Doctorate Dissertation

博士論文

Studies on Aerosol Chemical Compositions and Mixing States with Black Carbon

(エアロゾルの化学組成とブラックカーボンとの混合状態に関する研究)

A Dissertation Submitted for Degree of Doctor of Philosophy

July 2018

平成30年7月博士（理学）申請

Department of Earth and Planetary Science, Graduate School of Science, The University of Tokyo

東京大学大学院理学系研究科

地球惑星科学専攻

Yuya Ozawa

小澤　優哉

Abstract

Aerosols in the atmosphere, directly and indirectly, affect global radiation budget and therefore, affect climate. Because black carbon (BC) aerosols efficiently absorb solar radiation, their direct radiative forcing (DRF) is estimated to be the third largest following that of carbon dioxide and methane. However, there are large uncertainties in the BC DRF estimates. One of the largest uncertainty sources is BC mixing state, namely how individual BC-containing particles are coated (internally mixed) with other aerosol compounds. The coating increases both the BC mass absorption cross section (MAC) and removal rate through wet deposition. Since it is difficult to measure the chemical composition of the aerosol particles internally mixed with BC, the mixing state of BC is not well understood.

A laser-induced incandescence-mass spectrometry (LII-MS) is one of the techniques that can quantify the chemical compositions by BC mixing states. Previous studies have demonstrated that it is possible to quantify by LII-MS in laboratory experiments. The purpose of this study is to improve the LII-MS for applying to the atmospheric observations and to clarify the variation of the chemical compositions of aerosols internally and externally mixed with BC particles based on atmospheric measurements. Firstly, the MS section was improved and evaluated for practical application of LII-MS. Secondary, BC mixing state was observed in the downstream region of the large-scale East Asian emission source using LII-MS, and the variation of the chemical composition of aerosols internally and externally mixed with BC was clarified.

The LII-MS analyzer combines laser-induced incandescence analysis (LII) and mass spectrometry (MS) in series. The LII-MS analyzer quantifies the chemical composition of particles internally mixed with BC particles (BC-containing particles) and externally mixed with BC

particles (BC-free particles) by switching LII laser on and off. In order to quantify these mass concentrations, improvements in the MS section are necessary.

A particle trap-laser desorption mass spectrometer (PT-LDMS) is used for the MS section. The PT-LDMS vaporizes particles corrected on a particle trap by thermal decomposition and quantifies the mass concentration of the chemical composition of aerosols with a mass spectrometer. Because the decomposed species of sulfate compounds (SO_4^{2-}) depend on decomposition temperature, the mass concentration of SO_4^{2-} measured by PT-LDMS contains potential uncertainties. In this study, the temperature dependence of the aerosol components including ammonium sulfate ($(NH_4)_2SO_4$) was investigated by the laboratory experiments, and the optical system and the control system of the CO_2 laser heating were improved. Then, detailed uncertainties about accuracy and precision were evaluated by comparison with filter collection and chemical analysis method by ambient measurements. This clarified uncertain factors in the measurement of SO_4^{2-}. As a result, the PT-LDMS could realize stable and high sensitivity measurements of SO_4^{2-}.

On the other hand, because the decomposition temperature of nitrate aerosols (NO_3^-) is low, possible uncertainty in the NO_3^- measurement exists depending on the trap temperature of the particle collection section. In this study, the stable NO_3^- measurement was realized by improving the cooling efficiency of the particle trap. In addition to the improvement and evaluation of the MS section, LII-MS was able to quantify stably the inorganic compounds classified with BC mixing state by changing the laser control method in the LII section and improving the analysis method. An indicator to evaluate the lower detection limit of the LII-MS was set up and overall uncertainty was evaluated.

Using the improved LII-MS analyzer, in situ measurements of aerosols were conducted in Gwangju institute of science and technology (GIST), Gwangju, Korea (35°13′N, 126°50′E) from March 27 to April 7, 2016. The observation site is located on the west side of Korea. According to backward trajectory analysis, aerosols and precursor gas of the continental origin are often transported to the observation site during the measurement period due to the westerly wind of the lower atmosphere. The mass concentration of inorganic aerosols (secondary product) and BC particles (primary discharge) measured by the LII-MS analyzer also well correlated, thus the observed air masses were frequently affected by air originating from the Asian continent.

The mass concentrations of inorganic aerosols (SO_4^{2-} and NO_3^-) were quantitatively measured in atmosphere classified by BC mixing state by the observation at GIST for the first time. For the mass fractions of each compound to all the quantified compounds (G_{SO4}, G_{NO3}), no significant difference was found between BC-containing and BC-free particles on average. When comparing the mass fraction SO_4^{2-} and NO_3^- internally mixed with BC within the total mass concentration of each species (F_{SO4}, F_{NO3}), the average values of F_{SO4} and F_{NO3} were similar (0.16 and 0.17), and the one-hour values showed a weak positive correlation during the measurement period. These averaged features are generally consistent with the expected from the particle growth by a condensation and coagulation processes.

1 h values of F_{SO4} and F_{NO3} show large variabilities between 0.05 and 0.4, and a weak positive correlation was found between these two quantities. However, these values did not correlate with the number ratio of BC to that of the total aerosol particles. In addition, F_{SO4} exhibited an inverse correlation with the mass concentration of SO_4^{2-} (M_{SO4}), but no clear relationship was found within NO_3^-. These results cannot be explained consistently by the solely condensation and coagulation

processes. Calculations using an aerosol box model developed in this study also confirmed the condensation process alone cannot reproduce the observed features.

The observed negative correlation between M_{SO4} and F_{SO4} was resulted by low F_{SO4} values in highly polluted air masses (high M_{SO4}) originating from the continent and high F_{SO4} values in clean air masses (low M_{SO4}) transported from the free troposphere. In the former case, a presence of "droplet mode" in aerosol size distributions suggests the liquid-phase reactions within cloud and/or fog droplets, and these processes can potentially explain the observed high M_{SO4} and low F_{SO4} values. These observed "chemical features" are not inconsistent with the presence of low altitude clouds during transport of air from the Asian continent within the planetary boundary layer (meteorological features).

The chemical features of low M_{SO4} and high F_{SO4} air are also not inconsistent with the fact that these air parcels were transported from the free troposphere, considering possible wet removal of aerosols, which are externally mixed with BC.

The results presented in this study show that averaged features of BC mixing state were generally consistent with the ones resulted in condensation and coagulation processes; however, large variability in 1 h data that cannot be explained solely by condensation and coagulation process. Although the supporting data are limited, the present study suggested that the aqueous-phase chemical production and the wet-removal of aerosols also potentially play roles. These processes are considered to universally take place, but the relative importance is considered to differ depending on areas and seasons. Developing the ground-based or aircraft observation in places other than East Asia can be expected to contribute to better understandings of the mixing state of BC and their underlying mechanisms in the future.

List of acronyms

AMS	Aerosol mass spectrometer
ATOFMS	Aerosol time-of-flight mass spectrometry
BC	Black carbon
CCN	Cloud condensation nuclei
CE	Collection efficiency
CH	China
CPC	Condensation particle counter
C2di	Oxalic acid
C9di	Azelaic acid
DMT	Droplet measurement technology
DMA	Differential mobility analyzer
EI	Electron impact ionization
ext	External mixture
FT	Free troposphere
GDAS	Global data assimilation system
GIST	Gwangju institute of science and technology
HEPA	High-efficiency particulate air
HYSPLIT	Hybrid single-particle lagrangian integrated trajectory
int	Internal mixture
IPCC	Intergovernmental panel on climate change
JAXA	Japan aerospace exploration agency

KMA	Korea meteorological agency
LII	Laser-induced incandescence
LII-MS	Laser-induced incandescence-mass spectrometric analyzer
LOD	Limit of detection
LPM	Little per minute
MODIS	Moderate resolution imaging spectrometer
MR	Maritime
MS	Mass spectrometer
MTSAT	Multi-functional transport satellite
NIST	National instrument of standard technology
NOAA	National oceanic and atmospheric administrations
OC	Organic carbon
OL	Oleic acid
OM	Organic matter
OPC	Optical particle counter
PAC	Principle component analysis
PALMS	Particle analysis by laser mass spectrometry
PBL	Planetary boundary layer
PILS	Particle-into-liquid sampler
PSL	Polystyrene latex
PT-LDMS	Particle trap-laser desorption mass spectrometer
QMS	Quadrupole mass spectrometer

RH	Relative humidity
RIE	Relative ionization efficiency
RSMS	Rapid single-particle mass spectrometer
SEM	Secondary electron multiplier
SJAC	Steam jet aerosol collection
SMPS	Scanning mobility particle sizer
SPA	Sulfate particle analyzer
SP2	Single particle soot photometer
SP-AMS	Soot-aerosol mass spectrometer
ST	Stagnated
TDCIMS	Thermal desorption chemical ionization mass spectrometer
TEM	Transmission electron microscopy
UV	Ultraviolet
VTDMA	Volatility tandem differential mobility analyzer

Contents

1. General Introduction

1.1. Atmospheric aerosols

Atmospheric aerosols are small solid and liquid particles suspended in air. Aerosols can affect air quality, health, and climate on a regional and global scale. Individual particles have various sizes, compositions, and shapes, which determine the physical and chemical properties of aerosols [*Whitby* 1976; *Hinds* 1999; *Seinfeld and Pandis* 2006]. In turn, these physical and chemical properties cause the various optical and hygroscopic properties of aerosols. Aerosol particles have large influences on the radiative balance of the Earth's atmosphere by scattering or absorbing solar visible radiation (direct effect) and by altering the microphysical properties, lifetime, and coverage of clouds (indirect effect) [*IPCC* 2013].

Atmospheric aerosols mainly consist of sulfate, nitrate, ammonium, organic materials, black carbon (BC), sea salt, and dust. BC, some organics, sea salt, coastal materials, and dust are called primary particles, which are emitted into the atmosphere from emission sources directly. In contrast, sulfate, nitrate, and some other organics are called secondary particles, which are formed by gas-particle partitioning in the atmosphere. As an important type of urban fine particles, BC aerosols are described in the following section.

1.2. Black carbon (BC)

BC is defined as an ideally light-absorbing material composed of carbon [*Petzold et al.*, 2013]. BC is a primary material and is emitted from the incomplete combustion of biomass and fossil fuels. The major sources of BC are thermal power plants and diesel exhaust gas. BC is distinguishable from other forms of carbon and carbonaceous compounds in atmospheric aerosols

because it has a unique combination of the following physical properties. (1) It strongly absorbs visible light with a mass absorption cross-section of at least 5 m^2 g^{-1} [*Bond and Bergstrom*, 2006]. (2) It is refractory with a vaporization temperature near 4000 K [*Schwarz et al.*, 2006]. (3) It is insoluble in water and other components of atmospheric aerosols [*Fung* 1990]. (4) It exists as an aggregate of carbon spherules with a diameter of a few tens of nanometers [*Medalia and Heckman* 1969]. Figure 1.1 shows a summary of our understanding of the formation of BC particles [e.g., *Bockhorn et al.*, 1994; *Lahaye et al.*, 1981; *Siegla et al.*, 1981; *Tonokura*, 2014].

Although BC simply generated by the incomplete combustion of C_nH_m consists of spheres of approximately 20 nm (1–3), it immediately aggregates and develops an aggregate morphology (4, 5) [*Haynes and Wagner* 1981]. Freshly emitted BC particles often exist as an external mixture with organic and inorganic components [*Li et al.*, 2003, *Pósfai et al.* 2004, *Mallet et al.,* 2004]. The major global sources of BC are the open burning of forests and savannas, solid fuels for cooking and heating, and on-road and off-road diesel engines [*Bond et al.*, 2013]. After emission, BC particles acquire "coating materials" through the condensation of semi-volatile gaseous components and coagulation with other aerosol particles and then form internal mixtures [*Lee et al.*, 2002; *Shiraiwa et al.*, 2007]. The emitted BC aerosols are transported and removed from the atmosphere via wet and dry deposition. The mixing state of BC is described in the following section.

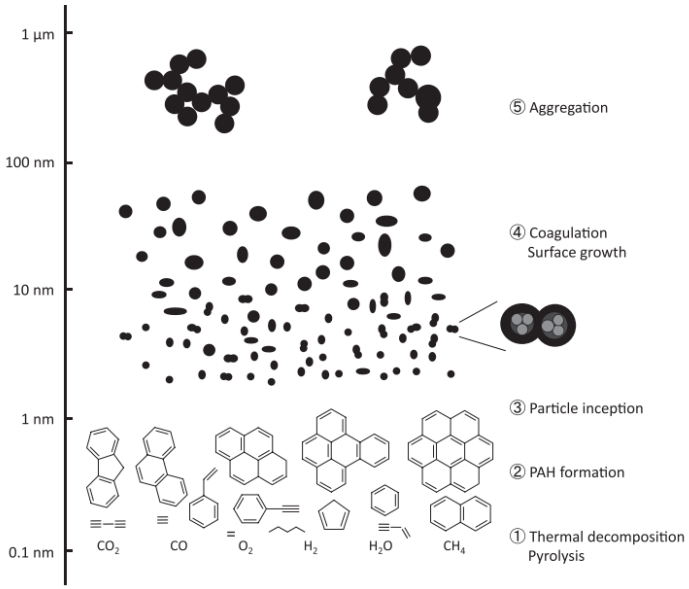

Figure 1.1. Schematic diagram of soot formation in premixed flame summarized by *Tonokura et al*. [2014].

1.3. Mixing state of BC

BC particles emitted to the atmosphere acquire coating materials by undergoing transformations, including the condensation of organic and inorganic gaseous species, heterogeneous reactions, and coagulation with other aerosol particles. These chemical transformations, which are commonly referred to as aging processes, change the mixing state, morphology, hygroscopicity, and optical properties of BC [e.g., *Wyslouzil et al.,* 1994; *Zhang and Zhang* 2005; *Levitt et al.,* 2007; *Xue et al.*, 2009; *Khalizov et al.,* 2013; *May et al.*, 2013]. After emission, condensation and coagulation cause individual chemical components to become an internal mixture. Figure 1.2 shows a transmission electron microscopy (TEM) image of BC particles taken by *Zhang et al.* [2008]. BC, immediately after its emission, exits as an aggregate with clearly discernible spherical primary particles of ~15 nm in diameter (Figure 1.2a). Coated BC aggregates were surrounded by smaller droplets of sulfuric acid, produced via splattering when the agglomerates deposited on the TEM grid (Figure 1.2b). *China et al.* [2013] quantified the

morphology and mixing state of BC particles and classified them into four categories: (1) ~50% are embedded (heavily coated), (2) ~34% are partly coated (attached with BC), (3) ~12% have inclusions, and (4) ~4% are bare. Figure 1.3 shows a TEM image of aerosol particles emitted from factories and transported into the atmosphere. The BC particles are shown by arrows and are mixed with other materials (sulfate and organics). In this study, particles containing BC completely inside are referred to as BC-containing particles or internal mixtures with BC, and particles not containing BC internally are called BC-free particles or external mixtures with BC. The mixing rate of BC depends on the concentration of gaseous species and aerosol particles [*Zhang et al.*, 2008]. According to a few previous studies, mixing has occurred within a few hours after emission at certain locations [*Moteki et al.*, 2007; *Moffet and Prather*, 2009], but there are insufficient measurements to estimate the extent of internal mixing throughout the atmosphere [*Bond et al.*, 2013]. The effects on climate caused by BC mixing states are described in next section.

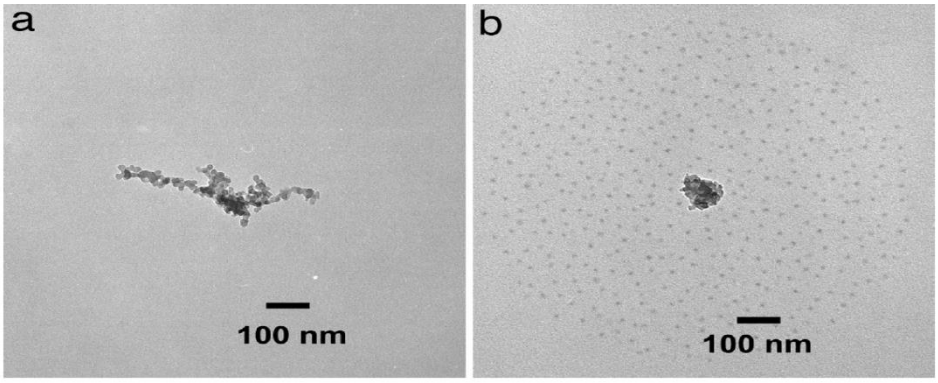

Figure 1.2. TEM image of BC particles: fresh BC (a) and BC after exposure to sulfuric acid (H_2SO_4) vapor and 5% RH (b). The cloud of small droplets surrounding the BC particle corresponds to sulfuric acid, which was shaken off the coated BC particle after impacting on the TEM grid.

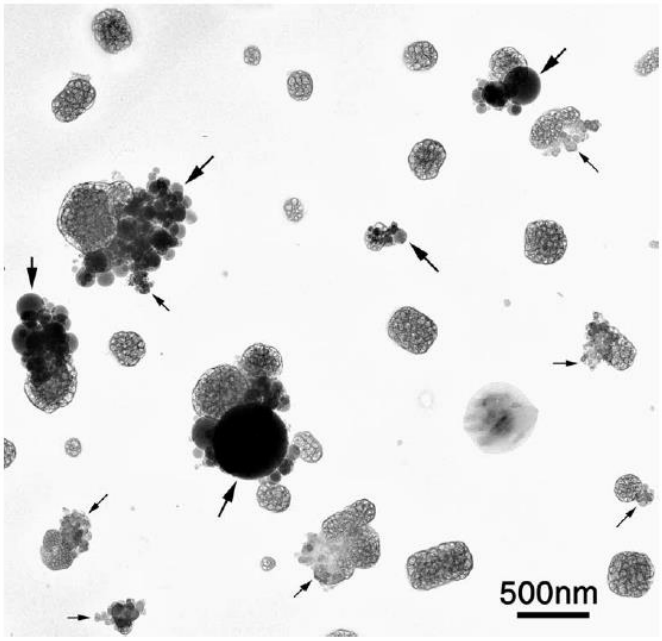

Figure 1.3. TEM image of ammonium sulfate particles mixed with soot (small arrows) and spherical silica (Bold arrows) by *Li et al.* [2003]. Ammonium sulfate particles formed bubbles under the radiation of electron beam.

1.4. Climate impacts of BC mixing state

Inorganic and organic aerosols scatter solar light and have cooling effects on the atmosphere. On the other hand, BC aerosols strongly absorb solar radiation and contribute to heating the atmosphere [*Rosen et al.*, 1979; *Charlson et al.*, 1991; *Ramanathan and Carmichael*, 2008]. Figure 1.4 shows the radiative forcing of climate between 1750 and 2011, obtained from the assessment report 5 by Intergovernmental Panel on Climate Change (IPCC). BC cause the largest positive radiative forcing after carbon dioxide (CO_2) and methane (CH_4) [*Jacobson*, 2000; *Hansen et al.*, 2000]. The net warming effect of BC aerosols balances the net cooling effect of other non-absorbing aerosols. However, the estimated radiative forcing of BC particles has a large uncertainty. This uncertainty is mainly derived from the estimation of BC emission and the parameters of BC particles (i.e., absorption and lifetime). Because the sources of BC are so diverse, the difficulty in quantifying them contributes to the uncertainty in evaluating the impact on climate

caused by BC [*Bond et al.,* 2013]. As described in the previous section, BC exists along with other aerosol components. The mixing state of BC affects the estimation of climate impact. The mixing state of BC is the focus of the next section.

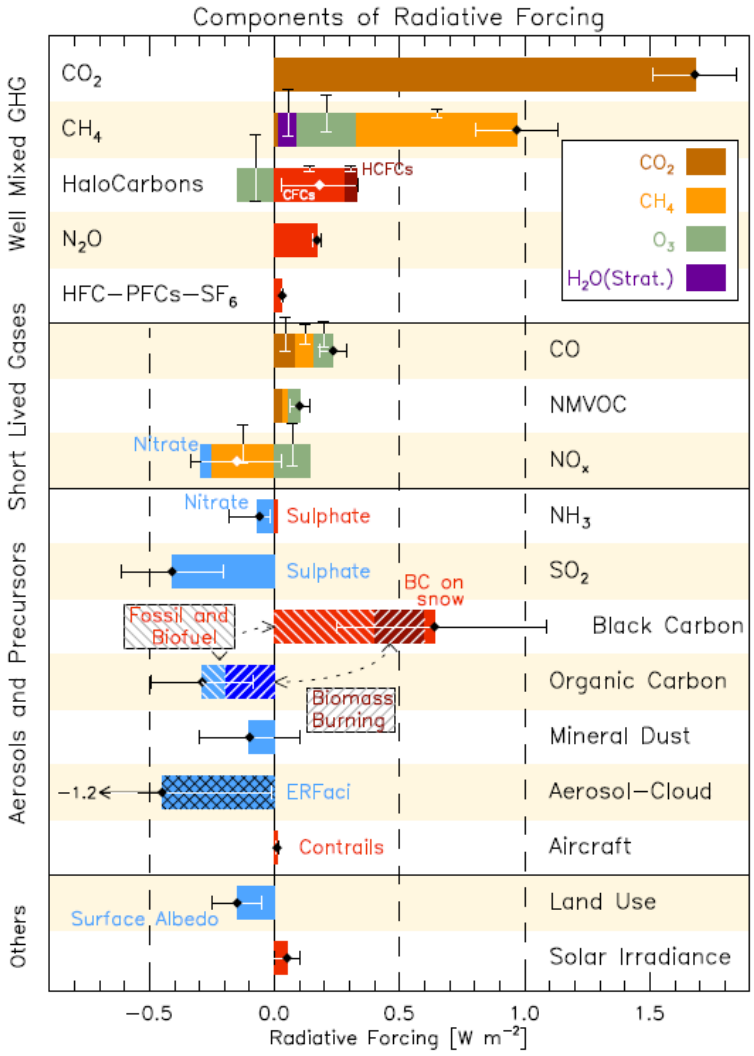

Figure 1.4. Radiative forcing bar chart for the period 1750-2011 based on emitted compounds (gases, aerosol procurers) or other changes. The values represent the forcing in 2011 relative to the start of the industrial year (about 1750).

The interaction between BC and climate systems depends on the optical properties and hygroscopicity of BC particles. BC-containing particles have different absorption efficiencies and lifetimes than pure BC particles. The coating materials of BC particles enhance their light absorption [*Fuller et al.* 1999; *Jacobson* 2001; *Lack and Cappa*, 2010]. This enhancement is caused by non-absorbing coating, which focuses incoming photons on the BC core. Uncertainty occurs depending on the assumptions of the mixing state of BC and the amount of non-absorbing components internally mixed with BC. In some models, core-shell type [*Fuller et al.*, 1995] and Maxwell-Garnet effective median approximation [*Heller*, 1965] are often used for the BC mixing state. BC particles internally mixed with other components become hydrophilic and indicate cloud condensation nuclei (CCN) activity [*Kuwata et al.*, 2007; *Jacobson*, 2006]. This process can reduce the lifetime of BC particles [*Stier et al.*, 2006]. The CCN activity depends more on particle size rather than composition, but for a constant particle size, the mass fraction of BC to other chemical composition is important [*Dusek et al.*, 2006]. Therefore, it is necessary to consider the size and composition of BC-containing particles for estimating the climate impact of BC. The treatment of BC particles in global models does not always reflect their theoretical dependence on size and a soluble fraction. The properties of BC-containing particles determined from experimental data have been used in most global radiative models [*Feng et al.*, 2003; *Wang et al.,* 2014; *Saleh et al.*, 2015]. *Kodros et al.*, [2015], who used a global chemical transport model, have proposed that more measurements are needed on total emissions mass, emission size distribution, and mixing state in order to better estimate climate forcing. The measurements of BC and its mixing state are described in the next section.

1.5. Measurement technics of mixing state of aerosol

The understanding of the mixing state of BC is important for reducing the uncertainty of BC forcing in climate models. In this section, I describe previous studies regarding the measurement of BC and its mixing state. As described in Section 1.2, BC has some unique properties. These properties distinguish BC particles from other aerosol components.

Electron microscopy is a common offline technique used for investigating the morphology and mixing state of individual BC particles. When using this technique, particles are collected on a filter and are irradiated by electrons under vacuum conditions. Information on the surface, structure, and elemental composition of the particles are obtained from scattered and transmitted electrons and the X-rays produced by interactions of electrons with the particles. As shown in Figures 1.3 and 1.4, electron microscopy is a useful tool that can be used to directly observe particle morphology. Electron microscopy data have shown that fresh BC particles are an aggregate of carbon spherules with a diameter of a few tens of nanometers and consisting of graphite layers [*Heidenreich et al.* 1968, *Medalia and Heckman* 1969, *Martins et al.* 1998]. They exist as an external mixture with other components [*Pósfai et al.*, 2003; *Li et al.*, 2003]. After emission, BC particles become internally mixed with organic and sulfuric compounds [*Okada et al.*, 2001; *Li et al.*, 2003; *Adachi et al.*, 2010]. Although electron microscopy involves offline measurements, it has provided valuable and important information on the composition, morphologies, and transformations of BC-containing particles.

Online techniques to measure BC particles and its mixing states have been developed and used. Instruments for online measurements can measure particulate sulfur, nitrogen, and carbon concentrations in situ in time scales that can vary from a few minutes to hours.

The laser-induced incandescence (LII) method has been used for online detection of BC and

certain metals [*Stephens et al.*, 2003]. This method is based on the properties of strong light absorption and high vaporization temperature. The Single Particle Soot Photometer (SP2), which is a commercially available LII BC analyzer developed by Droplet Measurement Technology (DMT, Boulder, USA), is able to provide continuous, real-time size and coating information for individual BC-containing particles over a wide range of mass concentration of BC. [*Gao et al.*, 2007; *Moteki and Kondo*, 2007; 2010; *Schwarz et al.*, 2006]. SP2 detects the incandescence and scattering signals of BC-containing particles induced by a 1064 nm Nd:YAG intra-cavity laser. SP2 measurements have provided number size distributions of BC in fresh urban plumes dominated by fossil fuel (FF) combustion [e.g., *Schwarz et al.*, 2008; *Kondo et al.*, 2011], in aged plumes in Asian outflows [*Shiraiwa et al.*, 2008], and in the remote upper troposphere and lower stratosphere [*Schwarz et al.*, 2006; 2008]. *Moteki et al.* [2014] have identified two morphological types of mixed BC-containing particles, namely attached and coated, which are important for understanding the impact of BC on climate. They reported that the observed number fractions of attached-type particles among morphologically identified BC-containing particles were generally less than 0.1, but ambient occasionally reached ~0.4 during short events during measurements in Tokyo, Japan. *Ohata et al.* [2016b] have investigated the hygroscopicity of BC-containing and BC-free particles using a humidified SP2, which is an SP2 equipped with a humidifier above the inlet [*Schwarz et al.*, 2015; *Ohata et al.*, 2016a]. They reported that the median hygroscopicity parameter of BC-containing and BC-free particles was well correlated and concluded that the chemical compositions of BC-free particles and BC-coating materials were similar on average.

Real-time in-situ techniques using mass spectrometry have been employed for the analysis of individual particles in flowing gas streams. These techniques involve rapid depressurization of the aerosols, the formation of a particle beam, and irradiation of the particles by a high-power

pulse laser to produce ions that can be analyzed via mass spectrometry. Aerosol particles are introduced into a vacuum chamber before they are analyzed. The time spent under reduced pressure is typically ~1 ms, which is short enough to avoid the loss of most semi-volatile compounds [*McMurry*, 2000]. Different techniques have been developed, such as particle analysis by laser mass spectrometry (PALMS) [*Thomson and Murphy*, 1994], aerosol time-of-flight mass spectrometry (ATOFMS) [*Noble et al.*, 1994], and rapid single-particle mass spectrometry (RSMS) [*Mansoori et al.*, 1994]. The instruments used can detect trace metals and inorganic and carbonaceous compounds in individual particles. These instruments have been shown to be capable of providing information on surface coating [*Carson et al.*, 1997a; 1997b], multicomponent crystallization [*Ge et al.*, 1996], compound speciation [*Neubauer et al.*, 1996], and oxidation state [*Neubauer et al.*, 1995]. These single-particle mass spectrometers have also been used in field measurements of atmospheric aerosols and have provided important information on atmospheric aerosols. For example, *Hinz et al.* [1994; 1996] found that principle component analysis (PCA) could be used for identifying the major chemical components of the primary particle types with information on particle source categories. *Murphy and Thomson* [1997a; 1997b] found that sulfate and nitrate usually, but not always, are found in different particles and that small amounts of organics are present in most particles in Idaho Hill aerosols. *Liu et al.* [1997] were able to identify pyrotechnically derived particles originating from fireworks and they also demonstrated the capability of detecting and tracking aerosol particles of a specific size and chemical composition from a particular source over time. During an in-situ measurement campaign in Cape Grim, Australia, via PALMS, *Murphy and coauthors* found that most particles down to 0.16 μm during clean marine conditions also contained some sea salt, that organics were internally mixed with that, and that halogens in individual particles were not correlated with sulfate

but were correlated with organics [*Middlebrook et al.*, 1998; *Murphy and Thomson*, 1997c; *Murphy et al.* 1998]. Although only a small fraction of the particles is irradiated, useful information on the chemical composition and mixing state of individual particles has been provided by the aforementioned instruments.

A technique combining near-infrared lasers and mass spectrometry has been developed as a method for measuring the chemical composition of aerosols focusing on the mixing states of BC. *Onasch et al.* [2012] developed an instrument that combines an Aerodyne aerosol mass spectrometer (AMS, Aerodyne Research Inc., USA) with a solid-state laser cavity used in a DMT SP2 (Soot Particle-Aerosol Mass Spectrometer, SP-AMS). The Aerodyne AMS is an instrument that is able to measure the chemical composition of ambient aerosol particles using a thermal decomposition method, enabled by a tungsten vaporizer inside the vacuum chamber [*Jayne et al.*, 2000]. The laser cavity is incorporated inside the vacuum chamber in front of the AMS vaporizer, so that the SP-AMS is able to directly measure the chemical composition of aerosol particles internally mixed with BC by switching the laser and the AMS vaporizer. *Lee et al.*, [2015] indicated that there was, on average, no significant difference in a fraction of the chemical composition of BC-containing particles and BC-free particles in an urban environment. Although quantitative measurements using the aforementioned technique combining laser and aerosol mass spectrometry are underway, it is a useful technique that is able to measure chemical composition focusing on the mixing state of BC.

A new instrument, called laser-induced incandescence-mass spectrometric analyzer (LII-MS), has been developed for quantifying the chemical composition of aerosols classified by the mixing state of BC [*Miyakawa et al.*, 2014]. This analyzer consists of an LII analyzer and a particle trap laser desorption mass spectrometer (PT-LDMS: Takegawa et al. 2012). The LII analyzer

selectively detects and vaporizes BC-containing particles. The PT-LDMS analyzes the chemical composition of the aerosol particles transported from the LII analyzer. The concepts behind this method were demonstrated by *Miyakawa et al.* [2014]. However, detailed evaluations of the PT-LDMS, which affects the quantification of the LII-MS analyzer, and ambient measurements using the LII-MS analyzer have not been conducted.

1.6. Purpose of this study

BC particles play an important role in global warming, and there is a large uncertainty in the estimation of radiative forcing caused by BC particles [*IPCC* 2013; *Bond et al.*, 2013]. This uncertainty is caused by our insufficient understanding of the chemical components mixed with BC particles. The chemical components internally mixed with BC particles affect their optical properties and lifetime. It is necessary to know quantitatively the time and space variations of the chemical components internally/externally mixed with BC. In previous observational studies, electron microscopy, LII, and mass spectrometry have provided a lot of information for our basic understanding of the mixing states of BC. However, there are no instruments that quantify the chemical compositions mixed with BC particles internally. Therefore, the purpose of this study is to quantify the chemical composition of classified BC mixing states via ambient measurements using the LII-MS method and to understand the variation factors of the mixing states of BC. For that purpose, an evaluation of PT-LDMS was performed to determine the performance of LII-MS, and ambient measurements conducted in Korea in the spring of 2016 were used. The evaluation of PT-LDMS is presented in Chapter 3. The details of LII-MS are provided in Chapter 4. The results of the aforementioned ambient measurements and an interpretation of them are described in Chapter 5.

Reference

Adachi, K., Chung, S. H. and Buseck, P. R. (2010), Shapes of soot aerosol particles and implications for their effects on climate, *J. Geophys. Res.*, 115, D15206

Bockhorn, H. (1994) Soot Formation in Conbution: Mechanisms and Models, Springer, Berlin, Heidelberg.

Bond, T. C., and Bergstrom, R. W. (2006), Light absorption by carbonaceous particles: An investigative review, *Aerosol Sci. and Technol.*, 40(1), 27–67

Bond, T. C., Doherty, S. J., Fahey, D. W., Forster, P. M., Berntsen, T., DeAngelo, B. J., Flanner, M. G., Ghan, S., Kärcher, B., Koch, D., Kinne, S., Kondo, Y., Quinn, P. K., Sarofim, M. C., Schultz, M. G., Schulz, M., Venkataraman, C., Zhang, H., Zhang, S., Bellouin, N., Guttikunda, S. K., Hopke, P. K., Jacobson, M. Z., Kaiser, J. W., Klimont, Z., Lohmann, U., Schwarz, J. P., Shindell, D., Storelvmo, T., Warren S. G., and Zender, C. S. (2013). Bounding the Role of Black Carbon in the Climate System: A Scientific Assessment, *J. Geophys. Res.*, 118: 1-173.

Carson, P. G., Johnston, M. V., Wexler, A. S., (1997a). Laser desorption ionization of ultrafine aerosol particles. *Rapid Communications in Mass Spectrometry*, 11, 993-996.

Carson, P. G., Johnston, M. V., Wexler, A. S., 1997b. Real-time monitoring of the surface and total composition of aerosol particles. Aerosol Sci. Technol. 26 (4), 291-300.

Charlson R. J., Langner, J., Rodhe, H., Leovy, C. B., and S. G. Warren (1991), Perturbation of the northern hemisphere radiative balance by backscattering from anthropogenic sulfate aerosols, Tellus, 43AB, 152-163.

China, S., Mazzoleni, C., Gorkowski, K., Aiken, A. C., and Dubey, M. K. (2013), Morphology and mixing state of individual freshly emitted wildfire carbonaceous particles, *Nature*, 4:2122, DOI: 10.1038/ncomms3122.

Dusek, U., Frank, G. P., Hildebrandt, L., Curtius, J., Schneider, J., Walter, S., Chand, D., Drewnick, F., Hings, S., Jung, D., Borrmann, S., and Andreae, M. O. (2006), Size Matters More Than Chemistry for Cloud-Nucleating Ability of Aerosol Particles, *Science*, 312(5778), 1375-1378, doi: 10.1126/science.1125261.

Feng, J., Chan, C-. M., and Li, J-. X. (2003). A method to control the dispersion of carbon black in an immiscible polymer blend, *Poly. Engneer. Sci.*, 43(5), 1058-1063

Fuller, K. A. (1995), Scattering and absorption cross sections of compounded spheres. III. Spheres containing arbitrarily located spherical inhomogeneities, *J. Opt. Soc. Am.*, 12(5), 893–904, doi:10.1364/JOSA.A.12.000893.

Fuller, K. A., Malm, W. C., and Kreidenweis, S. M. (1999), Effects of mixing on extinction by carbonaceous particles, *J. Geophys. Res.*, 104(D13), 15941–15954, doi: 10.1029/1998JD100069.

Fung, K. (1990). Particulate carbon speciation by MnO2oxidation. *Aerosol Science and Technology*, 12(1), 15–122, doi: 10.1080/02786829008959332.

Ge, Z., Wexler, A.S., Johnston, M.V., (1996). Multicomponent aerosol crystallization. *J. Colloid. Interface Sci.*, 183, 68-77.

Gao, R. S., Schwarz, J. P., Kelly, K. K., Fahey, D.W. ,Watts, L. A., Thompson, T. L., Spackman, J. R., Slowik, J. G., Cross, E. S., Han, J.-H., Davidovits, P., Onasch, T. B., and Worsnop, D. R. (2007). A Novel Method for Estimating Light–Scattering Properties of Soot Aerosols using a Modified Single–Particle Soot Photometer, *Aerosol Sci. Technol.* 41:125-135.

Hansen, J. E., Sato, M., Ruedy, R., Lacis, A., and Oinas, V. (2000), Global warming in the twenty‐first century: An alternative scenario, *P. Natl. Acad. Sci.*, 97(18), 9875–9880.

Haynes, B. S., and Wagner, H. G. (1981), Soot Formation, *Progress in Energy and Combustion*

Science, 7(4), 229–273.

Heller, W. (1965), Remarks on refractive index mixture rules, *J. Phys. Chem.*, 69, 1123–1129.

Heidenreich, R. D., Hess, W. M. and Ban, L. L. (1968), A test object and criteria for high resolution electron microscopy, *J. Appl. Crystallogr.*, 1(1–19).

Hinds, W. C., (1999). Aerosol Technology, Jhon Wiley & Sons, New York.

Hinz, K. P., Kaufmann, R., Spengler, B. (1994). Laser-induced mass analysis of single particles in the airborne state. *Analytical Chemistry*, 66 (13), 2071-2076.

Hinz, K.P., Kaufmann, R., Spengler, B. (1996). Simultaneous detection of positive and negative ions from single airborne particles by real-time laser mass spectrometry. *Aerosol Sci. and Technol.*, 24 (4), 233-242.

Intergovernmental Panel on Climate Change (IPCC) (2013). Climate change 2013: The Physical Science Basis. Contribution of Working Group I to the 5th Assessment Report of the IPCC. Cambridge University Press, Cambridge, UK.

Jacobson, M. Z. (2000). A physically-based treatment of elemental carbon optics: Implications for global direct forcing of aerosols, *Geophys. Res. Lett.*, 27(2), 217-220, doi: 10.1029/1999GL010- -968.

Jacobson, M. Z. (2006), Effects of externally-through-internally‐mixed soot inclusions within clouds and precipitation on global climate, J. Phys. Chem. A, 110(21), 6860−6873, doi:10.1021/jp056391r.

Jayne, J. T., Leard, D. C., Zhang, X. F., Davidovits, P., Smith, K. A., Kolb, C. E., and Worsnop, D. R. (2000). Development of an Aerosol Mass Spectrometer for Size and Composition Analysis of Submicron Particles. *Aerosol Sci. Technol.* 33(1-2): 49-70.

Khalizov, A. F., Lin, Y., Qiu, C., Guo, S., Collins, D., and Zhang, R. Y. (2013) Role of OH-Initiated

Oxidation of Isoprene in Aging of Combustion Soot. *Environ. Sci. Technol.* 2013, 47, 2254-2263.

Kodros, J. K., Scott, C. E., Farina, S. C., Lee, Y. H., L'Orange, C., Volckens, J., and Pierce, J. R. (2015), Uncertainties in global aerosols and climate effects due to biofuel emissions. *Atmos. Chem. Phys.,* 15, 8577-8596.

Kondo, Y., H. Matsui, N. Moteki, L. Sahu, N. Takegawa, M. Kajino, Y. Zhao, M. J. Cubison, J. L. Jimenez, S. Vay, G. S. Diskin, B. Anderson, A. Wisthaler, T. Mikoviny, H. E. Fuelberg, D. R. Blake, G. Huey, A. J. Weinheimer, D. J. Knapp, and W. H. Brune (2011), Emissions of black carbon, organic, and inorganic aerosols from biomass burning in North America and Asia in 2008, *J. Geophys. Res.*, 116, D08204, doi:10.1029/2010JD015152.

Kuwata, M., Y. kondo, M. Mochida, N. Takegawa, and K. Kawamura, (2007), Dependence of CCN activity of less volatile particles on the amount of coating observed in Tokyo, 112 (D11207), doi: 10.1029/2006JD007758

Lahaye, J. and Prado, G. (1981), Soot in Combustion Systems and Its Toxic Properties, *Plenum Press*, New York.

Liu, D.-Y., Rutherford, D., Kinsey, M., Prather, K. A., (1997). Realtime monitoring of pyrotechnically derived aerosol particles in the troposphere. Analytical Chemistry 69 (10), 1808-1814.

Lee, J. H., Yoshida, Y., Turpin, B. J., Hopke, P. K., Poirot, R. L., Lioy, P. J., and Oxley, J. C. (2002), Identification of Sources Contributing to Mid-Atlantic Regional Aerosol. *J. Air & Waste Manage. Assoc.*, 52(10), 1186–1205, doi: 10.1080/10473289.2002.10470850

Lee, A. K. Y, M. D. Willis, R. M. Healy, T. B. Onasch, and J. P. D. Abbatt, (2015), Mixing state of carbonaceous aerosol in an urban environment: single particle characterization using the soot

particle aerosol mass spectrometer (SP-AMS), *Atmos. Chem. Phys.*, 15, 1823–1841, doi: 10.5194/acp-15-1823-2015

Levitt, N. P., Zhang, R., Xue, H., and Chen, J. (2007), Heterogeneous Chemistry of Organic Acids on Soot Surfaces, *J. Phys. Chem.*, 111, 4804-4814.

Li, J., Anderson, J. R., and Buseck, P. R. (2003), TEM study of aerosol particles from clean and polluted marine boundary layers over the North Atlantic, *J. Geophys. Res.*, 108(D6), 4189, doi: 10.1029/2002JD002106.

Mallet, M., Roger, J. C., Despiau, S., Putaud, J. P., and Dubovik, O. (2004), A study of the mixing state of black carbon in urban zone, *J. Geophys. Res.*, 109(D4), D04202, doi: 10.1029/2003JD003940.

Mansoori, B.A., Johnston, M.V., Wexler, A.S., (1994) Quantitation of ionic species in single microdroplets by on-line laser desorption/ionization. *Analytical Chemistry* 66 (21), 3681-3687.

Martins, J. V., Artaxo, P., Liousse, C., Reid, J. S., Hobbs, P. V., and Kaufman, Y. (1998), Effects of black carbon content, particle size, and mixing on light absorption by aerosol from biomass burning in Brazil, *J. Geophys. Res.*, 103(D24), 32041–32050.

May, A. A. Presto, A. A., Hennigan, C. J., Nguyen, N. T., Gordon, T. D., and Robinson, A. L. (2013), Gas-Particle Partitioning of Primary Organic Aerosol Emissions: (2) Diesel Vehicles Environ. Sci. Technol., 47, 8288– 8296

McMurry, P. H. (2000), A review of atmospheric aerosol measurements, *Atmos. Environ.*, 34, 1950-1999.

Medalia, A. I., and Hackman, F. A. (1969). Morphology of Aggregates - II. Size and Shape Factors of Carbon Black Aggregates from Electron Microscopy. Carbon, 7, 567–582.

Middlebrook, A. M., Murphy, D. M., Thomson, D. S., (1998). Observations of organic material in individual marine particles at Cape Grim during ACE-1. *J. Geophys. Res.*, 103, 16475-16483.

Moffet, R. C., and Prather, K. A. (2009), In-situ measurements of the mixing state and optical properties of soot with implications for radiative forcing estimates, *P. Natl. Acad. Sci.*, 106(29), 11872−11877.

Miyakawa, T., Takeda, N., Koizumi, K., Tabaru, M., Ozawa, Y., Hirayama, N., and Takegawa, N. (2014). A New Laser Incandescence-Mass Spectrometric Analyzer (LII-MS) for Online Measurement of Aerosol Composition Classified by Black Carbon Mixing State, *Aerosol, Sci. Thecnol.* 48: 853-863.

Moteki, N., Kondo, Y., Miyazaki, Y., Takegawa, N., Komazaki, Y., Kurata, G., Shirai, T., Blake, D. R., Miyakawa, T., and Koike, M. (2007). Evolution of Mixing State of Black Carbon Particles: Aircraft Measurements over the Western Pacific in March 2004, Geophys. Res. Lett. 34, L11803, doi:10.1029/2006GL028943.

Moteki, N., and Kondo, Y. (2010). Dependence of Laser-induced Incandescence on Physical Properties of Black Carbon Aerosols: Measurements and Theoretical Interpretation, Aerosol Sci. Technol. 44:663-675.

Moteki, N., Kondo, Y., and Adachi, K. (2014). Identification by single-particle soot photometer of black carbon particles attached to other particles: Laboratory experiments and ground observations in Tokyo, J. Geophys. Res. 119:1031–1043, doi:10.1002/2013JD020655.

Murphy, D. M., and Thomson, D. S. (1995). Laser ionization mass spectroscopy of single aerosol particles. *Aerosol Sci. Technol.*, 22 (3), 237-249.

Murphy, D. M., and Thomson, D. S. (1997a). Chemical composition of single aerosol particles at Idaho Hill: negative ion measurements. *J. Geophys. Res.*, 102 (D5), 6353-6368.

Murphy, D. M., and Thomson, D. S., (1997b). Chemical composition of single aerosol particles at Idaho Hill: Positive ion measurements. J. Geophys. Res. 102 (D5), 6341-6352.

Murphy, D. M., Thomson, D. S., Middlebrook, A. M., (1997c). Bromine and iodine in single aerosol particles at Cape Grim. *Geophys. Res. Lett.*, 24, 3197-3200.

Murphy, D. M., Thomson, D. S., Middlebrook, A. M., Schein, M. E., (1998). In situ single particle characterization at Cape Grim. Journal of Geophysical Research 103, 16485-16491.

Neubauer, K. R., Johnston, M. V., Wexler, A. S. (1995). Chromium speciation in aerosols by rapid single-particle mass spectrometry. *International Journal of Mass Spectrometry and Ion Processes*. 151, 77-87.

Neubauer, K.R., Sum, S.T., Johnston, M.V., Wexler, A.S. (1996). Sulfur speciation in individual aerosol particles, *J. Geophys. Res.* 101 (D13), 18701-18707.

Noble, C.A., Nordmeyer, T., Salt, K., Morrical, B., Prather, K.A., (1994), Aerosol characterization using mass spectrometry, *Trends in Analytical Chemistry*, 13 (5), 218-222.

Okada, K., and Hitzenberger, R. M. (2001), Mixing properties of individual submicrometer aerosol particles in Vienna, Atmos. Environ., 35 (32), 5617-5628.

Ohata, S., J. P. Schwarz, Moteki, N., Koike, M., Takami, A., and Kondo, Y. (2016a). Hygroscopicity of materials internally mixed with black carbon measured in Tokyo. *J. Geophys. Res.* Doi: 10.1002/2015JD024153.

Ohata, S., Moteki, N., Mori, T., Koike, M., and Kondo, Y. (2016b). A key process controlling the wet removal of aerosols: new observational evidence, *Nature*, 6:34113, DOI: 10.1038/srep34113.

Onasch, T. B., A. Trimborn, E. C. Fortner, J. T. Jayne, G. L. Kok, L. R. Williams, P. Davidovits and D. R. Worsnop, (2012), Soot Particle Aerosol Mass Spectrometer: Development,

Validation, and Initial Application, *Aerosol Sci. Technol.*, 46:804-817.

Petzold, A., Ogren, J. A., Fiebig, M., Laj, P., Li, S. -M., Baltensperger, U., Holzer-Popp, T., Kinne, S., Pappalardo, G., Sugimoto, N., Wehrli, C., Widensohler, A., and Zhang, X. -Y. (2013), Recommendations for reporting black carbon measurements, *Atmos. Chem. Phys.*, 13(16), 8365–8379.

Pósfai, M., Simonics, R., Li, J., Hobbs, P. V., and Buseck, P. R. (2003), Individual aerosol particles from biomass burning in southern Africa: 1. Compositions and size distributions of carbonaceous particles, J. Geophys. Res., 108(D13), 8483, doi:10.1029/2002JD002291.

Pósfai, M., Gelencsér, A., Simonics, R., Arató, K., Li, J., Hobbs, P. V., and Buseck, P. R. (2004), Atmospheric tar balls: Particles from biomass and biofuel burning, *J. Geophys. Res.,* 109(D6), 1–9, doi: 10.1029/2003JD004169

Ramanathan, V., and Carmichael, G. (2008). Global and regional climate changes due to black carbon, *Nature*, 1, 221-227

Rosen, H., A., Hansen, D. A., Gundel, L. and Novakov, T. (1978), Identification of the optically absorbing component in urban aerosols, *Appl. Opt.*, 17(24), 3859–3861.

Saleh, R., Hennigan, C. J., McMeeking, G. R., Chuang, W. K., Robinson, E. S., Coe, H., Donahue, N. M., and Robinson, A. L. (2013). Absorptivity of brown carbon in fresh and photo-chemically aged biomass-burning emissions, Atmos. Chem. Phys., 13, 7683– 7693, doi:10.5194/acp-13-7683-2013.

Schwarz, J. P., Gao, R. S., Fahey, D. W., Thomson, D. S., Watts, L. A., Wilson, J. C., Reeves, M. J., Darbeheshti, M., Baumgardner, D. G., Kok, G. L., Chung, S. H., Schulz, M., Hendricks, J., Lauer, A., Kärcher, B., Slowik, J. G., Rosenlof, K. H., Thompson, T. L., Langford, A. O., Loewenstein, M., and Aikin, K. C. (2006). Single-particle measurements of midlatitude black

carbon and light-scattering aerosols from the boundary layer to the lower stratosphere, *J. Geophys. Res.*, 111(16), 1–15, doi:10.1029/2006JD007076

Schwarz, J. P., Spackman, J. R., Fahey, D. W., Gao, R. S., Lohmann, U., Stier, P., Watts, L. A., Thomson, D. S., Lack, D. A., Pfister, L., Mahoney, M. J., Baumgardner, D., Wilson, J. C., and Reeves J. M. (2008), Coatings and their enhancement of Black Carbon Light Absorption in the tropical atmosphere, *J. Geophys. Res.,* 113, D03203, doi: 10.1029/2007JD009042.

Schwarz, J. P., Perring, A. E., Markovic, M. Z., Gao, R. S., Ohata, S., Langridge, J. Lawa, D., McLaughlin, R., and Fahey, D. W. (2015), Technique and theoretical approach for quantifying the hygroscopicity of black-carbon-containing aerosol using a single particle soot photometer, *J. Aerosol Sci.,* 81, 110-126.

Seinfeld, J.H., and Pandis, S. N. (2006). Atmospheric Chemistry and Physics. *Jhon Wiley & Sons*, New York.

Shiraiwa, M., Kondo, Y., Moteki, N., Takegawa, N., Miyazaki, Y., and Blake, D. R. (2007), Evolution of mixing state of black carbon in polluted air from Tokyo. *Geophys. Res. Letters*, 34(16), 2–6, doi: 10.1029/2007GL029819.

Shiraiwa, M., Kondo, Y., Moteki, N., Takegawa, Sahu, L. K., Takami, A., Hatakeyama, S., Yonemura, S., and Blake, D. R. (2008), Radiative impact of mixing state of black carbon aerosol in Asian outflow, *J. Geophys. Res.*, 113, D24210, doi:10.1029/2008JD010546.

Siegla, D. C. and Smith, G. W. (1981), Particulate Carbon Formation during Combustion, *Plenum Press*, New York.

Stephens, M., Turner, N., and Sandberg, J. (2003), Particle identification by laser-induced incandescence in a solid-state laser cavity, *Applied Optics*, 42(19), 3726-3736.

Stier, P., Seinfeld, J. H., Kinne, S., Feichter, J., and Boucher, O., (2006), Impact of nonabsorbing

anthropogenic aerosols on clear‐sky atmospheric absorption, *J. Geophys. Res.*, 111(D18), D18201, doi:10.1029/2006JD007147.

Takegawa, N., Miyakawa, T., Nakamura, T., Sameshima, Y., Takei, M., Kondo, Y., and Hirayama, N. (2012). Evaluation of a New Particle Trap in a Laser Desorption Mass Spectrometer for Online Measurement of Aerosol Composition. Aerosol Sci. Technol. 46: 428-443.

Thomson, D.S., and Murphy, D.M. (1993), Laser-induced ion formation thresholds of aerosol particles in a vacuum, *Applied Optics*, 32 (33), 6818-6826.

Tonokura, K. (2014), Formation of Polycyclic Aromatic Hydrocarbons and Soot Particle in Combustion, *Earozoru Kenkyu*, 29(1), 5–9.

Wang, Q., Huang, R. –J., Cao, J., Han, Y., Wang, G., Li, G., Wang, Y., Dai, W., Zhang, R., and Zhou, Y. (2014), Mixing State of Black Carbon Aerosol in a Heavily Polluted Urban Area of China: Implications for Light Absorption Enhancement, *Aerosol Scie. Technol.*, 48: 689-697.

Whitby, K. T., (1976). The Physical Characteristics of Sulfur Aerosols. Atmos. Environ.,12:135-159.

Wyslouzil, B. E., Carleton, K. L., Sonnenfroh, D. M., Rawlins, W. T., and Armold, S. (1994), Observation of Hydration of Single, Modified Carbon Aerosols, *Geophys. Res. Let*., 21(19), 2107–2110.

Xue, H. X., Khalizov, A. F., Wang, L., Zheng, J., and Zhang, R. Y. (2009), Effects of Coating of Dicarboxylic Acids on the Mass–Mobility Relationship of Soot Particles, *Environ. Sci. Technol.*, 43, 2787– 2792

Zhang, D., and Zhang, R. (2005), Laboratory Investigation of Heterogeneous Interaction of Sulfate Acid with Soot, *Environ. Sci. Technol.*, 39, 5722-5728.

Zhang, R., Khalizov, A. F., Pagels, J., Zhang, D., Xue, H., and McMurry, P. H. (2008) Variability

in Morphology, Hygroscopicity, and Optical Properties of Soot Aerosols during Atmospheric Processing Proc. *Natl. Acad. Sci. U.S.A.*, 105, 10291-10296.

2. Theoretical Background

2.1. Introduction

BC particles undergo a chemical transformation during atmospheric transportation by obtaining a coating of inorganic or organic matters called "aging" [*Seinfeld and Pandis*, 2006]. The aging changes the mixing state, and chemical and physical properties of the BC particles, including morphology, hygroscopicity, and optical properties [*Zhang et al.,* 2008]. By condensation, heterogeneous reactions with inorganic and organic gases, and coagulation with other particles, the BC particles form internally mixed particles, which include other components. The formation processes of BC mixing states are described in this section.

2.2. Coagulation

Aerosol particles in the atmosphere come into contact due to their Brownian motion. During the collision, two particles coagulate to make a new particle. This process changes the number concentration of aerosols drastically and is, therefore, a major particle sink. According to *Muller* [1928], the rate of change of particle concentration due to coagulation can be described by the size distribution function $n(v, t)$, which is expressed by the following equation:

$$\frac{\partial n(v,t)}{\partial t} = \frac{1}{2}\int_{v_0}^{v-v_0} \beta(v-q, q)\, n(v-q, t)\, n(q, t) dq \; - n(v,t) \int_{v_0}^{\infty} \beta(q, v)\, n(q, t) dq, \quad (2.1)$$

where v and q are the volumes of the two colliding particles, v_0 is the volume of new particles generated by the collision, and β is the coagulation coefficient. The first term of equation (2.1) shows the probability that particles of volume $v - q$ collide with the particle of volume v, and the second term shows the probability that particles of volume v are lost in the collision. It is difficult to solve this equation analytically, and, therefore, it is necessary to solve it by a numerical method.

By assuming that the size distribution is a lognormal distribution and discontinuous, it is possible to calculate the change in concentration numerically for a discrete size distribution [*Jacobson*, 2005].

Table 2.1 shows the smallest coagulation coefficients for two typical particle sizes (D_{p1}, D_{p2}) [*Seinfeld and Pandis*, 2006]. The time constant of coagulation rapidly increases with the particle size. Large particles with a slow Brownian motion velocity have a large surface area and can act as a wide target for small particles with higher velocities. Collisions between large particles are slow due to their low velocities. On the other hand, small particles have high velocities, but the collision frequency is low because the cross-sectional area is small.

Table 2.1. Coagulation coefficients ($cm^3 s^{-1}$) of atmospheric particles[a]

	D_{p1} (μm)					
D_{p2} (μm)	0.002	0.01	0.1	1.0	10	20
0.002	8.9×10^{-10}	5.7×10^{-9}	3.4×10^{-7}	7.8×10^{-6}	8.5×10^{-5}	17×10^{-5}
0.01	5.7×10^{-9}	19×10^{-10}	2.5×10^{-8}	3.4×10^{-7}	3.5×10^{-6}	7.0×10^{-6}
0.1	3.4×10^{-7}	2.5×10^{-8}	15×10^{-10}	5.0×10^{-9}	4.5×10^{-8}	9.0×10^{-8}
1	7.8×10^{-6}	3.4×10^{-7}	5.0×10^{-9}	6.9×10^{-10}	2.1×10^{-9}	3.9×10^{-9}
10	8.5×10^{-5}	3.5×10^{-6}	4.5×10^{-8}	2.1×10^{-9}	6.1×10^{-10}	6.8×10^{-10}
20	17×10^{-5}	7.0×10^{-6}	9.0×10^{-8}	3.9×10^{-9}	6.8×10^{-10}	6.0×10^{-10}

[a]Indicated by *Seinfeld and Pandis* [2006]

The timescale of coagulation can be estimated by discretizing equation (2.1) and assuming a constant coagulation coefficient. The timescale τ_c is given by the following equation:

$$\tau_c = \frac{2}{\beta N_0}, \tag{2.2}$$

where N_0 is the initial particle concentration. τ_c indicates the time until the concentration of particles becomes half the initial concentration. The timescale shortens as the initial particle concentration increases. For example, the time scale of coagulation of 0.1 μm particles is calculated as $\beta = 10\times10^{-10}$ ($cm^3\ s^{-1}$). The τ_c values of particles with concentrations of 10^3 cm^{-3}, 10^4 cm^{-3}, and 10^6 cm^{-3} are 23 days, 56 hours, and 33 minutes, respectively. When the particle concentration is very high, coagulation occurs very quickly, and the particle number concentration dramatically decreases. On the other hand, for a typical atmospheric particle concentration (10^3-10^4 cm^{-3}), the time scale is about 2-23 days. Therefore, coagulation is an important process in polluted areas, such as in the vicinity of the emission sources, and the timescale of the coagulation increases as the concentration of particles decreases during long-range transport.

2.3. Condensation

As the vapor condenses on particles or the gas evaporates from the particles, the particle size, and the shape of the size distribution change. Assuming that the particles are not in equilibrium with the gas phase, the mass change of the particles due to condensation can be calculated. The change in the mass of particles of particle size D_p, due to the transport of species i between the gas phase and the particle phase, is expressed by the following equation:

$$\frac{dm}{dt} = \frac{2\pi D_p D_i M_i}{RT} f(\mathrm{Kn}, \alpha)\left(P_i - P_{\mathrm{eq},\,i}\right), \tag{2.3}$$

where D_i is the diffusion coefficient for species i in the air, M_i is its molecular weight, $f(\mathrm{Kn}, \alpha)$ is

the correction due to noncontinuum effects and imperfect surface accommodation., R is the gas constant, T is the absolute temperature, P_i is a partial pressure of gas species i near particle surface, and $P_{eq,i}$ is an equilibrium vaper pressure of gas species i. $f(\mathrm{Kn}, \alpha)$ is given by the *Fuchs-Sutugin* [1971] approach as follows:

$$f(\mathrm{Kn}, \alpha) = \frac{0.75\,\alpha\,(1 + \mathrm{Kn})}{\mathrm{Kn}^2 + \mathrm{Kn} + 0.283\,\mathrm{Kn}\,\alpha + 0.75\,\alpha}, \tag{2.4}$$

where Kn is Knudsen number and defined as $2\lambda/D_p$, and α is accommodation coefficient. The difference between the vapor pressure of i far from the particle P_i and the equilibrium vapor pressure $P_{eq,i}$ constitutes the driving force of Equation (2.3) for the transport of species i. Since Knudsen number is the order of $1/D_p$, $f(\mathrm{Kn}, \alpha)$ has the order of D_p. Therefore, Equation (2.4) can be regarded as being proportional to the D_p^2 order, and the condensation process depends on the surface area distribution of the aerosol particles.

High-stability species (sulfate, nitrate, organic matter) formed by the reaction in the gas phase condense to the particle phase. The accommodation coefficient, α shows the resistance of the transport between the particle phase and the gas phase and depends on the condensed species. The typical value of α of HCl, H_2SO_4, NH_4NO_3, organics, BC are 0.15, 0.7 - 0.2, 0.8, 0.02 - 0.2, 0.9, respectively.

Timescale τ_s, at which a species i with a concentration A condenses into particles with a mean diameter D_p, can be approximated by the following equation [*Wexler and Seinfeld*, 1992]:

$$\tau_s \cong \frac{1}{8\pi N D_p D_i f(\mathrm{Kn}, \alpha)}, \tag{2.5}$$

where N is the concentration of particles and D_A is the diffusion coefficient of gas A. According to *Wexler and Seinfeld* [1992], assuming α = 0.1 for polluted environment conditions ($N>10^5$ cm^{-3}, $D_p>0.01$ μm), $\tau_s < 800$ second. This timescale can be on the order of several hours

to several days where the concentration of aerosols is low [*Wexler and Seinfeld*, 1990; *Meng and Seinfeld*, 1996]. In the condensation process, the formation timescale of the condensed gas is also important. The formation of sulfate, nitrate, and organics, which are the major components of aerosol particles, is described in Section 2.5.

2.4. The influence on hygroscopicity by mixing state

In the cloud process, aerosol particles act as CCN and ice nuclei to form liquid particles. The cloud process contributes to both the increase and decrease of the concentration of particles. At the bottom of the cloud, the particles act as CCN and form cloud droplets. The cloud process leads to the irreversible removal of particles from the atmosphere because precipitation removes entrapped particles and gases from the atmosphere through a liquid phase reaction. In particular, the contribution of the sulfate liquid phase reaction is important. However, evaporation of the droplet contributes to the re-entrainment of the particles. The liquid phase reaction produces large particles (aerodynamic particle size around 0.7 μm) that cannot be produced by simple physical processes such as condensation. This particle size is called a droplet mode.

The BC-containing particles show a significantly different effective density, morphology, hygroscopicity, optical properties, and chemical reactivity from pure BC [*Bond et al.,* 2013]. The wet removal by cloud process of these particles is important to control the atmospheric lifetime of BC [*Stier et al.* 2006; *Kipling et al.,* 2016]. The κ-Köhler theory can describe the probability that aerosol particles form clouds. According to the κ-Köhler theory, under sub-saturated or saturated conditions, an equilibrium vapor pressure (S) of a particle surface of particle size D is expressed by the following equation [*Petters and Kreideneweis*, 2007]:

$$S = \frac{\mathrm{RH}}{100} = a_{\mathrm{w}} \exp\left(\frac{4\sigma M_{\mathrm{w}}}{RT\rho_{\mathrm{W}} D}\right), \tag{2.6}$$

where a_{w} is the activity of the water solution, ρ_{w} is the density of water, M_{w} is the molecular weight of water, σ is the surface tension, R is the gas constant, and T is the absolute temperature [*Köhler*, 1936].

a_{w} depends on the solute properties in the solution. The solute effect tends to decrease the equilibrium saturation ratio. The exponential term in Equation (2.6) represents the effect of the curvature of the droplet and tends to increase the equilibrium saturation ratio. Because of these two effects, S, as a function of D, has a maximum value, called critical supersaturation (S_{c}), at the critical diameter (D_{c}). S_{c} is an important parameter that is related to the CCN activity of particles. When a saturation level is larger than S_{c}, droplets rapidly grow.

A single hygroscopic parameter κ represents the CCN activity of mixed particles. According to *Petters and Kreidenweis* [2007], κ is defined by the following equation through the activity of the solution:

$$\frac{1}{a_{\mathrm{w}}} = 1 + \kappa \frac{V_{\mathrm{s}}}{V_{\mathrm{w}}}, \tag{2.7}$$

where V_{s} is the volume of the dry particles and V_{w} is the volume of the water. In a multi-component system, the total volume of the water can be assumed to be the sum of the water contents of the individual components. The value for κ can be expressed by a simple mixing rule as follows:

$$\kappa = \sum_{\mathrm{i}} \kappa_{\mathrm{i}} \frac{V_{\mathrm{si}}}{V_{\mathrm{s}}}, \tag{2.8}$$

where κ_{i} is κ of composition i, and $V_{\mathrm{si}}/V_{\mathrm{s}}$ is the dry volume fraction of composition i compared to the whole particle. The value of κ depends only on the chemical composition of the dry particles and can be physically understood by the volume ratio. If the value of κ is large, the CCN activity is also high. Typical κ values of NaCl, NH_4NO_3, $(NH_4)_2SO_4$, OC, and BC are 1.12, 0.69 - 0.95,

0.53, 0.05 - 0.20, and 0.0, respectively [*Petters and Kreideneis*, 2007; *Huff Hartz et al.,* 2005; *Van Reken et al.,* 2005, *King et al.* 2009; *Hu et al.* 2011]. Because κ values of BC are significantly low compared to those of other compositions, the hygroscopic property of mixed aerosol particle highly depends on the mass fraction of BC.

2.5. Formation process of inorganic materials

2.5.1. Sulfate formation

Sulfate aerosols are secondary particles. Sulfate is the greatest mass contributor to aerosol particles by a single compound on average. The precursor to sulfate is H_2SO_4. In the gas phase, H_2SO_4 is generated by the oxidation of sulfur dioxide (SO_2) by the hydroxyl radical (OH) [*Stockwell and Calvert et al.,* 1983; *Lovejoy and Hanson,* 1996]:

$$SO_2 + OH + M \rightarrow HSO_3 + M. \quad \text{(reaction 2.1)}$$

$$HSO_3 + O_2 \rightarrow HO_2 + SO_3. \quad \text{(reaction 2.2)}$$

$$SO_3 + H_2O + M \rightarrow H_2SO_4 + M. \quad \text{(reaction 2.3)}$$

M is the third body of the reaction. Reaction (2.3) is the rate-determining step. The time constant of this reaction is several days to one week at atmospheric OH levels. Therefore, oxidation of SO_2 into H_2SO_4 occurs mainly on this reaction path during long-range transport [*Seinfeld and Pandis*, 2006]. However, near the main source of SO_2, the pH of precipitation can often decrease due to the concentration of SO_4^{2-}. A reaction to generate SO_4^{2-} more rapidly is required to explain this phenomenon.

SO_2 is also oxidized by a heterogeneous reaction in droplets, such as clouds and fog. SO_2, incorporated in droplets by Henry's law, becomes H_2SO_4 through the following reactions [*Hoffman and Calvert*, 1985]:

$$SO_2(g) + H_2O \rightleftarrows SO_2 \cdot H_2O, \quad \text{(reaction 2.4)}$$

$$SO_2 \cdot H_2O \rightleftarrows H^+ + HSO_3^-, \quad \text{(reaction 2.5)}$$

$$HSO_3^- \rightleftarrows H^+ + SO_3^{2-}. \quad \text{(reaction 2.6)}$$

The time constant of this reaction path is sufficiently faster than the oxidation of SO_2 in the gas phase (2.6) – (2.8). If clouds and fog droplets exist in ambient conditions, H_2SO_4 can be produced within 1 hour [*Seinfeld and Pandis*, 2006]. This reaction path is the most important *in situ* SO_4^{2-}-generating process.

The generated H_2SO_4 tends to condense onto pre-existing particles because of its low vapor pressure. In many cases, H_2SO_4 is immediately neutralized on the particle surface by ammonia (NH_3) and becomes ammonium sulfate ($(NH_4)_2SO_4$). Since the surface area distribution of the aerosols is biased by the accumulation mode, $(NH_4)_2SO_4$ mainly exists in the accumulation mode (0.1 to 2.5 μm in diameter).

2.5.2. Nitrate formation

Almost all nitrates (NO_3^-) are secondary particles. Nitric acid (HNO_3), a precursor of NO_3^-, is mainly produced by the oxidation of nitric oxide radicals (NO_x=NO+NO_2) present in the gas phase, which is caused by ultra violet (UV) radiation [*Rodhe et al.,* 1981]:

$$NO_2 + OH + M \rightarrow HNO_3 + M. \quad \text{(reaction 2.7)}$$

As a result, this reaction can only occur in the atmosphere during the daytime.

At night, HNO_3 is produced by the following reaction path: In the nighttime, HNO_3 is produced by the following reaction path:

$$NO_2 + O_3 \rightarrow NO_3 + O_2, \quad \text{(reaction 2.8)}$$

$$NO_2 + NO_3 \rightarrow N_2O_5 + M, \quad \text{(reaction 2.9)}$$

$$N_2O_5 + H_2O \rightarrow 2H^+ + 2NO_3^-. \quad \text{(reaction 2.10)}$$

As OH is formed by photochemical reactions, and NO_3 is easily photolyzed, reactions (2.8) - (2.10) dominate at night [*Pathak et al.,* 2009]. The time constant of HNO_3 production is about one day by reaction (2.12) and about 1 hour in the night. The lifetime of NO_x is about one day on

average.

Since HNO_3 has a high saturation vapor pressure, it does not move directly to the particle phase. When HNO_3 adheres to the surface of existing particles, it is neutralized by surrounding NH_3 and exists in the particle phase as ammonium nitrate (NH_4NO_3).

$$HNO_3 + NH_3 \rightleftarrows NH_4NO_3. \qquad \text{(reaction 2.11)}$$

This equilibrium reaction is strongly dependent on temperature and humidity. When the temperature is high, reaction (2.16) is biased toward HNO_3. Since NO_3^- formation is faster than SO_4^{2-} formation, the concentration of NO_3^- may exceed that of SO_4^{2-} in urban fine particles. As well as SO_4^{2-}, NO_3^- also exists mainly in the accumulation mode.

2.6. Formation rate of BC-containing particles

BC particles released into the atmosphere undergo condensation, heterogeneous reactions with inorganic and organic gases, and coagulation with other particles. As a result, the BC particles form internally mixed particles, which include other components. Although the formation rate of the BC-containing particles depends on the surrounding gas and particle concentrations, observational knowledge is insufficient [*Bond et al.*, 2013]. Several observations have suggested that a sufficiently thick coating was obtained in about 1 – 5 day [*Moteki and Kondo*, 2007; *Moffet and Prather*, 2009]. Also, in numerical calculations, the formation rate of BC-containing particles is often assumed to be roughly 1 - 5 days [*Jacobson et al.,* 2001; *Aquila et al.*, 2011].

Reference

Aquila, V., et al. (2011), MADE‐in: A new aerosol microphysics submodel for global simulation of insoluble particles and their mixing state, *Geosci. Model Dev.*, 4, 325-355, doi:10.5194/gmd‐4‐325‐2011.

Bond, T. C., Doherty, S. J., Fahey, D. W., Forster, P. M., Berntsen, T., DeAngelo, B. J., Flanner, M. G., Ghan, S., Karcher, B., Koch, D., Kinne, S., Kondo, Y., Quinn, P. K., Sarofim, M. C., Schultz, M. G., Schulz, M., Venkataraman, C., Zhang, H., Zhang, S., Bellouin, N., Guttikunda, S. K., Hopke, P. K., Jacobson, M. Z., Kaiser, J. W., Klimont, Z., Lohmann, U., Schwarz, J. P., Shindell, D., Storelvmo, T., Warren S. G., and Zender, C. S. (2013). Bounding the Role of Black Carbon in the Climate System: A Scientific Assessment, *J. Geophys. Res.*, 118: 1-173.

Hu, D., Chen, J., Ye, X., Li, L., and Yang, X. (2011) Hygroscopicity and Evaporation of Ammonium Chloride and Ammonium Nitrate: Relative Humidity and Size Effects on the Growth Factor. *Atmos. Environ.*, 45, 14, 2349-2355

Fuchs, N. A., and Sutugin, A. G., (1971) High Dispersed aerosols, in Topics in Current Aerosol Research (Part2), G. M. Hidy and J. R. Brock, *eds., Pergamon*, New York, pp. 1-200.

Huff Hartz, K. E., Rosenorn, T., Ferchak, S. R., Raymond, T. M., Bilde, M., Donahue, N. M., and Pandis, S. N. (2005). Cloud condensation nuclei activation of monoterpene and sesquiterpene secondary organic aerosol, *J. Geophys. Res*. 110:D14208, doi:10.1029/2004JD005754.

Jacobson, M. Z. (2001), Strong radiative heating due to the mixing state of black carbon in atmospheric aerosols, *Nature,* 409, 695-697.

Jacobson, M. Z. (2005), Fundamentals of Atmospheric Modeling, 2nd ed.,813 pp., *Cambridge Univ. Press*, New York.

King, S. M., Rosenoern, T., Shilling, J. E., Chen, Q., and Martin, S. T. (2009). Increased cloud activation potential of secondary organic aerosol for atmospheric mass loadings, *Atmos. Chem. Phys*. 9:2959-2971.

Kipling, Z., et al. (2016), What controls the vertical distribution of aerosol? Relationships between process sensitivity in HadGEM3-UKCA and inter‐model variation from AeroCom phase II,

Atmos. Chem. Phys., 16(4), 2221-2241.

Köhler, H. (1936) The nucleus in and the growth of hygroscopic droplets. Tram. Faraday Soc. 32, 1152.

Lovejoy, E. R., and Hanson, D. R. J., (1996), Kinetics and Products of the Reaction SO3+NH3+N2. *Phys. Chem.* 100 (11), 4459-4465.

Meng, Z., and Seinfeld, J. H., (1996) Timescales to achieve atmospheric gas-aerosol equilibrium for volatile species, *Atmos. Environ.,* 30, 2889-2900.

Moffet, R. C., and K. A. Prather (2009), In‐situ measurements of the mixing state and optical properties of soot with implications for radiative forcing estimates, *P. Natl. Acad. Sci. USA*, 106(29), 11872?11877.

Moteki, N., and Y. Kondo (2007), Effects of mixing state on black carbon measurements by laser‐induced incandescence, *Aerosol Sci. Technol.*, 41(4), 398?417, doi:10.1080/02786820701199728.

Muller, H., (1928), Zur allegemeinen Theorie der rascen Koagulation. Die koagulation von Stabchen und Blattchen-kolloiden; die Theorie beliebig polydisperser Systeme und der Stromungskoagulation. *Kolloidbeibefte*, 27, 223-50.

Pathak, R. K., Wu, W. S., and Wang, T., (2009) Summertime PM2.5 Ionic Species in Four Major Cities of China: Nitrate Formation in an Ammonia-Deficient Atmosphere. *Atmos. Chem. Phys.*, 9, 1711-1722.

Petters, M. D.and Kreidenweis, S. M., (2007) A Single Parameter Representation of Hygroscopic Growth and Cloud Condensation Nucleus Activity Atmos. Chem. Phys., 7, 1961-1971

Rodhe, H., Crutzen, P., and Vanderpol, A., (1981) Formation of Sulfuric and Nitric-Acid in the Atmosphere during Long-Range Transport. *Tellus*, 33, 132-141.

Seinfeld, J. H., and Pandis, S. N., (2006) Atmospheric Chemistry and Physics?From Air Pollution to Climate Change, 2nd ed.; *John Wiley & Sons*: Hoboken, NJ, 2006.

Stier, P., J. H. Seinfeld, S. Kinne, J. Feichter, and O. Boucher (2006), Impact of nonabsorbing anthropogenic aerosols on clear‐sky atmospheric absorption, *J. Geophys. Res.*, 111(D18), D18201, doi:10.1029/2006JD007147.

Stockwell, W. R., J. G. Calvert, (1983) The mechanism of the HO‐SO2 reaction, *Atmos. Environ.*, 17, 2231-2235.

VanReken, T. M., Ng, N. L., Flagan, R. C., and Seinfeld, J. H. (2005). Cloud condensation nucleus activation properties of biogenic secondary organic aerosol, *J. Geophys. Res.* 110: D07206, doi:10.1029/2004JD005465.

Wexler, A. S., and Seinfeld, J. H., (1990) The Distribution of Ammonium Salts among a Size and Composition Dispersed Aerosol, *Atmos. Emviron*. 24A, 1231-1246.

Wexler, A. S., and Seinfeld, J. H., (1992) Analysis of Aerosol Ammonium Nitrate: Departures from Equilibrium during SCAQS, *Atmos. Environ.* 26A, 579-591.

Zhang, R., Khalizov, A. F., Pagels, J., Zhang, D., Xue, H., and McMurry, P. H. (2008) Variability in Morphology, Hygroscopicity, and Optical Properties of Soot Aerosols during Atmospheric Processing Proc. *Natl. Acad. Sci. U.S.A*., 105, 10291-10296.

3. Evaluation of a particle trap laser desorption mass spectrometer (PT-LDMS)

3.1. Introduction

Online measurements of aerosols are important for improving our understanding of the formation and loss processes of ambient aerosols. In particular, quantification of the mass concentration of sulfate aerosols is of high priority because sulfate aerosols are typically the major components of fine particulate mass in the troposphere [e.g. *Altshuller* 1973, *Drewnick et al.* 2003, *Hogrefe et al.* 2004. Ammonium sulfate ($(NH_4)_2SO_4$) is the predominant form of sulfate aerosols found in urban areas and in regions significantly affected by anthropogenic emissions [e.g., *Saltzman et al.* 1983, *Pilinis and Seinfeld* 1987, *Schwab et al.* 2004].

The instruments currently employed for online measurements of sulfate aerosols are roughly categorized into dry and wet methods. Dry methods are often based on thermal desorption techniques and include the Aerodyne aerosol mass spectrometer (AMS; Aerodyne Research Inc., USA) [*Jayne et al.* 2000, thermal desorption chemical ionization mass spectrometer (TDCIMS) [*Voisin et al.* 2003], and sulfate particulate analyzer (SPA; Thermo-Scientific, USA) [*Schwab et al.* 2006]. Wet methods are based on online water extraction techniques followed by chemical analysis; these methods include a steam jet aerosol collector (SJAC) [*Khlystov et al.* 1995] and particle-into-liquid sampler (PILS) [*Weber et al.* 2001]. They are often coupled with ion chromatography for the quantification of bulk compositions of aerosols.

Among these instruments, the Aerodyne AMS has been utilized by a number of researchers, and useful insights into the formation of sulfate aerosols have been reported [e.g., *Zhang et al.* 2005; 2007]. Generally, the routine calibration of an AMS is performed using pure ammonium

nitrate (NH_4NO_3) particles because of the high particle collection efficiency (CE) for NH_4NO_3. The quantification of sulfate aerosols in ambient air is performed by assuming representative values of CE and relative ionization efficiency (RIE) [*Allan et al.* 2003]. As discussed below, the thermal decomposition products of $(NH_4)_2SO_4$ are known to significantly vary depending on the temperature of the vaporizer. In fact, earlier AMS studies indicated that the detection efficiency of $(NH_4)_2SO_4$ exhibited a significant dependence on the vaporizer temperature [*Alfarra* 2004]. For these reasons, there is a need to revisit the quantification of sulfate aerosols by thermal decomposition techniques and to reconsider the choice of appropriate materials for calibration.

We have developed a particle trap laser desorption mass spectrometer (PT-LDMS) and demonstrated the proof of concept [*Takegawa et al.* 2012]. The PT-LDMS developed has been categorized as a dry method, as mentioned previously. This is the first report of quantification of mass concentrations of ambient sulfate aerosols by the PT-LDMS. Laboratory experiments for determining the operating conditions of the PT-LDMS and intercomparisons with other instruments, including an SPA and a filter sampling method, are presented. Possible uncertainties in quantification by the PT-LDMS and SPA are discussed in detail.

3.2. Experimental

3.2.1. PT-LDMS

The hardware and data acquisition software have been used according to the previous version reported by *Takegawa et al.* [2012] with some modifications. A schematic diagram of the PT-LDMS used in this study is shown in Figure 3.1. Herein, we summarize the important specifications. Aerosol particles are introduced into a vacuum chamber through an aerodynamic lens [*Liu et al.* 1995]. The majority of gas molecules contained in sample air can be removed by a

skimmer cone, which results in a concentration of aerosol particles along the centerline of the lens [*Allan et al.* 2003]. Aerosol particles are collected on a particle trap comprised of layers of micro-structured mesh and are subsequently vaporized by a carbon dioxide (CO_2) laser (ULR-10, Universal Laser System, Inc., USA). The vaporization mechanism included both direct heating of aerosol particles due to light absorption and thermal conduction from the heated surface of the particle trap, as described in *Takegawa et al.* [2012]. The particle trap is enclosed by an Au-coated aluminum cell (a quartz cell was used in the previous version), which is connected to a quadrupole mass spectrometer (QMS; gas-tight ionizer type, PrismaPlus, Pfeiffer Vacuum, GmbH, Germany). The vaporized gas from collected aerosol particles is ionized by electron impact ionization (EI) with an electron energy of 60 eV. Ion currents at some selected *m/z* values ($I_{m/z}$) are detected by a secondary electron multiplier (SEM) using the multiple ion detection mode of the QMS.

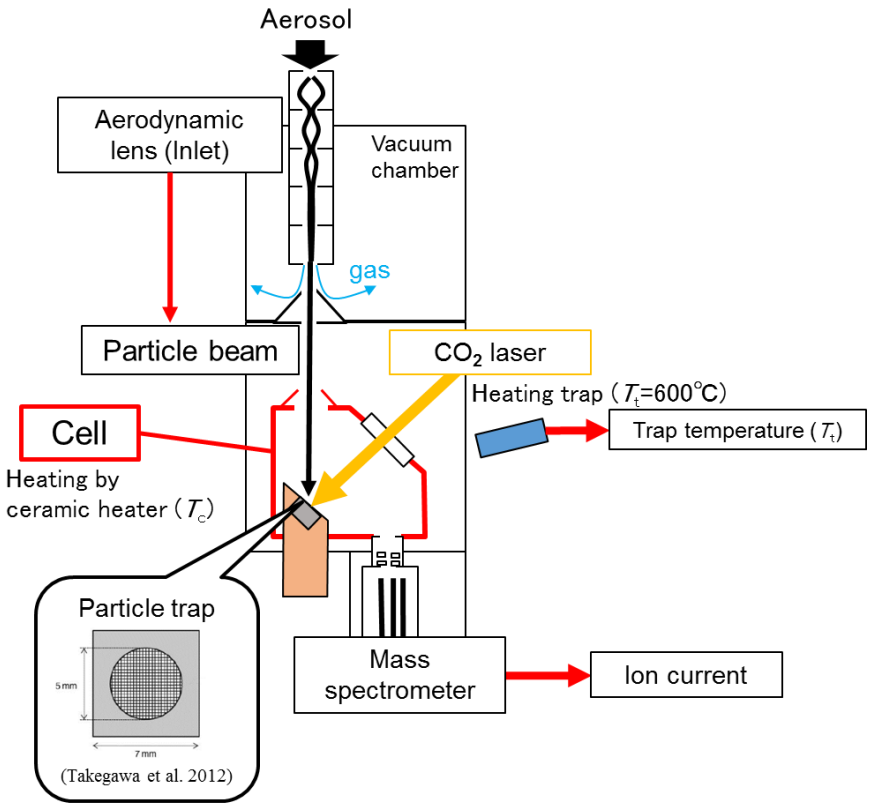

Figure 3.1. Schematic diagram of the PT-LDMS.

Compared to the previous version presented by *Takegawa et al.* [2012], the coating material of the trap was changed from pure Pt to a mixture of Pt and W to increase the melting point. The separation distance between the mesh layers was changed from 200 to 250 μm to facilitate machining. A 20-μm-thick Au film was inserted between the particle trap and holder to improve thermal conductivity. The trap holder was cooled by circulating water at 15°C. A small gap was introduced between the holder and the cell for improving thermal insulation. These modifications enable heating of the cell and cooling of the trap. The former is necessary to reduce the adsorption of the evolved gas, while the latter is needed to reduce the loss of particle compounds by evaporation during collection.

The laser power (P_{laser}) was continuously monitored using a beam splitter and thermopile sensor. A beam homogenizer (Sumitomo Electric, Japan) was installed in the optical path for generating a nearly top-hat-shaped laser beam, although the shape of the actual beam at the position of the particle trap was not precisely measured. This is beneficial both in terms of homogeneous heating of the particle trap and avoiding penetration of the trap by the laser beam. A radiation thermometer (IGA140, LumaSense Technologies, Inc., USA) was placed outside the chamber for monitoring the temperature of the particle trap. The thermometer observed near-infrared radiation emitted from the trap heated by the laser passing through a quartz window of the vacuum chamber. Note that the temperature data should be treated as a lower limit because the emissivity of the trap and the transmission efficiency of the quartz window were both assumed to be unity.

The total measurement cycle was 15 min including the time for particle collection, laser desorption analysis, cooling of the trap, and buffer time for stabilization. After aerosol particles in sample air were collected on the particle trap for 7 min, the inlet valve was closed (SS-43GF4 with

MS-142ACX, Swagelok, Inc., USA). The laser was switched on for 1.5 min to detect the gas evolved from collected particles 1 min after the inlet valve had been closed. The inlet valve was kept closed for 5.5 min after the laser was switched off for cooling the trap.

The inlet flow rate of the PT-LDMS was calibrated using a standard flow meter (DryCal DC-Lite Air Flow Calibrator, Brandt Instruments, Inc., USA). The mass concentration is expressed in units of $\mu g\ m^{-3}$ at 25°C and 1 atm.

3.2.2. Other Instruments

The SPA quantifies the mass concentration of sulfate aerosols by a thermal decomposition/reduction method coupled with a sulfur dioxide (SO_2) monitor [*Schwab et al.* 2006]. Sulfate aerosol particles are reduced to SO_2 in a converter tube heated to 1000°C and subsequently detected by a pulsed UV fluorescence method. The detected signals include signals from sulfate aerosols and those from gas-phase SO_2. We did not use a denuder to remove gas-phase interference. The mass concentration of sulfate was calculated by subtracting the data obtained for particle-free air (zero air) from the data obtained for particle-loaded air.

Filter sampling and analysis were performed by Murata Corp (http://www.murata-s.co.jp/). $PM_{2.5}$ samples were collected using a $PM_{2.5}$ aerosol sampler (MCAS-SJ, Murata Keisokuki Service, Co. Ltd., Japan) and subsequently analyzed by ion chromatography in the laboratory. *Miyakawa et al.* [2015] described the collection and analysis procedure in detail.

3.2.3. Laboratory Experiment

The dependence of the sensitivity on P_{laser} and cell temperature (T_{cell}) was investigated in the laboratory prior to ambient measurements. The particle generation and evaluation system was

practically the same as that described by *Takegawa et al.* [2005]. It consisted of a Collison atomizer (Model 3076, TSI, Inc., USA), diffusion dryer, differential mobility analyzer (DMA; Model 3081, TSI, Inc., USA), and condensation particle counter (CPC, Model 3022, TSI, Inc., USA). Monodisperse aerosols with known chemical compositions were generated and introduced into the PT-LDMS.

We used $(NH_4)_2SO_4$ particles for the laboratory experiment because they are typically the predominant form of sulfate aerosols in urban air. As described by *Takegawa et al.* [2012], major fragments of $(NH_4)_2SO_4$ were observed at m/z 48 (SO^+) and 64 (SO_2^+). A mobility diameter (d_m) of 250 nm was chosen for most of the experiments because of the high particle transmission efficiency through the aerodynamic lens at this diameter [*Miyakawa et al.* 2014]. The effect of multiply charged particles was estimated using the same method as that described by *Takegawa and Sakurai* [2011] to calculate the mass of sulfate introduced into the PT-LDMS.

In addition to $(NH_4)_2SO_4$, potassium nitrate (KNO_3) was used as the reference because of its simple molecular structure and fragmentation pattern [*Takegawa et al.* 2012]. Details of the experimental results for KNO_3 particles are given in the supplementary material. The quantification of nitrate aerosols is also an important issue, but it is beyond the scope of this paper. A detailed investigation of nitrate aerosols, including KNO_3 and NH_4NO_3, is currently underway and will be presented elsewhere.

3.2.4. Ambient Measurements

Ambient measurements were performed in November 2013 at a building on the campus of the Research Center for Advanced Science and Technology, the University of Tokyo. Although the intercomparison was also performed in March 2013, as qualitatively discussed by *Miyakawa*

et al. [2014], their data were not utilized in this study. Figure 3.2 shows the experimental setup for the ambient measurements. Ambient air aspirated from a window was introduced into a buffer box so that all of the instruments could take samples from the same air volume. The inner surface of the buffer box was coated with aluminum foils and grounded to avoid electrostatic charges. The filter samples were collected every 12 h. The SPA and PT-LDMS were equipped with a $PM_{2.5}$ cyclone (URG-2000-30EH, URG, Inc., USA), while the size cut of the PT-LDMS was approximated as PM_1 (limited by the transmission efficiency of the aerodynamic lens).

The zero levels of the PT-LDMS signals were measured every hour by replacing the sample air with zero air generated using a high-efficiency particulate air (HEPA) filter. The PT-LDMS was routinely calibrated using monodisperse $(NH_4)_2SO_4$ particles during the measurement period by the particle generation system described in section 3.2.3.

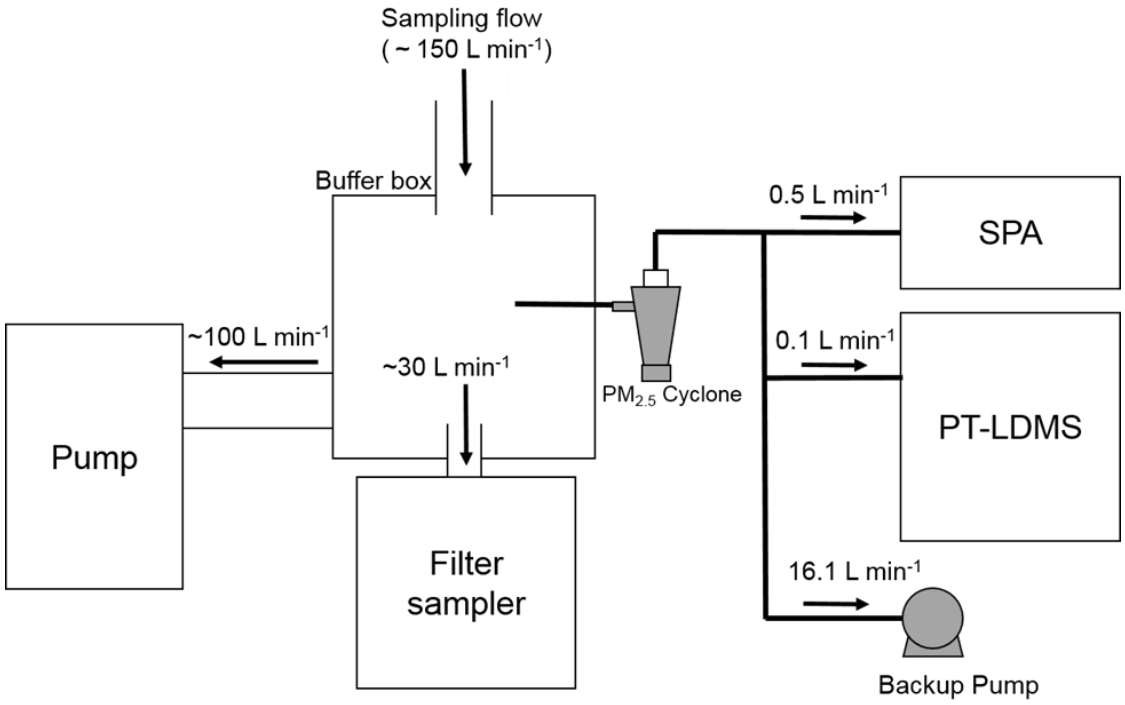

Figure 3.2. Schematic diagram of the experimental set up for ambient measurements.

The zero levels of the SPA signals were measured every hour using a three-way valve and a HEPA filter placed upstream of the converter. The valve was switched between particle-loaded and zero air. Although the SO_2 monitor of the SPA was calibrated using SO_2 standard gas prior to the measurement period, the overall calibration of the SPA was performed using monodisperse $(NH_4)_2SO_4$ particles after the period. The three-way valve was not used for the correction of gas-phase SO_2 during the calibration because a substantial amount of SO_2 outgas from the DMA was present, presumably originating from HEPA filters for generating sheath air. Instead, the contribution of gas-phase SO_2 was estimated by turning off the high voltage of the DMA.

3.2.5. Data Reduction

PT-LDMS

As described in section 3.2.1, ion currents at some selected *m/z* values were detected (*m/z* 14, 16, 28, 30, 44, 48, 55, and 64). The *m/z* 14 signal was dominated by N^+ originating from the nitrogen present in ambient air with the inlet valve open, and was used to correct for the temporal drift of the ion detection efficiency. A similar correction process was also carried out by *Takegawa et al.* [2012], who used *m/z* 32 (O_2^+) instead of *m/z* 14. Although this section focusses on the quantification of sulfate aerosols, the equations presented here are also applicable to other compounds such as nitrate.

Table 3.1 summarizes the key parameters used in this study and their abbreviations. The ion current above the background level was accumulated over the laser irradiation time to obtain an integrated ion signal at each *m/z* ($Q^{X}_{m/z}$). Note that the superscript X (= "amb" or "cal") represents ambient or calibration conditions, respectively. The mass concentration of sulfate (M^{X}_{MS}) was calculated using the difference in the integrated ion signal between particle-loaded and zero air

(net integrated ion signal, $\Delta Q^{X}_{m/z}$):

$$M^{X}_{MS} = \frac{\Delta Q^{X}_{m/z}}{S_{m/z}\, V} \ , \tag{3.1}$$

where V is the sampled air volume, and $S_{m/z}$ is the sensitivity for sulfate aerosols at the corresponding m/z value. $\Delta Q^{X}_{m/z}$ is expressed as follows:

$$\Delta Q^{X}_{m/z} = Q^{X}_{m/z,\,\mathrm{particle}} - Q^{X}_{m/z,\,\mathrm{zero}} \ , \tag{3.2}$$

where $Q^{X}_{m/z,\,\mathrm{particle}}$ is the integrated ion signal at m/z for particle-loaded air and $Q^{X}_{m/z,\,\mathrm{zero}}$ is the integrated ion signal at m/z for zero air. Using monodisperse aerosol particles generated and quantified by the DMA and CPC system, the average mass concentration of sulfate aerosols introduced into the PT-LDMS during a calibration cycle (M^{cal}_{CPC}) can be calculated as follows:

$$M^{cal}_{CPC} = \frac{\pi}{6}\, d^{3}_{m}\, \rho\, N_{CPC}\, f_{corr}\, R_{SO4} \ , \tag{3.3}$$

where d_m is the mobility diameter of calibration particles classified by the DMA, ρ is the particle density, N_{CPC} is the number concentration of particles measured by the CPC, f_{corr} is the correction coefficient for the multiple-charge effect estimated by a method similar to *Wang et al.* [2010] (see appendix), and R_{SO4} is the molecular fraction of SO_4^{2-} in $(NH_4)_2SO_4$. The $S_{m/z}$ values are then given as follows:

$$S_{m/z} = \frac{\Delta Q^{cal}_{m/z}}{M^{cal}_{CPC}\ V} \ . \tag{3.4}$$

These equations are also used to estimate possible uncertainties in quantification (section 3.4.3).

Table 3.1. Key factors affecting quantification

Instrument	Parameter	Definition	Remark
PT-LDMS	$I_{m/z}$	Ion current at *m/z*	a
	$M_{\mathrm{MS}}^{\mathrm{X}}$	Mass concentration measured by the PT-LDMS	a
	$\Delta Q_{m/z}^{\mathrm{X}}$	Net integrated ion signals at *m/z*	a
	$Q_{m/z,\ \mathrm{particle}}^{\mathrm{X}}$	Integrated signal at *m/z* for particle-loaded air	a
	$Q_{m/z,\ \mathrm{zero}}^{\mathrm{X}}$	Integrated signal at *m/z* for particle-free air (zero air)	a
	$S_{m/z}$	Sensitivity determined by calibrations	a
	Tr^{X}	Transmission efficiency of the aerodynamic lens	
	CE^{X}	Collection efficiency of particles	
	Y^{X}	Vaporization efficiency of particle compounds	
	α^{X}	Adsorption fraction of SO_2 on the cell surface	
	IE^{X}	Ionization efficiency for evolved gas	
	$f_{m/z}^{\mathrm{X}}$	Fragment ratio at *m/z*	
SPA	$M_{\mathrm{SPA}}^{\mathrm{X}}$	Mass concentration measured by the SPA	a
	$\Delta\chi^{\mathrm{X}}$	Net mixing ratio of SO_2 measured by the SO_2 monitor	a
	$\chi_{\mathrm{particle}}^{\mathrm{X}}$	Mixing ratio of SO_2 for particle-loaded air	a
	$\chi_{\mathrm{zero}}^{\mathrm{X}}$	Mixing ratio of SO_2 for zero air	a
	F_{SPA}	Calibration factor of the SPA	
	ε^{X}	Conversion efficiency of sulfate to SO_2	
	$\chi_{\mathrm{gas}}^{\mathrm{X}}$	Mixing ratio of gas-phase SO_2 in sampling air	
Others	$M_{\mathrm{CPC}}^{\mathrm{cal}}$	Mass concentration of calibration particles quantified using the CPC	a
	V	Sampled air volume	a
	d_{m}	Mobility diameter classified by the DMA	a
	ρ	Density of the calibration material	a
	N_{CPC}	Number concentration measured by the CPC	a
	f_{corr}	Correction coefficient for the multiple-charge effect	a
	$M_{\mathrm{true}}^{\mathrm{X}}$	"True" mass concentration of aerosol particles	

The superscript X (= "amb" or "cal") denotes ambient or calibration conditions, respectively.

The subscripts represent the species, instruments, or mode of measurements.

a: These values were explicitly determined by calibrations or ambient measurements.

SPA

The mass concentration of sulfate aerosols measured by the SPA (M^{X}_{SPA}) was calculated using the difference of the mixing ratio of SO_2 between particle-loaded and zero air (net SO_2 mixing ratio, $\Delta\chi^{X}$):

$$M^{X}_{SPA} = \Delta\chi^{X} F_{SPA}. \quad (3.5)$$

$\Delta\chi^{X}$ is expressed as follows:

$$\Delta\chi^{X} = \chi^{X}_{particle} - \chi^{X}_{zero} , \quad (3.6)$$

where $\chi^{X}_{particle}$ is the mixing ratio of SO_2 for particle-loaded air, and χ^{X}_{zero} is the mixing ratio of SO_2 for zero air. F_{SPA} is the correction factor determined by calibration:

$$F_{SPA} = \frac{M^{cal}_{CPC}}{\Delta\chi^{cal}} . \quad (3.7)$$

Notably, both M^{X}_{MS} and M^{X}_{SPA} were scaled to the same standard, which is critical for the interpretation of the intercomparison results.

3.3. Results

3.3.1. Laboratory Experiment

The radiation temperature of the particle trap was primarily controlled by P_{laser} density and thermal properties of the trap (i.e., absorbance and thermal conductance). Figure 3.3 shows an example of the P_{laser} and radiation temperature profiles at a certain laser power setting. The P_{laser} was modulated (overshoot at the beginning) to achieve a rapid evolution of radiation temperature. The P_{laser} and trap temperature (T_{trap}) were estimated using data points between 30 and 90 s after the laser was switched on (i.e., “plateau time period”).

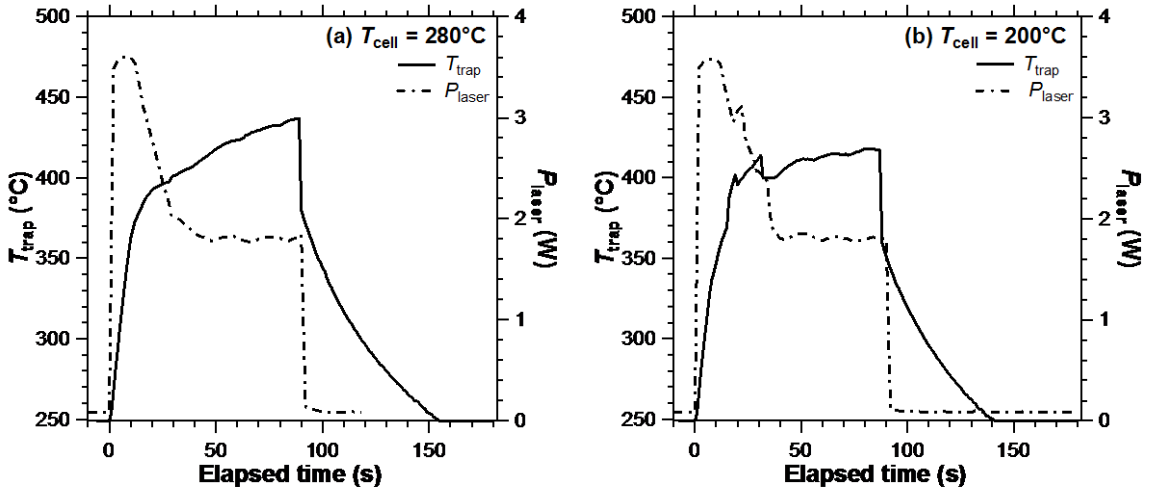

Figure 3.3. Example of T_{trap} (solid line, left axis) and P_{laser} (dashed line, right axis) profiles at a T_{cell} of (a) 280°C and (b) 200°C.

We measured the sensitivity under various P_{laser} (T_{trap}) and T_{cell} conditions. Figure 3.4 shows the evolution of the *m/z* 48 ion currents for $(NH_4)_2SO_4$ particles obtained at a P_{laser} of ~4 W (T_{trap} of ~550°C) and T_{cell} values of 200 and 280°C. The accumulated mass of sulfate was 18 and 8 ng for T_{cell} = 200 and 280°C conditions, respectively. The ion current for T_{cell} = 200°C was scaled down by a factor of 0.44 (= 8/18) to clarify the comparison of two signals. The ion current signal was characterized by a sharp peak immediately after the laser was switched on and a broad peak 10 s after the laser was switched on. This result suggests that the particle vaporization process consisted of at least two thermal desorption mechanisms, as mentioned earlier. Notable changes were observed for the ion current at *m/z* 48 for $(NH_4)_2SO_4$ in the latter time period of laser irradiation (30–90 s) with increasing T_{cell}.

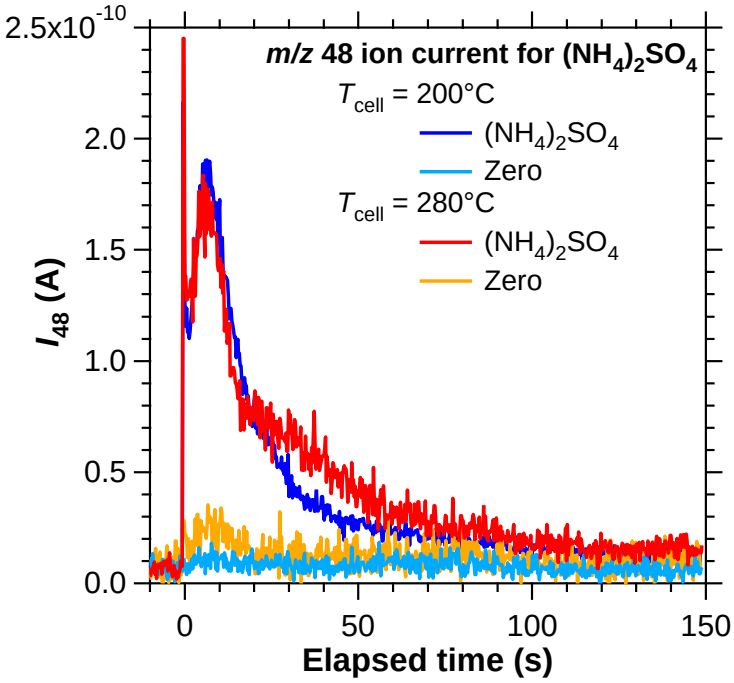

Figure 3.4. Evolution of mass normalized *m/z* 48 ion current for $(NH_4)_2SO_4$ particles obtained at a T_{trap} of ~550°C and a T_{cell} of 200°C (blue and turquoise lines) and 280°C (red and orange lines). The accumulated mass of sulfate was 18 and 8 ng for T_{cell} = 200 and 280°C conditions, respectively. The ion current for T_{cell} = 200°C was scaled down by a factor of 0.44 (= 8/18) to clarify the comparison of two signals.

Figure 3.5a shows the relationship between T_{trap} and P_{laser} under three T_{cell} conditions. The relationship did not show significant dependence on the T_{cell} conditions. Figure 3.5b summarizes the results of the temperature experiments. Although substantial scatter was observed in the data, the dependence of the sensitivity on T_{cell} appeared to be more significant than that on P_{laser} (T_{trap}) for $(NH_4)_2SO_4$. Higher T_{cell} conditions tended to exhibit higher sensitivity for $(NH_4)_2SO_4$ particles. As mentioned in section 3.2.3, major fragments of $(NH_4)_2SO_4$ were observed at *m/z* 48 and 64, and detectable amounts of other sulfur-related signals such as *m/z* 80 (SO_3^+) and 98 ($H_2SO_4^+$) were not observed. The ΔQ_{64}^X to ΔQ_{48}^X ratio can be used as a diagnostic for desorption because this ratio can vary depending on the chemical form of sulfur compounds (SO_2, sulfuric acid, or others).

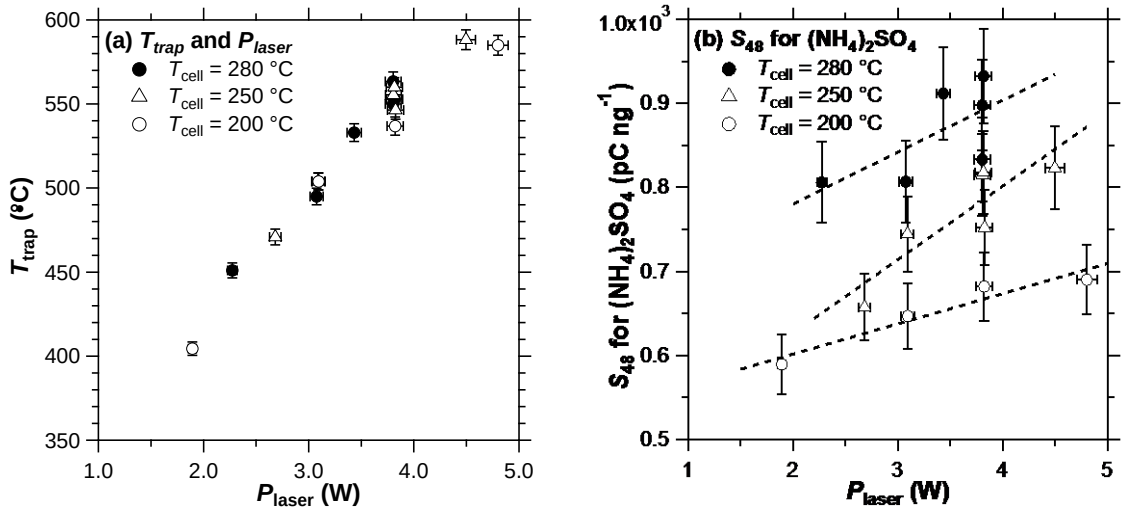

Figure 3.5. (a) Scatter plot of T_{trap} versus P_{laser} from laboratory experiments. (b) Dependence of sulfate sensitivity on P_{laser} at various T_{cell} values. T_{cell} value for the experiment were selected as 280°C (filled circle), 250°C (triangle), and 200°C (open circle). Dashed lines denote the regression lines of each dataset in (b). Error bars depict the uncertainty originating from the random error of PT-LDMS (4%), CPC (2%), radiation thermometer (1%) and thermopile sensor (1%).

Figure 3.6 shows the scatter plot of ΔQ_{64}^{cal} versus ΔQ_{48}^{cal} obtained during laboratory experiments. Previous studies have reported that the thermal decomposition products of $(NH_4)_2SO_4$ mainly consist of SO_2 above ~400°C and that the decomposition products vary below ~400°C [*Kiyoura and Urano* 1970]. According to the EI (70eV) mass spectrum database provided by the National Institute of Standard Technology (NIST) (http://webbook.nist.gov/chemistry/), the ΔQ_{64}^{X} to ΔQ_{48}^{X} ratio can differ significantly depending on the chemical form of sulfate compounds (SO_2, H_2SO_4 etc.). The observed $\Delta Q_{64}^{cal}/\Delta Q_{48}^{cal}$ value from $(NH_4)_2SO_4$ was ~1.4 with a high correlation coefficient (r^2 ~ 0.99). Although we did not directly identify the chemical form of sulfur compounds in the evolved gas, the tight correlation suggests that the thermal decomposition products of $(NH_4)_2SO_4$ can be regarded as uniform.

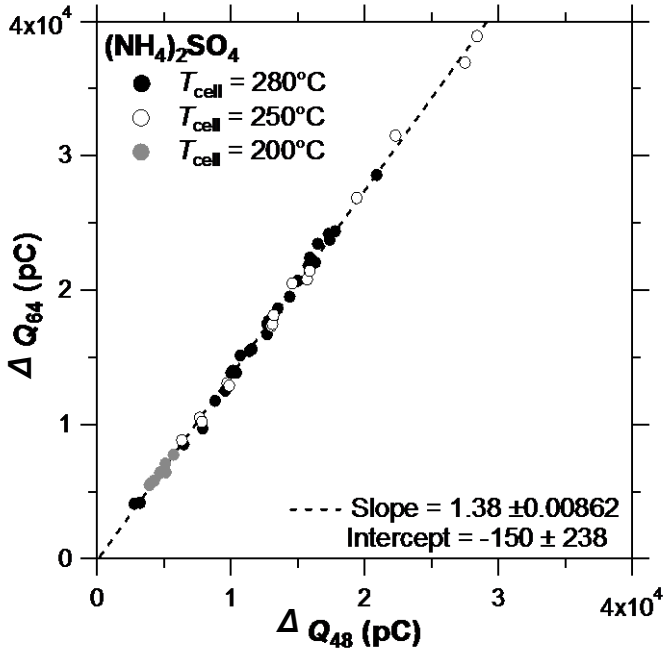

Figure 3.6. Correlation plots of ΔQ_{64}^{cal} versus ΔQ_{48}^{cal} from the laboratory experiments (filled circle: T_{cell} = 280°C, open circle: T_{cell} = 250°C, shaded circle: T_{cell} = 200°C). The data points for T_{cell} = 250°C includes routine calibrations during ambient measurements. The dashed line denotes the regression line for the entire data (r^2 = 0.998).

3.3.2. Ambient Measurements

Figure 3.7 shows the time series of the average ion current at *m/z* 14 (reference signal) with the inlet open and the sensitivities for sulfate and nitrate during the laboratory experiment (October 2013) and ambient measurement (November 2013). The sensitivity for nitrate was determined using KNO_3 as a calibration material (section 2.2.3). The reference signal changed in accordance with changes in the SEM voltage. The sensitivity for sulfate exhibited a large decrease over the course of a few days following the start of the ambient measurements, while the sensitivity for nitrate exhibited a slight decreasing trend. The sensitivity recovered after the replacement of the particle trap; however, it exhibited a similar decreasing trend again. Such a drastic change was not observed during the laboratory experiment or ambient measurement in March 2013 [*Miyakawa et al.* 2014]. A scanning electron microscopy observation indicated that the Pt/W coating was

partially detached from the particle trap surface (not shown), which could have caused the decrease in the sulfate sensitivity. The particle trap was replaced when the sensitivity for sulfate was decreased to ~200 pC ng^{-1}, although optimal timing of the replacement of the particle trap is still under consideration.

Figure 3.8 shows the scatter plot of ΔQ_{64}^{amb} versus ΔQ_{48}^{amb} obtained during ambient measurements. For comparison, the regression line from the laboratory experiment is also shown. The $\Delta Q_{64}^{amb} / \Delta Q_{48}^{amb}$ values for ambient aerosol particles showed good agreement with the laboratory data within a variation of 15%, indicating that the thermal desorption products from ambient sulfate aerosol particles were very similar to those from $(NH_4)_2SO_4$ particles generated in the laboratory.

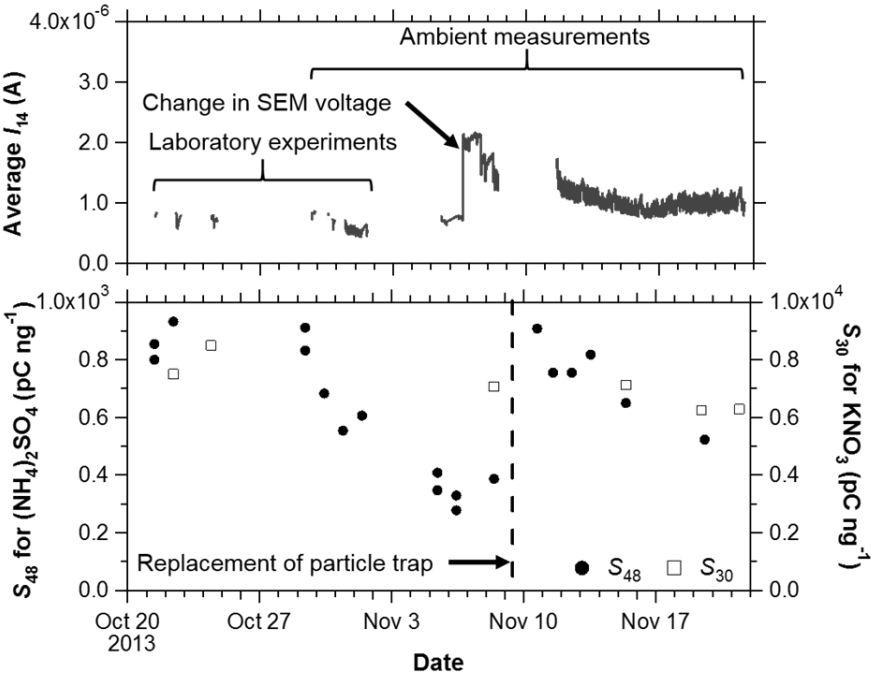

Figure 3.7. Temporal changes in (a) the average of *m/z* 14 ion current and (b) sensitivity of sulfate (filled circle) and nitrate (open square) during laboratory experiments and ambient measurements. The particle trap was replaced on November 9. The sensitivity data include the laboratory experiments and routine calibrations. There was an overlap between ambient measurement and laboratory experiment periods because some laboratory experiments were performed during the ambient measurement period.

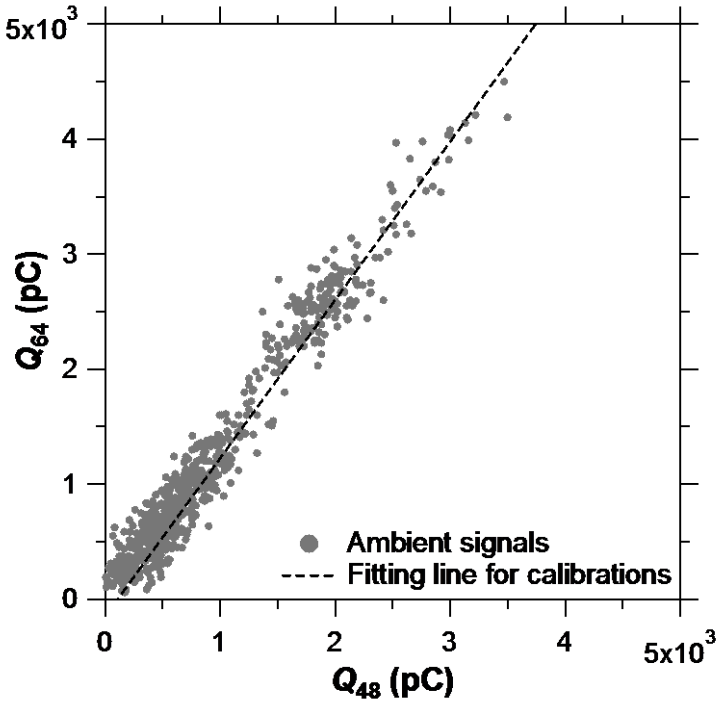

Figure 3.8. Correlation plots of $\Delta Q_{64}^{\mathrm{amb}}$ versus $\Delta Q_{48}^{\mathrm{amb}}$. The dashed line denotes the regression line shown in Figure 2.5.

Figure 3.9a shows the time series of $Q_{48,\,\mathrm{particle}}^{\mathrm{amb}}$ and $Q_{48,\,\mathrm{zero}}^{\mathrm{amb}}$ during ambient measurement period. The zero air signals were found to exhibit a positive correlation with ambient signals, suggesting that the zero air signals originated from residual sulfate compounds, which may have been incompletely vaporized by each laser shot. Figure 3.9b shows the time series of $M_{\mathrm{MS}}^{\mathrm{amb}}$, $M_{\mathrm{SPA}}^{\mathrm{amb}}$, and $M_{\mathrm{filter}}^{\mathrm{amb}}$ during the measurement period. Note that the $M_{\mathrm{filter}}^{\mathrm{amb}}$ is the ambient mass concentration measured by filter analysis. The $M_{\mathrm{MS}}^{\mathrm{amb}}$ values were calculated using the data shown in Figure 8a and by interpolating the sensitivity data shown in Figure 3.7. The $M_{\mathrm{SPA}}^{\mathrm{amb}}$ values were calculated using equations (3.5) − (3.7), and calibration performed by same method of PT-LDMS. During the period of high sulfate mass concentrations (November 17–19), the PT-LDMS data tended to be lower than those obtained from SPA and filter analysis. On the other hand, the difference in the mass concentration of sulfate between the PT-LDMS and SPA/filter analysis

during the low mass concentration period (November 14 and 20) was not as large as the difference during the high-sulfate period.

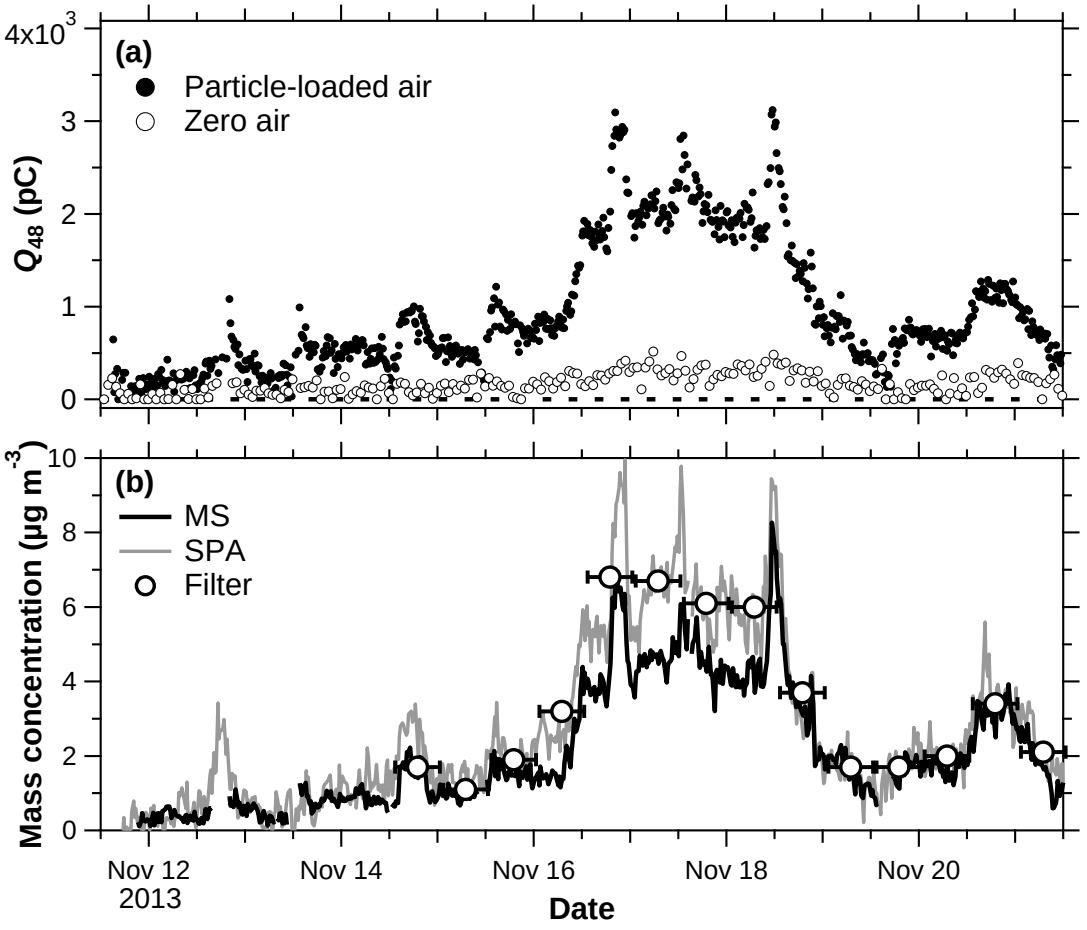

Figure 3.9. (a) Time series of $Q^{amb}_{48,\ particle}$ and $Q^{amb}_{48,\ zero}$. The filled and open circles denote the particle-loaded air signals and zero air signals, respectively. The dashed line represents the zero level. (b) Time series of M^{amb}_{MS} (solid line), M^{amb}_{SPA} (shade line), and M^{amb}_{filter} (circle marker). Error bars of M^{amb}_{filter} depict the average time of filter sampling (12 h). Missing data points of PT-LDMS (e.g. November 12) were due to calibrations.

Figure 3.10 shows the scatter plot of M_{MS}^{amb}, M_{SPA}^{amb}, and M_{filter}^{amb}, and that of M_{MS}^{amb} and M_{SPA}^{amb}. Good agreement was observed between M_{SPA}^{amb} and M_{filter}^{amb}, with a regression slope of 0.98 and an r^2 value of 0.99. Although M_{MS}^{amb} exhibited a close correlation with M_{SPA}^{amb} (r^2 = 0.96) and M_{filter}^{amb} (r^2 = 0.95), the PT-LDMS tended to underestimate the filter analysis (regression slope = 0.67) and SPA (regression slope = 0.70). It should be noted that the regression slope was largely affected by the data points in the higher mass concentration range. When focusing on the lower mass concentration range, the data points became closer to the 1:1 correspondence line.

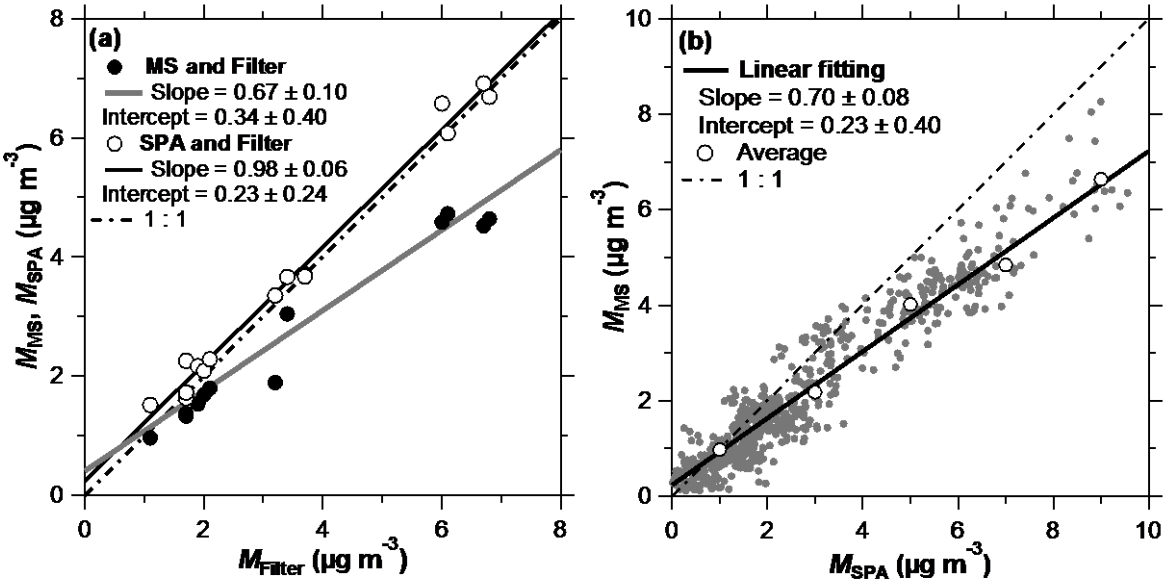

Figure 3.10. Correlation plots of (a) M_{MS}^{amb} and M_{SPA}^{amb} versus M_{filter}^{amb} analysis and (b) M_{MS}^{amb} versus M_{SPA}^{amb}. The shaded and solid lines in (a) represent the regression lines of M_{MS}^{amb} versus M_{filter}^{amb} (r^2=0.95) and M_{SPA}^{amb} versus M_{filter}^{amb} (r^2=0.99), respectively. The shaded points in (b) represent all data, while open circles represent the averages in the M_{SPA}^{amb} bin of 1 μg m^{-3}. The solid line in (b) represents the regression line for the averaged values (r^2=0.96). The dashed lines in (a) and (b) denote the 1:1 lines.

3.4. Discussion

3.4.1. Decrease in the Sensitivity for Sulfate

The observed decrease in the sulfate sensitivity during the ambient measurements is discussed. The decrease in the sulfate sensitivity was not observed during the laboratory experiments and became evident after the start of the ambient measurements (see Figure 2.6). The damage of the particle trap may have been caused by the presence of refractory compounds in ambient aerosols that efficiently absorbed the CO_2 laser. This may have resulted in local, extreme heating of the particle trap and partial detachment of the coating. Further investigation and improvement are needed to increase the durability of the trap.

3.4.2. Limit of Detection

The limit of detection (LOD) for sulfate aerosols by the PT-LDMS is now evaluated. The LOD can be estimated as the equivalent concentration at which the difference in the peak height of ion currents between particle-loaded and zero air is twice the standard deviation (2σ) of the background level. The LOD value estimated by this method was 0.07 μg m^{-3}, on average. Alternatively, the upper limit of LOD can be estimated by calculating the variability in the mass concentration in ambient air at sufficiently low mass concentrations (November 12–13 in Figure 2.8). The average and standard deviation of the mass concentration during this period were 0.5 and 0.04 μg m^{-3}, respectively, which yields an upper limit of LOD of 0.08 μg m^{-3}.

3.4.3. Possible Uncertainties

PT-LDMS

Possible systematic uncertainties in the determination of sulfate mass concentrations by the PT-LDMS are discussed based on theoretical expressions. For simplicity, we assume that $Q^{X}_{m/z,\,\mathrm{zero}}$

was proportional to $Q^{X}_{m/z,\,\mathrm{particle}}$. $\Delta Q^{X}_{m/z}$ can be theoretically expressed as follows:

$$\Delta Q^{X}_{m/z} = A \quad Tr^{X}\, CE^{X}\, Y^{X}\, (1 - \alpha^{X})\, IE^{X}\, fr^{X}_{m/z}\, M^{X}_{\mathrm{true}}\, V, \tag{3.8}$$

where A is a constant for the conversion from mass to ion signals, Tr^{X} is the transmission efficiency of the aerodynamic lens, CE^{X} is the collection efficiency of particles, Y^{X} is the vaporization efficiency of particle compounds, α^{X} is the adsorption efficiency of SO_2 on the cell, IE^{X} is the ionization efficiency of the evolved gas, and $fr^{X}_{m/z}$ is the fragment ratio at *m/z*. M^{X}_{true} is the "true" mass concentration of sulfate aerosols, which is unknown in principle. Note that each parameter in equation (3.8) is not explicitly determined by calibration.

Based on equations (3.1) – (3.4) and (3.8), the relative error in the mass concentration of sulfate aerosols can be expressed as follows:

$$\frac{M^{\mathrm{amb}}_{\mathrm{MS}}}{M^{\mathrm{amb}}_{\mathrm{true}}} = \frac{Tr^{\mathrm{amb}}}{Tr^{\mathrm{cal}}}\,\frac{CE^{\mathrm{amb}}}{CE^{\mathrm{cal}}}\,\frac{Y^{\mathrm{amb}}}{Y^{\mathrm{cal}}}\,\frac{1 - \alpha^{\mathrm{amb}}}{1 - \alpha^{\mathrm{cal}}}\,\frac{IE^{\mathrm{amb}}\, fr^{\mathrm{amb}}_{48}}{IE^{\mathrm{cal}}\, fr^{\mathrm{cal}}_{48}}\,\frac{M^{\mathrm{cal}}_{\mathrm{CPC}}}{M^{\mathrm{cal}}_{\mathrm{true}}}. \tag{3.9}$$

The uncertainty in the mass concentration of sulfate determined by the PT-LDMS depends on the difference in the following factors between ambient and calibration particles: transmission efficiency of the aerodynamic lens ($Tr^{\mathrm{amb}}/Tr^{\mathrm{cal}}$), particle collection efficiency ($CE^{\mathrm{amb}}/CE^{\mathrm{cal}}$), vaporization efficiency of particles ($Y^{\mathrm{amb}}/Y^{\mathrm{cal}}$), adsorption efficiency of the evolved gas ($(1 - \alpha^{\mathrm{amb}})/(1 - \alpha^{\mathrm{cal}})$), and ionization efficiency and fragmentation of evolved gas ($IE^{\mathrm{amb}}/IE^{\mathrm{cal}}$ and $fr^{\mathrm{amb}}/fr^{\mathrm{cal}}$, respectively). The uncertainty also depends on the accuracy of the DMA sizing, CPC counting, and multiple charge correction, which can be cancelled out when taking into account the comparison between the PT-LDMS and SPA. It is noted that these factors are also important for quantification using an Aerodyne AMS.

Table 3.2 summarizes the estimates of systematic errors. The size cut of the PT-LDMS was approximated as PM_1 and limited by the transmission efficiency of the aerodynamic lens, which

is essentially the same as those used in the Aerodyne AMS [e.g., *Liu et al.* 1995; *Takegawa et al.* 2009; *Miyakawa et al.* 2014]. The transmission efficiency for particles with d_m = 250 nm can be regarded as unity, but the transmission efficiency for multiply charged particles included in the DMA exit (d_m = 412, 569 nm) may be less than unity. The overall Tr^{cal} was estimated to be ~0.97 using the transmission efficiency curve given by *Miyakawa et al.* [2014]. The overall Tr^{amb} was estimated to be ~0.85 assuming a typical size distribution of aerosol particles in Tokyo (see appendix). This yields an estimate of ~0.88 for Tr^{amb}/Tr^{cal} in this case of $PM_{2.5}$ ambient particles. Note that Tr^{amb} and Tr^{cal} values are strongly dependent on the accuracy of the transmission efficiency of the aerodynamic lens and the assumption of the size distribution in ambient air.

The collection efficiency of ambient aerosol particles is also difficult to quantify because it depends on the size distribution and physical properties of aerosol particles. As compared to liquid particles, solid particles such as dry $(NH_4)_2SO_4$ particles generated in the laboratory tend to exhibit a broader distribution on the particle trap [*Takegawa et al.* 2012]. Polydisperse, irregularly shaped particles such as soot aggregate particles may also exhibit a broader distribution than monodisperse, spherical particles because of the characteristics of the aerodynamic lens [*Zhang et al.* 2004; *Huffman et al.* 2005; *Salcedo et al.* 2007]. The degree of overlap between the laser and particle beams can affect the temporal evolution of ion signals [*Takegawa et al.* 2012]. A possible approach for estimating the uncertainty is to compare the temporal evolution of ion signals at *m/z* 48 between ambient and calibration conditions, as shown in Figure 3.11. The evolution profiles were found to be similar, suggesting that the distributions of collected particles did not significantly vary between ambient and calibration conditions and that CE^{amb}/CE^{cal} can be assumed to be close to unity. This assumption does not mean that both CE^{amb} and CE^{cal} were unity but that they were comparable during the measurement period.

Table 3.2. Possible error of each instrument

Instruments	Factor		Relative error
PT-LDMS	Size cut[a]	Ambient	−0.15
		Calibration	+0.03
	Vaporization[b]	Ambient	−0.13
		Calibration	+0.03
	Contribution of refractory compounds[c]		−0.06
Calibration[d]	DMA sizing		±0.01
	CPC detection efficiency		−0.05
	Correction for multiply charged particles		±0.04

[a] The size cut error was estimated assuming a typical size distribution of the aerosols in Tokyo (unpublished data, see supplementary material).

[b] The vaporization error was estimated based on the temporal variation of $Q^{X}_{48,\,zero}$ (see text for details).

[c] The refractory compound error was estimated using Na^+, Cl^-, and K^+ from filter analysis and previous studies [*Takegawa et al.* 2005; *Schwab et al.* 2006]. This error represents refractory sulfate compounds that are detectable by the SPA but not by the PT-LDMS (Na_2SO_4, K_2SO_4).

[d] The calibration error can be cancelled out when taking into account the comparison between the PT-LDMS and SPA.

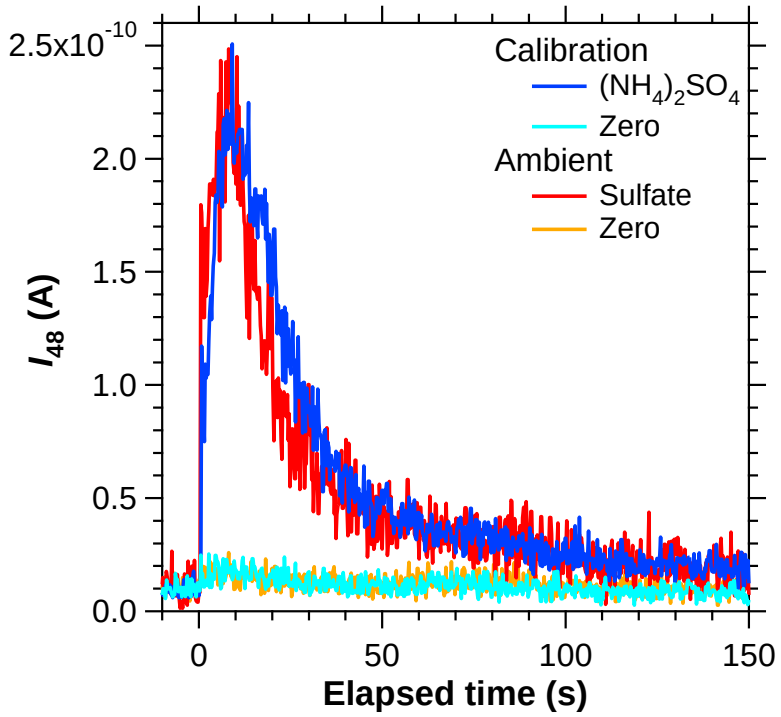

Figure 3.11. The evolution of mass normalized *m/z* 48 ion current for calibration (blue and turquoise lines) and ambient (red and orange lines) conditions. The accumulated mass of sulfate was 10.2 and 5.8 ng for calibration and ambient conditions, respectively. The ion current for ambient condition was scaled up by a factor of 1.76 (= 10.2/5.8) to clarify the comparison of two signals.

The Y^{amb}/Y^{cal} ratio is affected by two factors: incomplete vaporization of $(NH_4)_2SO_4$ particles and contribution of refractory sulfate compounds, which were unlikely vaporized with their vaporization temperature exceeding T_{trap} (sodium sulfate (Na_2SO_4) and potassium sulfate (K_2SO_4)). The ratio of zero air to particle-loaded air signals was ~0.13 for ambient particles and ~0.03 for calibration particles. As a result, Y^{amb}/Y^{cal} originating from incomplete vaporization of $(NH_4)_2SO_4$ was estimated to be ~0.90.

Good agreement was observed for $\Delta Q^X_{64}/\Delta Q^X_{48}$ between ambient and calibration particles, suggesting that the major component of evolved gas in the case of ambient particles was very

similar to calibration particles (Figure 2.5 and 2.7). Hence, we can assume that IE^{amb}/IE^{cal}, $fr_{48}^{amb}/fr_{48}^{cal}$, and $(1-\alpha^{amb})/(1-\alpha^{cal})$ were close to unity.

The positive or negative signs of the systematic errors in Table 3.2 represent that the mass concentration of sulfate in ambient air can be overestimated or underestimated, respectively. The errors for ambient and calibration conditions were partially cancelled out because of the similarities in the chemical form and size of sulfate aerosol particles between ambient and calibration conditions. Conversely, it is suggested that the choice of material and size of calibration particles is important for reducing the measurement uncertainties.

SPA

Possible systematic uncertainties in the determination of sulfate mass concentrations by the SPA are discussed. As mentioned in section 3.2.5, χ_{zero}^{amb} was measured using a HEPA filter and χ_{zero}^{cal} was measured by turning off the DMA voltage. The $\chi_{particle}^{X}$ is expressed as follows:

$$\chi_{particle}^{X} = B\,\varepsilon^{X}\,M_{true}^{X} + \chi_{gas}^{X}\ , \tag{3.10}$$

where B is a constant for the conversion from the mass concentration of sulfate to the mixing ratio of SO_2, ε^X is the conversion efficiency of sulfate to SO_2, and χ_{gas}^{X} is the mixing ratio of gas-phase SO_2 in the sample air. As for the calibration, χ_{gas}^{cal} should be equal to χ_{zero}^{cal} because there is no difference in the airflow line between particle-loaded and zero air (the zero level was measured by turning off DMA voltage). On the other hand, χ_{gas}^{amb} and χ_{zero}^{amb} may be different due to adsorption of SO_2 in the HEPA filter, considering large surface area inside the filter. It is rather difficult to estimate the χ_{zero}^{amb} value because the amount of SO_2 adsorption on the filter may not correlate with the SO_2 mixing ratio in the sample air [*Eatough et al.* 1995]. Although $\chi_{particle}^{X}$ may also have been affected by adsorption of SO_2 on other surfaces including the conversion cell and

tubing, we assumed this effect was relatively minor.

Based on equations (3.5) − (3.7), and (3.10) the mass concentration of sulfate aerosols determined by the SPA can be expressed as follows:

$$\frac{M_{\mathrm{SPA}}^{\mathrm{amb}}}{M_{\mathrm{true}}^{\mathrm{amb}}} = \frac{\varepsilon^{\mathrm{amb}}}{\varepsilon^{\mathrm{cal}}} \frac{M_{\mathrm{CPC}}^{\mathrm{cal}}}{M_{\mathrm{true}}^{\mathrm{cal}}} + \left(\chi_{\mathrm{gas}}^{\mathrm{amb}} - \chi_{\mathrm{zero}}^{\mathrm{amb}}\right) F_{\mathrm{SPA}} \frac{1}{M_{\mathrm{true}}^{\mathrm{amb}}} \quad . \tag{3.11}$$

The uncertainty in the mass concentration of sulfate determined by the SPA depends on two terms. The first term originates from the conversion of sulfate to SO_2 and depends on the conversion efficiency ($\varepsilon^{\mathrm{amb}}/\varepsilon^{\mathrm{cal}}$). The second term originates from SO_2 in the ambient air and depends on the mixing ratio of ambient SO_2.

The $\varepsilon^{\mathrm{amb}}/\varepsilon^{\mathrm{cal}}$ ratio can be affected by the contribution of refractory sulfate compounds, which were unlikely vaporized with their vaporization temperature exceeding converter tube temperature of SPA (e.g. $CaSO_4$).

As mentioned above, the uncertainty originating from gas-phase SO_2 in ambient air was difficult to estimate because $\chi_{\mathrm{gas}}^{\mathrm{amb}}$ was not determined from the measurements. If we assume an error of $\chi_{\mathrm{gas}}^{\mathrm{amb}}$ minus $\chi_{\mathrm{zero}}^{\mathrm{amb}}$ to be 1 ppbv, for example, it corresponds to an error of 4 μg m^{-3} in the mass concentration of sulfate aerosols. This uncertainty could potentially become important with increasing mixing ratios of SO_2.

3.4.4. Comparison between PT-LDMS and SPA

For the comparison between PT-LDMS and SPA, it is necessary to consider the difference in the sulfate compounds measured by these instruments. The temperature of the particle trap induced by the CO_2 laser was ~500°C, while the temperature of the converter of the SPA was set at 1000°C. Among various refractory sulfate compounds, Na_2SO_4 (dissociation temperature of 800°C) was likely to be the most relevant form of the compound, which was detectable by the SPA but not by

the PT-LDMS. *Schwab et al.* [2006] reported that the responses of SPA to Na_2SO_4 and to K_2SO_4 were ~20% and 60% respectively. Based on their study, the contributions of Na_2SO_4 and K_2SO_4 were estimated to be ~2% and ~5%, respectively. Note that the contribution of Na_2SO_4 was estimated using Na^+ and Cl^- from the filter data assuming that the Na^+ originated from both sodium chloride (NaCl) and Na_2SO_4 [*Takegawa et al.* 2005]. The contribution of K_2SO_4 was estimated assuming that all K^+ originated from K_2SO_4.

The combined uncertainty of the factors described in the previous section and the above factor were estimated to be ~20%, which may potentially explain the underestimation by the PT-LDMS to a large extent. Further studies are needed to improve the quantification of sulfate aerosol under various environments.

3.5. Summary

This study reports the quantification of sulfate aerosols by the PT-LDMS. The instrument was modified compared to the previous version described by *Takegawa et al.* [2012]. Laboratory experiments were performed to investigate the optimal conditions for ambient measurements and temperature dependence of sulfate sensitivity. The major decomposition product of $(NH_4)_2SO_4$ was similar to that of ambient sulfate in the PT-LDMS. The results also showed that the sensitivity for $(NH_4)_2SO_4$ particles tended to increase with T_{cell}, which may be explained by decreased adsorption of the decomposition product of $(NH_4)_2SO_4$ on the cell surface at high temperatures.

Ambient measurements for the overall test of the instrument, as well as the intercomparison of PT-LDMS with other measurements methods, were performed in Tokyo. $\Delta Q^X_{64}/\Delta Q^X_{48}$ for ambient aerosol particles showed good agreement with the laboratory data to within 15%, indicating that the thermal desorption products from ambient sulfate aerosol particles were very

similar to those from $(NH_4)_2SO_4$ particles generated in the laboratory. The PT-LDMS exhibited tight correlation with the SPA (r^2 = 0.96), but tended to underestimate the mass concentration of sulfate (slope = 0.70).

Major uncertainties in the PT-LDMS during the measurement period originated from the size cut of the aerodynamic lens (~12%) and the difference in vaporization efficiency of $(NH_4)_2SO_4$ particles between calibrations and ambient conditions (~10%). In addition, uncertainty in the contribution of refractory sulfur compounds between the PT-LDMS and SPA was estimated to be ~6% in this case. These uncertainties were estimated by consideration of numerous sources of systematic error and used for the interpretation of the intercomparison results. The overall uncertainty due to the above factors was estimated to be ~20%, which may potentially explain the underestimation of the PT-LDMS to a large extent. Further studies using polydisperse aerosol particles and other materials for calibrations are needed in order to improve the accuracy of quantification.

Appendix 3A: supplementary material

3A.1. Correction for multiple charging

A method for multiply charged correction is described. The method is similar to that described by *Wang et al.* [2010] and *Takegawa and Sakurai* [2011]. The aerosol flow passing through the DMA contain not only singly charged particles but also multiply charged particles. The mass concentration of calibration particles may be underestimated if we assume the particles are all singly charged. The population of muliply charged particles needs to be experimentally evaluated.

The fraction of doubly charged particles (f_2) and triply charged particles (f_3) was calculated by using the method described in *Wang et al.* [2010] and *Takegawa and Sakurai* [2011]. The mass concentration determined from the CPC data (M_{CPC}^{cal}) is expressed as follows:

$$M_{CPC}^{cal} = \frac{\pi}{6}\rho N d_1^3 \left(1 - f_2 - f_3 + f_2 \frac{d_2^3}{d_1^3} + f_3 \frac{d_2^3}{d_1^3}\right) . \quad \text{(A3.1)}$$

Where ρ is a particle density, N is the number concentration measured by the CPC, d_1 is a particle diameter selected by DMA, d_2 is the paricle diameter of doubly charged particles, and d_3 is the particle diameter of triply cherged particles.

3A.2. KNO_3

The sensitivity for nitrate was measured under various T_{trap} and T_{cell} conditions as well as sulfate. Figure 3A.1 shows the evolution of the *m/z* 30 ion currents for KNO_3 particles obtained at a T_{trap} of ~550°C and T_{cell} values of 200 and 280°C. For KNO_3 particles, the overall shape of the *m/z* 30 signal significantly changed in the earlier time period with increasing T_{cell}. The artifact signals were found be more pronounced for KNO_3 than for $(NH_4)_2SO_4$ particles.

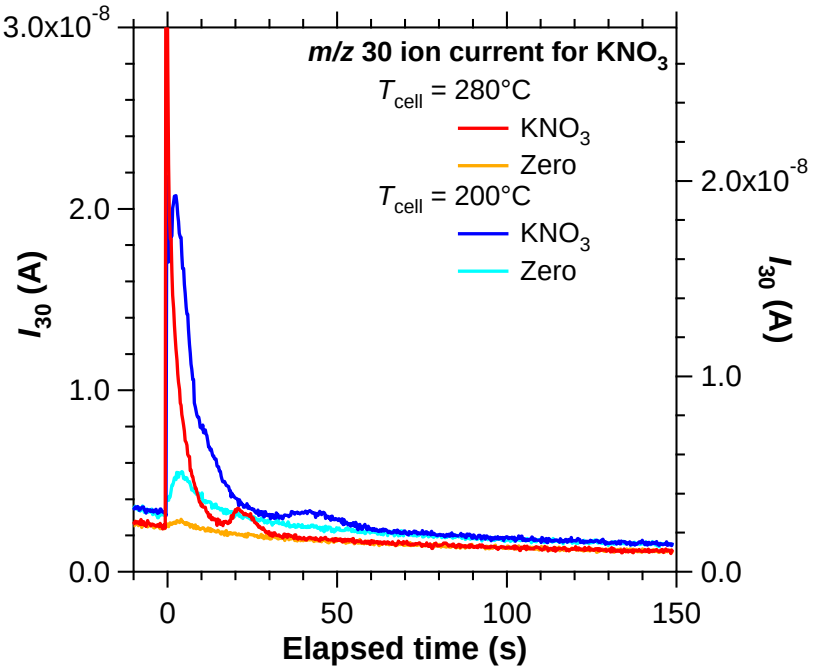

Figure 3A.1 The evaluation of mass normalized *m/z* 30 ion current for KNO_3 particles obtained at a T_{trap} of ~550°C and T_{cell} values of 200°C (blue and light blue lines, right axis) and 280°C (red and orange lines, left axis).

Figure 3A.2 shows the sensitivity experiment for KNO_3. Although substantial scatter was observed in the data, the dependence of the sensitivity on T_{cell} also appeared to be more significant than the dependence on T_{trap} for KNO_3. Higher T_{cell} conditions exhibited lower sensitivity for KNO_3 particles.Changes in the temporal evolution of ion current and sensitivity depending on T_{cell} were somewhat unexpected results. These features may not be explained by adsorption of NO on the cell wall. Further experiments are needed to investigate the mechanism.

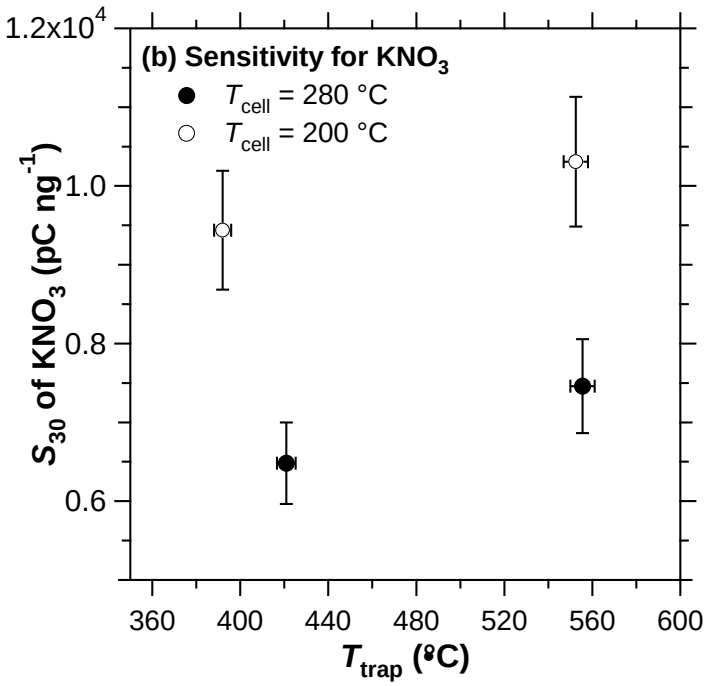

Figure 3A.2. Dependence of nitrate sensitivity versus T_{trap} at various T_{cell} values. The error bars represent uncertainty originating from random error (2σ) of PT-LDMS (4%), CPC (2%), and radiation thermometer (1%).

2A.3 Effect of the Difference in Size Cut

The effects of the difference in the size cut between the PT-LDMS (approximately PM_1) and SPA ($PM_{2.5}$) are described. Figure 3A.3 shows an expample of volume size distribution in urban air (quoted from *Seinfeld and Pandis* [2006]), and that measured in Tokyoin the spring of 2013 by a scanning mobility particle sizer (SMPS) and optical particle counter (OPC; unpublished data), together with the transimission efficiencies of the aerodynamic lens [*Miyakawa et al.* 2015] and the $PM_{2.5}$ cyclone. We asumed that the ambient particle density was 1.5 g cm^{-3} for calculating the vacuum aerodynamic diameters. As a result, the uncertainty of size cut was estimated to be −0.15 for ambient particles.

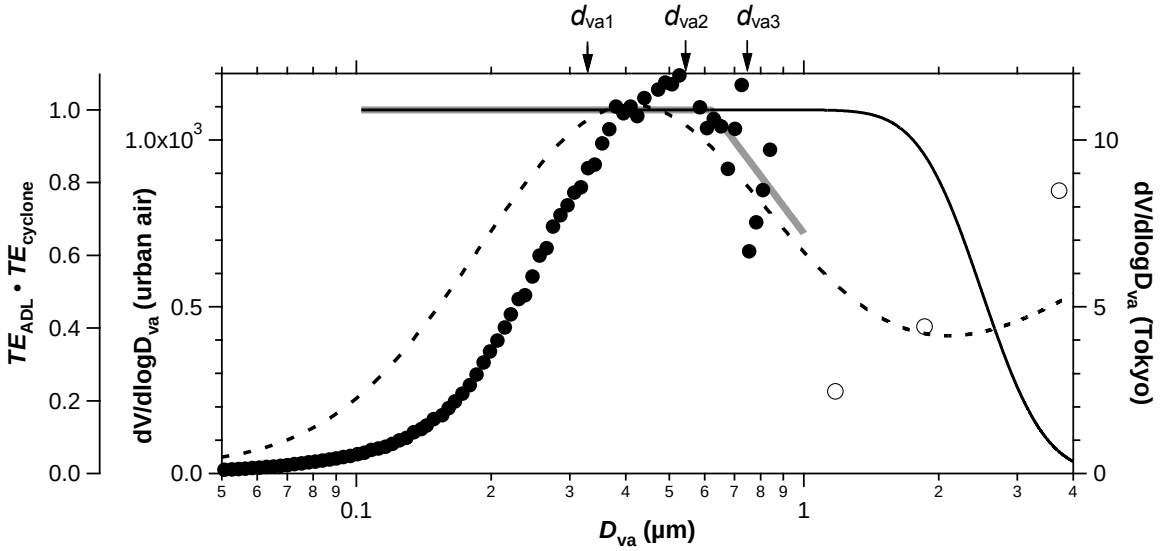

Figure 3A.3. An example of volume size distribution in urban air quoted from Seinfeld and Pandis (2006) (dashed line) and that measured in Tokyo in the spring of 2013 (filed and open circles), transmission efficiency of the aerodynamic lens (TE_{ADL}, shaded line), and that of the $PM_{2.5}$ cyclone ($TE_{cyclone}$, solid line). The vacuum aerodynamic diameters were calculated based on the assumption that the ambient particle density was 1.5 g cm^{-3}. The curve of $TE_{cyclone}$ was drawn based on the datasheet of URG-2000-30EH. The arrows indicate the vacuum aerodynamic diameters of calibration $(NH_4)_2SO_4$ particles.

References

Alfarra, M. R., (2004). Insights into Atmospheric Organic Aerosols Using an Aerosol Mass Spectrometer. University of Manchester Institute of Science and Technology, PhD Thesis.

Allan, D. A., Jimenez, J. L., Williams, P.I., Alfarra, M. R., Brower, K. N., Jayne, J.T., Coe, H., and Worsnop, D. R. (2003), Quantitative Sampling Using an Aerodyne Aerosol Mass Spectrometer 1. Techniques of Data Interpretation and Error Analysis. *J. Geophys. Res.* 108(D3):4090.

Altshuller, A. P. (1973). Atmospheric Sulfur Dioxide and Sulfate Distribution of Concentration at

Urban and Nonurban Site in United States. *Environ. Sci. Tech.* 7: 8.

Drewnick, F., Schwab, J. J., Hogrefe, O., Peters, S., Husain, L., Diamond, D., Weber, R., and Demerjian, K. L. (2003). Intercomparison and Evaluation of Four Semi-continuous $PM_{2.5}$ Sulfate instruments. *Atmos. Environ.* 37: 3335-3350.

Eatough, D., Lewis, L. J., Eatough, M., and Lewis, E. (1995). Sampling Artifacts in the Determination of Particulate Sulfate and SO_2 (g) in the Desert Southwest Using Filter Pack Samples. *Environ. Sci. Technol.* 29, 787-791.

Hogrefe O., Schwab J. J., Drewnick F., Lala G. G., Peters S., Demerjian K. L., Rhoads K., Felton H. D., Rattigan O. V., Husain L., Dutkiewicz V. A. (2004). Semicontinuous PM2.5 sulfate and nitrate measurements at an urban and a rural location in NewYork: PMTACS-NY summer 2001 and 2002 campaigns. *J. Air. Waste. Manage. Assoc.* 54:1040-1060.

Huffman, J. A., Jayne, J. T., Drewnick, F., Aiken, A. C., Onasch,T., Worsnop, D. R., and Jimenez, J. L. (2005). Design, Modeling, Optimization, and Experimental Tests of a Particle Beam Width Probe for the Aerodyne Aerosol Mass Spectrometer, *Aerosol Sci. Technol.* 39, 1143-1163.

Jayne, J. T., Leard, D. C., Zhang, X. F., Davidovits, P., Smith, K. A., Kolb, C. E., and Worsnop, D. R. (2000). Development of an Aerosol Mass Spectrometer for Size and Composition Analysis of Submicron Particles. *Aerosol Sci. Technol.* 33(1-2): 49-70.

Khlystov, A., Wyers, G. P., and Slanina, J. (1995). The Steam-Jet Aerosol Collector, Atmos. Environ. 29: 2229-2234.

Kiyoura, R., and Urano, K. (1970). Mechanism, Kinetics, and Equilibrium of Thermal Decomposition of Ammonium Sulfate. *Ind. Eng. Chem. Process Des. Dev.* 9(4), 489-494.

Liu, P., Ziemann, P. J., Kittelson, D. B., and McMurry, P. H. (1995). Generating Particle Beams of

Controlled Dimensions and Divergence: I. Theory of Particle Motion in Aerodynamic Lenses and Nozzle Expansions. *Aerosol Sci. Technol*. 22:293-313.

Miyakawa, T., Takeda, N., Koizumi, K., Tabaru, M., Ozawa, Y., Hirayama, N., and Takegawa, N. (2014). A New Laser Incandescence-Mass Spectrometric Analyzer (LII-MS) for Online Measurement of Aerosol Composition Classified by Black Carbon Mixing State, *Aerosol, Sci. Thecnol.* 48: 853-863.

Miyakawa, T., Kanaya, Y., Taketani, F., Tabaru, M., Sugimoto, N., Ozawa, Y., and Takegawa, N. (2015). Ground-based Measurement of fluorescent aerosol particles in Tokyo in the spring of 2013: Potential Impacts of Non-biological Materials on Autofluorescence measurements of airborne particles. *J. Geophys. Res.* DOI: 10.1002/2014JD022189.

Pilinis, C., and Seinfeld, J. H. (1987). Continued Development of a General Equilibrium Model for Inorganic Multicomponent Atmospheric Aerosols. *Atmos. Environ.* 21, 2453-2466.

Salcedo, D., Onasch, T. B., Canagaratna, M. R., Dzepina, K., Huffman, J. A., Jayne, J. T., Worsnop, D. R., Kolb, C. E., Weimer, S., Drewnick, F., Allan, J. D., Delia, A. E., and Jimenz, J. L. (2007). Technical Note: Use of a beam width probe in an Aerosol Mass Spectrometer to monitor particle collection efficiency in the field. *Atmos. Chem. Phys.* 7, 549-556

Saltzman, E. S., Brass, G. W., and Price, D. A. (1983). The Mechanism of Sulfate Aerosol Formation: Chemical and Sulfur Isotopic Evidence. *Geophys. Res. Lett.* 10:N7, 513-516.

Schwab, J. J., Felton, H. D., and Demerjian, K. L. (2004). Aerosol Chemical Composition in New York State from Integrated filter Samples: Urban/rural and Seasonal Contrasts. *J. Geophys. Res.* 109:D16S05

Schwab, J. J., Hogrefe, O., Demerjian, K. L., Dutkiewicz, V. A., Husain, L., Rattigan, O. V., and Felton, H. D. (2006). Field and Laboratory Evaluation of the Thermo Electron 5020 Sulfate

Particle Analyzer. *Aerosol Sci. Technol.* 40: 744-752

Seinfeld, J.H., and Pandis, S.N. (2006). Atmospheric Chemistry and Physics, 2nd ed., John Wiley &Sons, New York.

Takegawa, N., Miyazaki, Y., Kondo, Y., Komazaki, Y., Miyakawa, T., Jimenez, J. L., Jayne, J. T., Worsnop, D. R., Allan, J. D., and Weber, R. J. (2005). Characterization of an Aerodyne Aerosol Mass Spectrometer (AMS): Intercomparison with Other Aerosol Instruments. *Aerosol Sci. Technol.* 39: 760-770.

Takegawa, N., Miyakawa, T., Watanabe, M., Kondo, Y., Miyazaki, Y., Han, S., Zhao, Y., van Pinxteren, D., Bruggemann, E., Gnauk, T., Herrmann, H., Xiao, R., Deng, Z., Hu, M., Zhu, T., and Zhang, Y. (2009). Performance of an Aerodyne Aerosol Mass Spectrometer (AMS) during Intensive Campaigns in China in the Summer of 2006. *Aerosol Sci. Technol.* 43:189-204.

Takegawa, N., and Sakurai, H. (2011). Laboratory Evaluation of a TSI Condensation Particle Counter (Model 3771) Under Airborne Measurement Conditions. *Aerosol Sci. Technol.* 45: 272-283

Takegawa, N., Miyakawa, T., Nakamura, T., Sameshima, Y., Takei, M., Kondo, Y., and Hirayama, N. (2012). Evaluation of a New Particle Trap in a Laser Desorption Mass Spectrometer for Online Measurement of Aerosol Composition. *Aerosol Sci. Technol.* 46: 428-443.

Voisin, D., Smith, J. N., Sakurai, H., McMurry, P. H., and Eisele, F. L. (2003). Thermal Desorption Chemical Ionization Mass Spectrometer for Ultrafine Particle Chemical Composition. *Aerosol Sci. Technol.* 37: 417-475.

Wang, X., Caldow, R., Sem, G. J., Hama, N., and Sakurai, H. (2010). Evaluation of a Condensation Particle Counter for Vehicle Emission Measurement: Experimental Procedure and Effects of

Calibration Aerosol Material. *J. Aerosol Sci.* 41:306-318.

Weber, R. J., Orsini, D., Daun, Y. Lee, Y.-N., Klotz, P. J., and Brechtel, F. (2001). A Particle-into-Liquid Collector for Rapid Measurement of Aerosol Bulk Chemical Composition, *Aerosol Sci. Technol.* 35: 718-727.

Zhang, Q., Canagaratna, R., Jayne, J. T., Worsnop, R., and Jimenez, J. L. (2005). Time- and Size-resolved Chemical Composition of Submicron Particles in Pittsburgh: Implications for Aerosol Sources and Processes. *J. Geophys. Res.* 110: D07S09.

Zhang, Q., Jimenez, J. L., Canagaratna, M. R., Allan, J. D., Coe, H., Ulbrich, I., Alfarra, M. R., Takami, A., Middlebrook, A. M., Sun, Y. L., Dzepina, K., Dunlea, E., Docherty, K., DeCarlo, P. F., Salcedo, D., Onasch, T., Jayne, J. T., Miyoshi, T., Shimono, A., Hatakeyama, S., Takegawa, N., Kondo, Y., Schneider, J., Drewnick, F., Borrmann,S., Weimer, S., Demerjian, K., Williams, P., Bower, K., Bahreini, R., Cottrell, L., Griffin, R. J., Rautiainen, J., Sun, J. Y., Zhang, Y. M., and Worsnop, D. R. (2007). Ubiquity and Dominance of Oxygenated Species in Organic Aerosols in Anthropogenic ally-Influenced Northern Hemisphere Midlatitudes. *Geophys. Res. Lett.* 31:L13801

Zhang, X., Smith, K. A., Worsnop, D. R., Jimenz, J. L., Jayne, J. T., Kolb, C. E., Morris, J., and Davidovits, P. (2004). Numerical Characterization of Particle Beam Collimation: Part II Integrated Aerodynamic-Lens-Nozzle System. *Aerosol Sci. Technol.* 38: 619-638.

4. Laser induced incandescence – mass spectrometry (LII-MS)

4.1. Introduction

Investigating the mixing states of BC is important for estimating the climate impact of aerosol particles. Electron microscopy, LII, and a method combining a mass spectrometer and LII have been used as measurement methods for the mixing states of BC. However, LII cannot quantify the chemical composition of aerosols mixed with BC particles. It is effective to combine the LII with a mass spectrometry technique to measure the chemical composition of aerosols mixed with BC in situ.

SP-AMS is one of the most important instruments recently developed for the on-line measurement of the chemical composition of aerosols mixed with BC. A soot particle-aerosol mass spectrometer (SP-AMS) [*Onasch et al.* 2012] is constructed by placing the solid-state laser cavity used in the LII inside the chamber of an aerosol mass spectrometer (AMS). In AMS, particles introduced into the vacuum chamber are volatilized with a heated tungsten vaporizer (~600 °C) and the chemical composition of aerosols is quantified as vaporized gases with a mass spectrometer. In SP-AMS, the point of intersection between the particle beam axis and the laser axis installed inside the chamber is set just before the vaporizer. SP-AMS can directly measure the chemical composition of BC-containing particles and all particles by switching the laser. However, it has been pointed out that there are several important issues regarding such quantifications, including uncertainty due to the overlap of the laser and particle beams. Evaluations of the quantifications obtained via SP-AMS are underway. An instrument that can quantitatively measure the chemical composition of aerosols mixed with BC is needed to investigate the mixing state of

ambient BC.

The LII-MS analyzer has been developed for quantifying the chemical composition of aerosol classified by the mixing state of BC. The LII-MS analyzer consists of an LII analyzer, which selectively detects and vaporizes BC-containing particles, and a particle trap-laser desorption mass spectrometer (PT-LDMS) [*Takegawa et al.* 2012], which analyzes the chemical composition of the aerosol particles transported from the LII analyzer. The principle of operation and details of the LII-MS have been described in a previous publication [*Miyakawa et al.* 2014]. Some modifications and their performance are described in this Chapter.

4.2. Configuration of the LII-MS

Figure 4.1 shows a schematic diagram of the LII-MS analyzer. The LII-MS analyzer is an instrument in which an LII analyzer and a PT-LDMS are connected in series. In the mode in which the two analysis sections are in parallel (parallel mode), the number concentration and the mass concentration of the chemical components of aerosols are independently measured by the LII analyzer and the PT-LDMS, respectively. On the other hand, in the mode in which the two analysis sections are connected in series (tandem mode), the mass concentration of the chemical components of aerosols classified with mixing state of BC is measured. In the LII section, because BC particles are heated to the boiling point of BC (~4000 K), the chemical components mixed with BC particles are vaporized in the LII chamber. Therefore, by switching the LII laser on and off, it is possible to measure the chemical components according to the mixing state of BC in the PT-LDMS. The chemical composition of the total aerosol particles (all particles) can be analyzed in the PT-LDMS by turning off the laser (MS mode), and that of the aerosol particles externally mixed with BC (BC-free particles) can be analyzed by turning on the laser (LII-MS mode). The

difference between the signal captured for all particles and that of BC-free particles corresponds to aerosol particles internally mixed with BC (BC-containing particles).

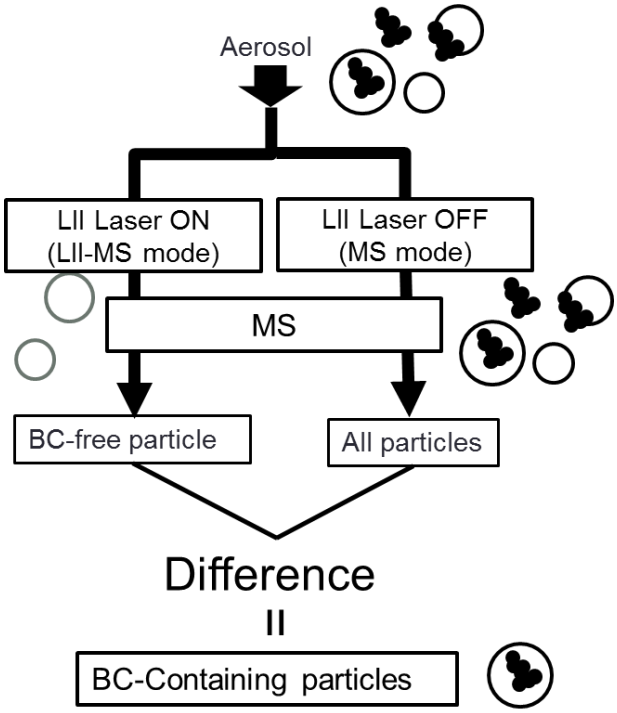

Figure 4.1. Schematic diagram of the LII-MS system which graphically describes how aerosol particles are analyzed by the PT-LDMS.

Figure 4.2 shows a schematic diagram of LII analyzer. A collection tube is used to recover the aerosol sample flow with only small changes in aerosol concentration. The collection probe consists of two coaxial tubes; the center tube is used to isolate and collect the aerosol flow separately from the sheath flow. The sample flow rate is limited by the critical orifice of the PT-LDMS (approximately 0.11 LPM). The remaining sheath flow is drawn through the space between the center and the outer tubes, which is referred as the excess flow.

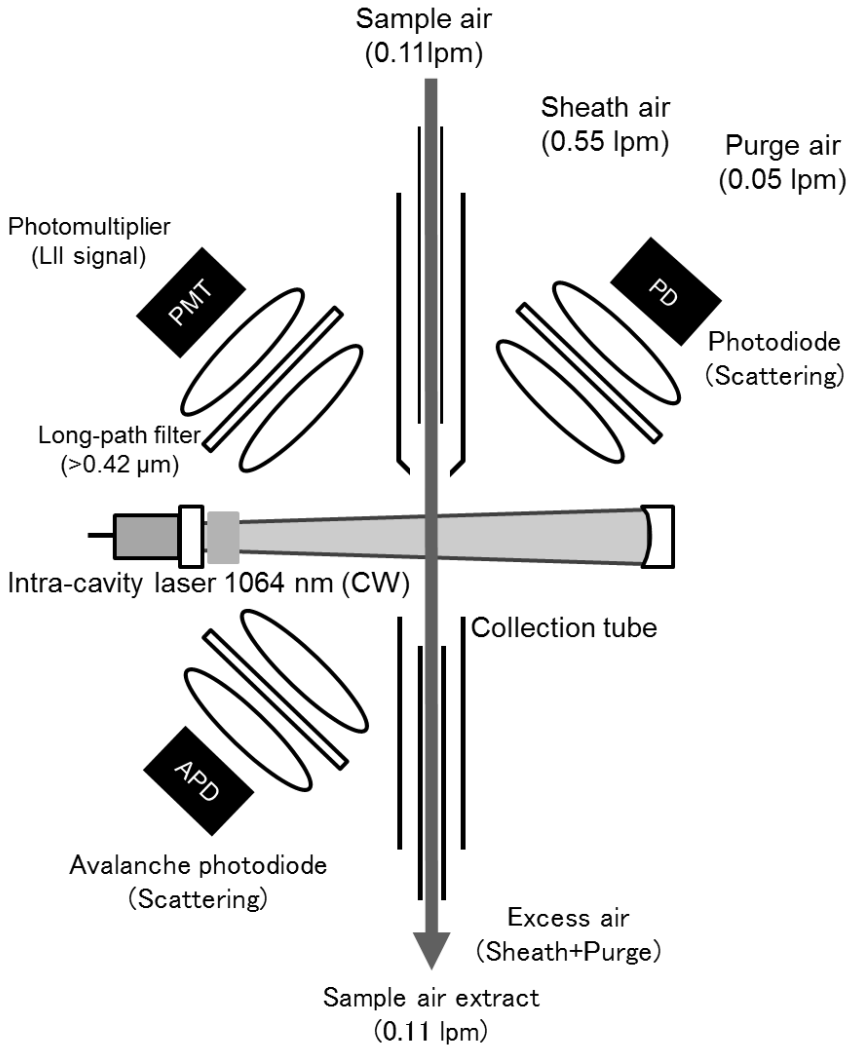

Figure 4.2. Schematic diagram of the LII analyzer. Arrows depict sample and air flows.

The PT-LDMS was developed for the online quantification of the mass concentration of sulfate, nitrate, and organics. [*Takegawa et al.* 2012; *Ozawa et al.* 2016]. A detailed design is described in *Takegawa et al.* [2012]. Here, the configuration of the PT-LDMS is summarized. The PT-LDMS consists of an inlet, a particle trap enclosed by a gold-coated cell, and a quadrupole mass spectrometer with electron impact ionization. The inlet consists of a critical orifice, an aerodynamic lens, and a skimmer cone. The flow rate is controlled and set to 0.1 LPM by the critical orifice. Particles in the sample air are converged into a narrow beam by the aerodynamic lens and are separated from the gas by the skimmer cone in the vacuum chamber. The particles are then collected in the particle trap. The particle trap consists of five stages of silicon mesh layers and a plate at the bottom coated with platinum and tungsten. The particles collide with the wall surface in the mesh layer several times and are trapped on the particle trap after losing their momentum. The particles trapped on the particle trap are vaporized by heating the trap (to ~500 °C) using a CO_2 laser with a power output of 10 W. This vaporization process includes evaporation, sublimation, decomposition, and reactions. The gas vaporized by the thermal decomposition of the particles becomes ionized via electron impacts and is detected by a quadrupole mass spectrometer (QMS). A mass concentration is calculated by comparing the ion signal obtained in ambient measurements with the calibration curve obtained in laboratory experiments.

4.3. Modification of LII-MS

In this section, I focus on important modifications to the LII-MS systems used in previous studies. Figure 4.3 shows the overview of LII-MS. The LII analyzer used in this work is the same as that used by *Miyakawa et al.* [2014]. The on/off cycle of the LII laser was changed for more

quantitative measurements of the mixing states of BC. The measurement cycle used in this study was changed from that used by *Miyakawa et al.* [2014]. The number of lasers on cycles was decreased and the time interval between two off cycles was shortened. This modification makes it possible to respond to rapid changes in mass concentration within a measurement cycle. The flow balance of the sheath-air inlet of the LII analyzer was changed for more stable measurements. The flow rate of sheath air was increased by 0.05 LPM to make the sample aerosol jet narrower. The mass concentrations of PM_1 aerosol samples passing through the LII analyzer are quantified by the PT-LDMS. The PT-LDMS quantifies the chemical composition of aerosol particles collected on the particle traps via thermal decomposition using an infrared laser. The PT-LDMS used is the same as that described by *Ozawa et al.* [2016]. The structure holding the particle traps was improved and the traps were placed closer for obtaining a high thermal conductivity. This modification improved the efficiency of trap cooling using circulating water, and the PT-LDMS could measure semi-volatile particles, such as ammonium nitrate (NH_4NO_4). The performance of PT-LDMS has been described in *Ozawa et al.* [2016].

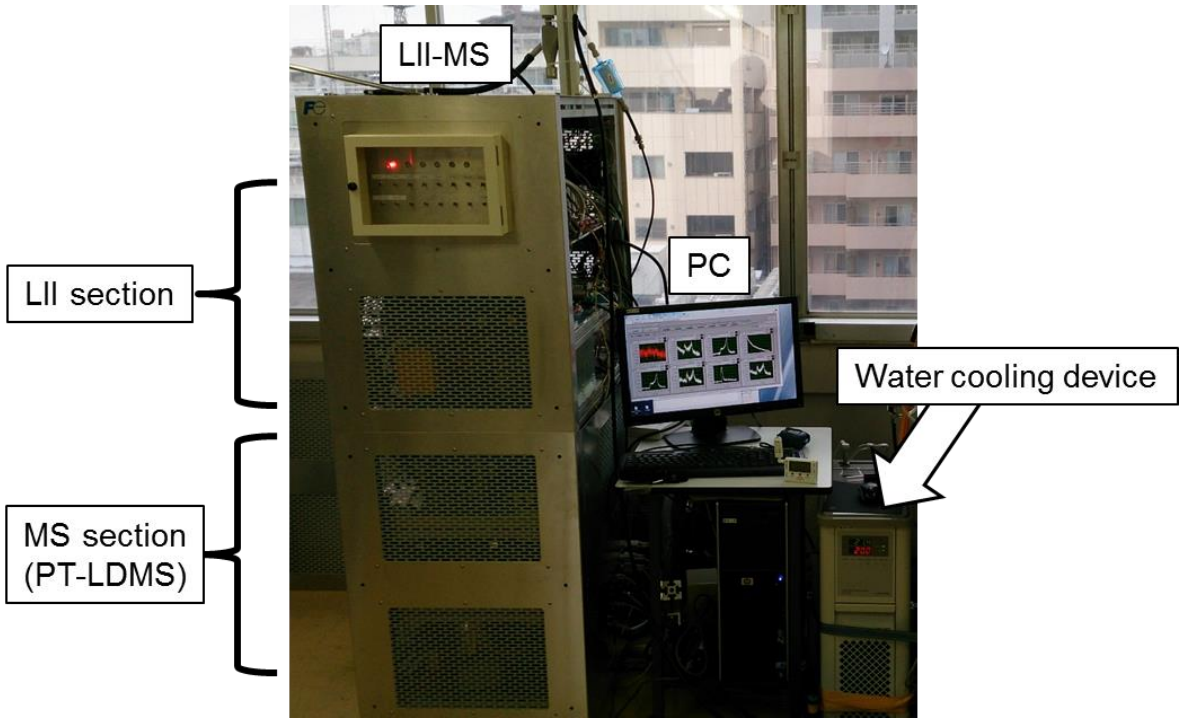

Figure 4.3. Laser induced incandescence-mass spectrometric analyzer (LII-MS).

4.4. Data processing

Ion signals at *m/z* 14 (N^+), 16 (O^+), 28 (CO^+), 30 (NO^+), 44 (CO_2^+), 48 (SO^+), 55 ($C_4H_7^+$), and 64 (SO_2^+) were monitored in laboratory experiments and in ambient measurements. The integrated values of the ion signals above the background level at each *m/z* ($Q_{m/z}$) indicate the mass of the introduced species. The values of Q_{30}, Q_{48}, and Q_{28} were selected as signals for nitrate, sulfate, and organic carbon (OC), respectively. The difference between the $Q_{m/z}$ values with and without particles (sample air and the zero-filtered air, $\Delta Q_{m/z}$) was used as a net signal originating from the particles. The details of the calculations of mass concentration are described in Chapter 3.

Ammonium sulfate ($(NH_4)_2SO_4$), potassium nitrate (KNO_3), ammonium nitrate (NH_4NO_3), oxalic acid (C2di), and azelaic acid (C9di) particles were used in the laboratory experiments. Laboratory experiments were performed in LII-MS mode to include the transmission efficiency of the tandem nozzle. The typical calibration curves obtained via laboratory experiments during

ambient measurements described in Chapter 5 are shown in Figure 4.4. The masses of nitrate (NO_3^-) and sulfate (SO_4^{2-}) introduced into the LII-MS showed good correlation with the signals of Q_{30} and Q_{48}, respectively. Using these calibration curves, the mass concentrations of nitrate (NO_3^-) and sulfate (SO_4^{2-}) in the ambient measurements were calculated.

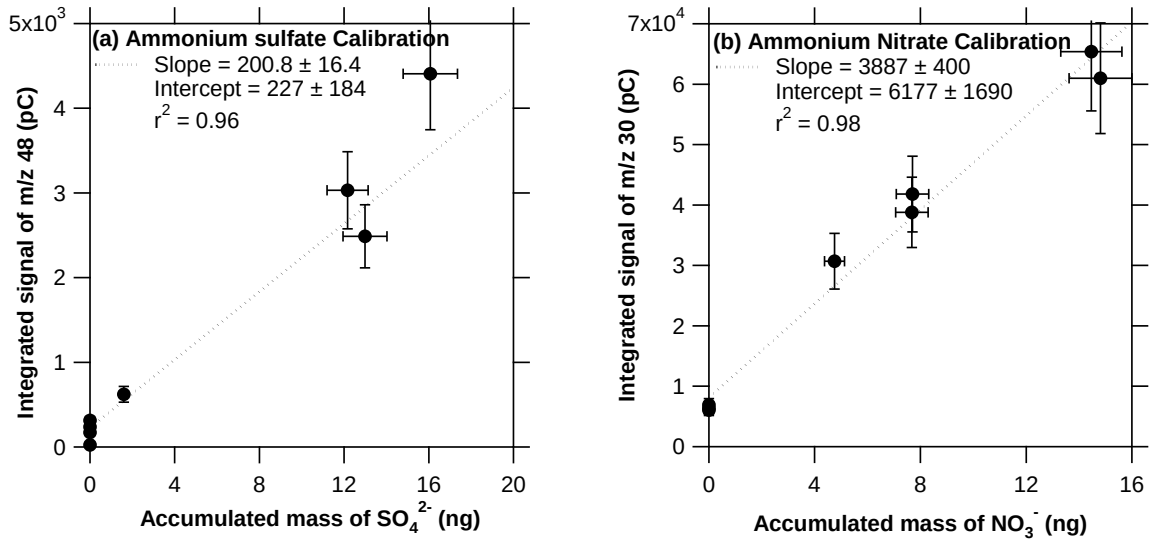

Figure 4.4. Calibration curves of (a) SO_4^{2-} and ΔQ_{48}, and (b) NO_3^- and ΔQ_{30} by laboratory experiments during an ambient measurements period.

4.5. Transmission efficiency of the LII-MS system

Figures 4.4a–4.4c show the throughput efficiency of the LII chamber (TE_{LII}), the transmission, collection, and vaporization efficiencies of the PT-LDMS ($TE_{MS} \cdot Eff_{MS}$), and the estimated transmission efficiency of the LII-MS system ($TE_{LII} \cdot TE_{MS} \cdot Eff_{MS}$), as indicated by *Miyakawa et al.* [2014]. Figure 4.5a shows the TE_{LII} of polystyrene latex (PSL) particles. More than 60% of the particles in accumulation mode are transported into the PT-LDMS. The TE_{LII} of large particles (larger than 0.8 μm in diameter) tends to increase because of their greater inertia compared with small particles. Figure 4.5b shows the $TE_{LII} \cdot TE_{MS} \cdot Eff_{MS}$ of KNO_3 and $(NH_4)_2SO_4$ particles. Because the $TE_{MS} \cdot Eff_{MS}$ at a diameter of 1 μm is ~0.6, the upper size cut of the PT-LDMS can be approximated as PM_1. Considering the combination of TE_{LII} and $TE_{MS} \cdot Eff_{MS}$, it is suggested that the LII-MS can collect and analyze 60% or more of particles in accumulation mode without significant size dependence (Figure 4.5c).

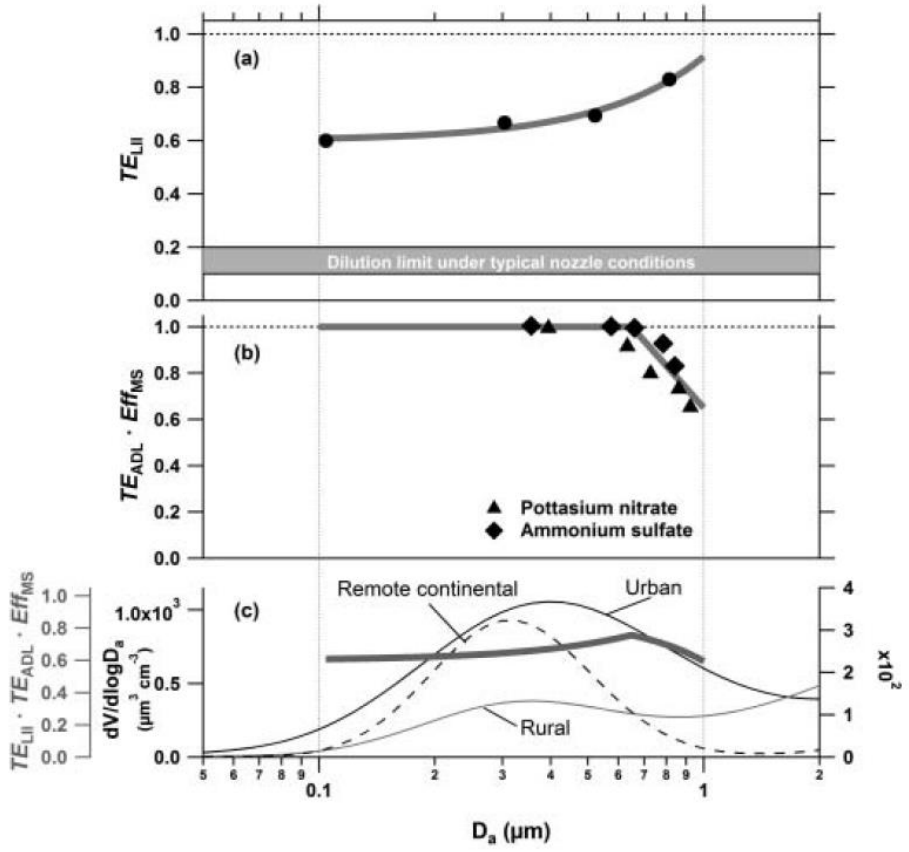

Figure 4.5. Size-dependent instrumental transfer function for the LII-MS system and typical volume size distribution in various atmospheric environments indicated in *Miyakawa et al.* 2014. (a) the throughput efficiency of the LII chamber (TE_{LII}); (b) transmission, collection, and vaporization efficiency of the PT-LDMS ($TE_{MS} \cdot Eff_{MS}$); (c) estimated transmission efficiency of LII-MS system ($TE_{LII} \cdot TE_{MS} \cdot Eff_{MS}$).

4.5. Analysis of Aerosol Composition Classified by the BC Mixing State

Figures 4.5a and 4.5b are the results of laboratory experiments of LII-MS reported by *Miyakawa et al.* [2014]. Propane flame soot particles coated with oleic acid (OL) were used as BC-containing particles (internally-mixed particle). Uncoated propane flame soot particles and $(NH_4)_2SO_4$ particles were used as BC-free particles (externally-mixed particle). Figure 4.6a shows the relationship between ΔQ_{28} and the OC mass of OL internally mixed with propane flame soot, obtained from both MS and LII-MS modes. The organic signals for the MS mode showed a

positive correlation with the carbon mass of OL. The signals derived from OC in LII-MS mode did not exceed the zero level. These results are proof that BC-containing particles are almost fully vaporized before they are transferred to the PT-LDMS when the LII laser is turned on. Mono-disperse $(NH_4)_2SO_4$ particles externally mixed with monodisperse fullerene particles were introduced to the LII-MS. Figure 4.6b shows the relationship between ΔQ_{48} (SO^+) and sulfate mass obtained in both the MS and LII-MS modes. No significant differences were found in the correlation of ΔQ_{48} with sulfate mass. These results demonstrates that BC-free particles are not affected by the LII laser and are transferred to the PT-LDMS.

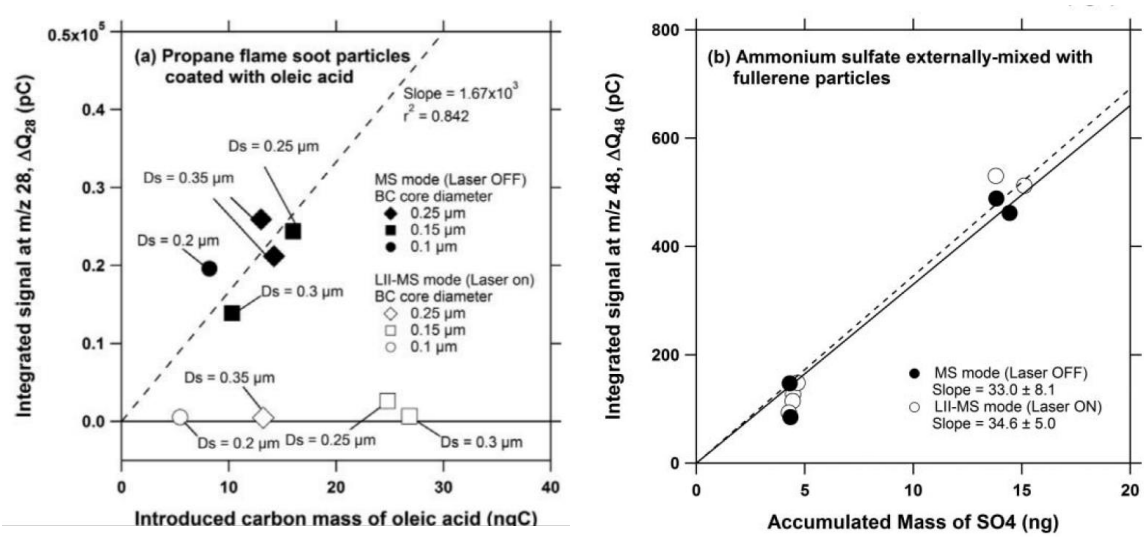

Figure 4.6. The correlation plots under the LII-MS and MS mode indicated by *Miyakawa et al.* [2014]: (a) the correlation plot of $\Delta Q28$ with the mass concentration of OC of oleic acid coating for BC-Containing particles. (b) the correlation plot of $\Delta Q48$ with the mass concentration of SO_4^{2-}.

4.6. Measurement cycle and error estimation

Figure 4.7 shows a schematic diagram of a measurement cycle in this study. The mass concentration of each chemical component for all particles (M_t^{off}) under the LII-MS ($t = t_{n+2}$) was estimated in order to calculate the mass concentration of compounds internally mixed with BC. The value of $M_{t_{n+2}}^{off}$ was estimated by linearly interpolating between $M_{t_{n+1}}^{off}$ and $M_{t_{n+3}}^{off}$. The difference between $M_{t_{n+2}}^{off}$ and $M_{t_{n+2}}^{on}$ was defined as the mass concentration of compounds internally mixed with BC at time t.

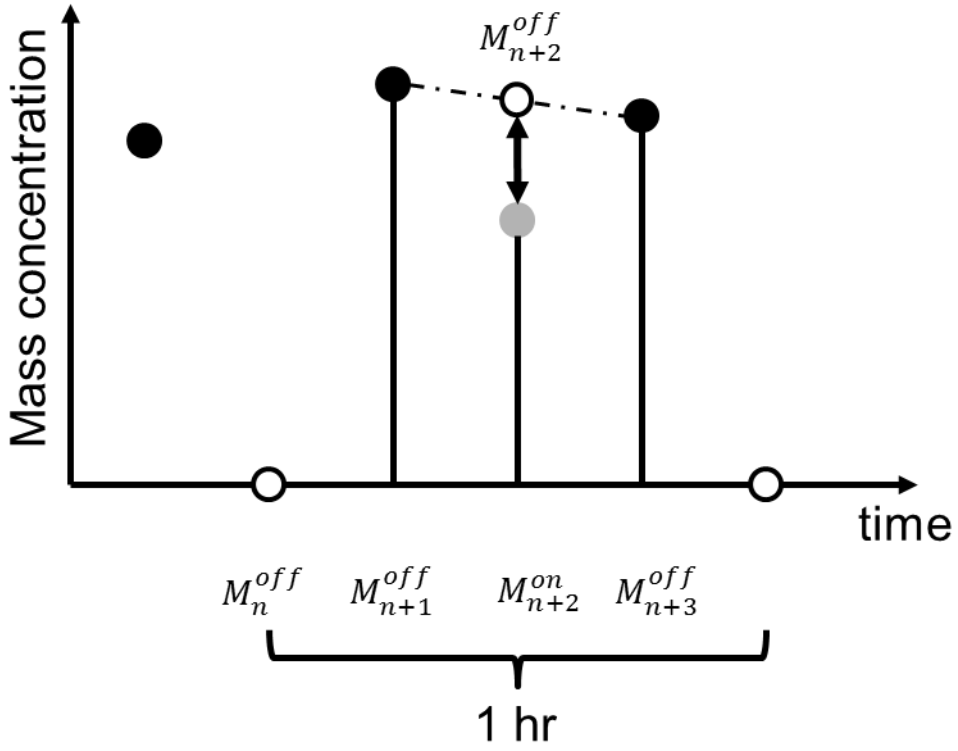

Figure 4.7. A schematic diagram of the measurement cycle used this study. Solid, shaded and open circles are the data sampling with the MS (LII laser off), LII-MS (LII laser on) mode, and zero air, respectively. The shaded circle indicates the BC-free particle. The difference between the dashed line (linear inter potation of the MS data) and shaded circle indicate the mass concentration of BC containing particles.

Potential errors can occur when estimating BC-containing particles using the LII-MS system. These errors are caused by calculating the difference between $M^{\mathrm{off}}_{\mathrm{t_{n+2}}}$ and $M^{\mathrm{on}}_{\mathrm{t_{n+2}}}$. In this method, uncertainty occurs when the mass concentration is near the limit of detection (LOD) or when it changes in a short time. The LOD can be determined from the signal-to-noise ratio of the mass spectrometer. During the measurements carried out in this research (presented in Chapter 5), most of the mass concentrations of the chemical components were sufficiently larger than the LOD. Relative changes in mass concentration within one laser on/off cycle were used as an indicator of uncertainty. The relative mass concentration change ratio (R) is defined as follows.

$$R = \frac{\Delta M}{M} \cdot \frac{1}{\Delta t}\bigg|_{t=t_{n+2}} = \left(\frac{M^{\mathrm{off}}_{t_{n+3}} - M^{\mathrm{off}}_{t_n}}{M^{\mathrm{off}}_{t_{n+2}}} \right) \cdot \frac{1}{\Delta t} \ , \qquad (4.1)$$

Here, Δt represents the time (30 min) of one measurement cycle. The standard deviation (σ) of the value of R calculated in MS mode is used as the uncertainty, including the aforementioned relative changes. The ratio of BC-containing particles to all particles in LII-MS mode was compared with this standard deviation, and it seems that data with values less than σ should be indistinguishable from error. Therefore, this σ was used as the LOD of the LII-MS mode. The details for screening using this LOD are described in Chapter 5.

Reference

Miyakawa, T., N. Takeda, K. Koizumi, M. Tabaru, Y. Ozawa, and N. Takegawa, (2014), A New Laser Incandescence-Mass Spectrometric Analyzer (LII-MS) for Online Measurement of Aerosol Composition Classified by Black Carbon Mixing State. *Aerosol Sci. Technol.* 48:853-863

Moteki, N. and Kondo, Y. (2007). Effects of Mixing State on Black Carbon Measurements by

Laser-Induced Incandescence. Aerosol Sci. Technol., 41:398-417.

Moteki, N. and Kondo, Y. (2010). Dependence of Laser-Induced Incandescence on Physical Properties of Black Carbon Aerosols: Measurements and Theoretical Interpretation. Aerosol Sci. Technol., 44:663-675

Moteki, N. Takegawa, N. Koizumi, K., Nakamura, T., and Kondo, Y. (2011). Multi-Angle Polarimetry of Thermal Emission and Light Scattering by Individual Particles in Airflow. Aerosol Sci. Technol., 45:1184-1198.

Onasch, T. B., A. Trimborn, E. C. Fortner, J. T. Jayne, G. L. Kok, L. R. Williams, P. Davidovits and D. R. Worsnop, (2012), Soot Particle Aerosol Mass Spectrometer: Development, Validation, and Initial Application, *Aerosol Sci. Technol.*, 46:804-817.

Ozawa, Y., N. Takeda, T. Miyakawa, M. Takei, N. Hirayama, and N. Takegawa, (2016). Evaluation of a particle trap laser desorption mass spectrometer (PT-LDMS) for the quantification of sulfate aerosols. *Aerosol Sci. Technol.* 2: 173-186.

Schwarz, J. P., Gao, R. S., Fahey, D. W., Thomson, D. S., Watts, L. A., Wilson, J. C., et al. (2006). Single-Particle Measurements of Midlatitude Black Carbon and Light-Scattering Aerosols from the Boundary Layer to the Lower Stratosphere. J. Geophys. Res., 111:D16207, doi:10.1029/2006JD007076.

Takegawa, N., T. Miyakawa, T. Nakamura, Y. Sameshima, M. Takei, Y. Kondo, and N. Hirayama, (2012). Evaluation of a new particle trap in a laser desorption mass spectrometer for online measurement of aerosol composition. *Aerosol Sci. Technol.* 46:428-443.

5. Field measurements of BC mixing state

5.1. Introduction

Emissions of trace gases and aerosols from industrial sources, biomass burning, and natural source in East Asia contribute significantly to the global budget of aerosols [e.g. *Streets et al.* 2003; *Wang et al.* 2006; *Jiang et al.* 2013]. Several observational studies were conducted in East Asia to quantify the chemical composition of aerosol particles, investigate the formation process of aerosols, and estimate the optical and hygroscopic properties of aerosol particles [e.g. *Guo et al.* 2013; *Cui et al.* 2016]. Previous studies revealed extremely high concentration of sulfate in northern China when air masses were stagnant on a regional scale [*Takegawa et al.* 2009; *Guo et al.* 2013]. High concentrations of nitrate were also observed in northern China in low temperature conditions [*Guo et al.* 2014]. These studies provide useful insights into the formation processes of aerosols in East Asia, however, variability in the mixing state of BC particles remain poorly understood, although they represent an important parameter for the estimation of the radiative impact of aerosols.

Measurements of the mixing states of BC in East Asia were mostly conducted using a volatility tandem differential mobility analyzer (VTDMA), [*Chen et al.* 2012] or single particle soot photometer (SP2) [e.g. *Shiraiwa et al.*, 2009; *Moteki et al.*, 2010; 2014]. These techniques can quantify the number size distribution of BC-containing particles with high precision, but do not provide quantitative information on the chemical composition of aerosol particles internally or externally mixed with BC.

Ground-based measurements of aerosols were conducted in Korea in the spring of 2016. The chemical composition of aerosols internally or externally mixed with BC were measured using the

LII-MS. The purpose of this study is to investigate the variability in the mixing state of BC-containing particles in Asian outflow and possible mechanisms affecting this variability.

5.2. Measurements

5.2.1. Measurement site

The measurements were conducted from March 26 to April 7, 2016, on the Gwangju Institute of Science and Technology (GIST) campus (35°13′N, 126°50′E, as shown in Figure 5.1). A previous study showed that air sampled at this site is generally affected by both the regional scale pollution from the Asian continent and, emission from local sources depending on meteorological conditions and wind directions [*Park et al.* 2012]. The local emission sources include residential/commercial areas (~0.6 km away from the site), major highways (~1.5 km away from the site), small industrial areas (~1.5 km away from the site), and agricultural areas (~0.8 km away from the site). In addition, a major industrial area is located approximately 90 km southeast from the site.

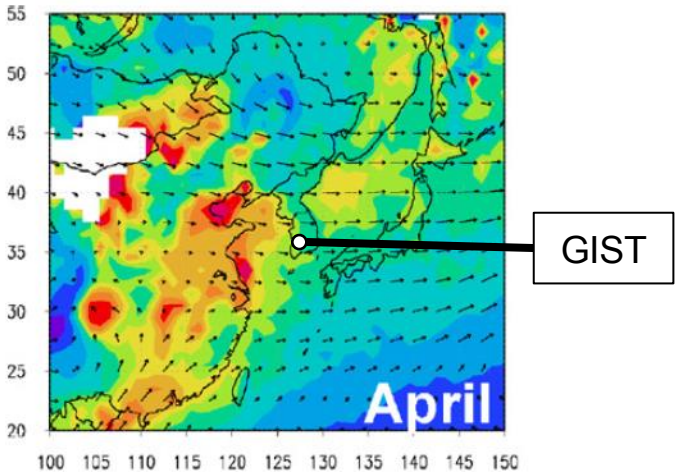

Figure 5.1. Location of the measurement site. Location of GIST is depicted on an image of aerosol optical depth by moderate resolution imaging spectrometer (MODIS) [*Kim et al.* 2007].

5.2.2. Instruments

The LII-MS analyzer was used to measure the aerosol chemical composition that was internally and externally mixed with BC. In this chapter, the particles internally and externally mixed BC referred to as named BC-containing and BC-free particles, respectively. Mass concentration of nitrate (NO_3^-) and sulfate (SO_4^{2-}) were determined by the sensitivity of routine calibrations during the measurements (Appendix 5.1). In this chapter, the mass concentrations of SO_4^{2-}, NO_3^-, and BC are represented as M_{SO4}, M_{NO3}, and M_{BC}, respectively. Because mass concentrations of organic matter (OM) have not been estimated, the ion current signal of m/z 44 was expressed as a relative value of OM. We compared LII-MS signals with OM mass concentrations in laboratory experiments using oxalic acid particles. Resultantly, we found that the signal with a value of 3.0×10^4 pC at m/z 44 corresponds to approximately ~15 μg m^{-3}.

An aethalometer (AethLabs, Magee Scientific, Berkeley, CA, USA) was used to measure the M_{BC} [*Hansen et al.* 1984]. The aethalometer determines the M_{BC} of particles by the spectral absorption of seven wavelengths [*Hansen et al.* 1984]. The aerosol samples introduced into the aethalometer are dried using a diffusion dryer that is placed upstream of the aethalometer. The limit of detection (LOD) is about 0.3 μg C m^{-3} [*Batmunkh et al.* 2016].

Filter samples were collected for offline analysis of $PM_{2.5}$ chemical composition. The integration time for sampling was 24 h. A total of 18 samples were obtained during the measurement period. Ion chromatography was used to quantify the mass concentration of ionic species. The instruments used for the ambient measurements are summarized in Table 5.1.

Table 5.1. Instruments using the ambient measurements

instrument	Target	LOD	Time resolution
LII-MS	mass concentration of sulfate, nitrate, and organics mixed with BC	Same as PT-LDMS	1 h
LII	BC, aerosol size distribution	-	2 min
PT-LDMS	mass concentration of sulfate, nitrate, and organics	Sulfate: 0.5 Nitrate: 0.4	15 min
Aethalometer	mass concentration of BC	0.05 ug	1 min
SMPS	aerosol size distribution	-	5 min
Filter	mass concentration of ions	0.1 ug	12 h

5.2.3. Limit of detection

The limit of detection (LOD) of the LII-MS analyzer is evaluated in this section. The uncertainty in estimating the internally mixed fraction becomes larger if there is a rapid change in the mass concentration during the laser on/off cycle, namely, the data obtained in LII-MS mode and MS mode. The mass concentrations calculated by linear interpolation can contain uncertainties when the mass concentrations are close to the LOD of the PT-LDMS, or when they show large temporal variability within a short time period, as described in Section 3. The LOD of the PT-LDMS was estimated by the same method described in Section 3.4. The values of the LOD for SO_4^{2-} and NO_3^- in the current instrumental setup were estimated to be 1.4 (± 0.6) μg m^{-3} and 2.9 (± 0.7) μg m^{-3}, respectively. During the measurement period, most of the data exhibited higher M_{SO4} and M_{NO3} than these LOD values. A measure of the uncertainty due to the LII laser on/off cycle was defined as R, as described in Section 3. The R-value of the measurements using only the PT-LDMS was calculated and the standard deviation (σ) of R was defined as the LOD of the measurements obtained with the LII-MS analyzer. This LOD was compared with the value of R calculated from the measurements of the LII-MS analyzer, and the data of the LII-MS analyzer

were screened.

5.2.4. Error estimation

The uncertainty of the data obtained with the LII-MS analyzer was estimated from possible random and systematic errors. The error in the mass concentration of aerosol particles measured by the LII-MS analyzer is mainly caused by the PT-LDMS measurement and calibration. Error factors were discussed in Section 3.4. The major error factors of the LII-MS are the error in size cut of the inlet and error due to the volatility efficiency of the chemical composition of aerosol particles. The error of the inlet also includes the uncertainty of the transmission efficiency of the LII. For calibration errors, the values described in Section 3.4 were and used with (± 5%). The uncertainties of the LII-MS are discussed below. Hereafter, the positive and negative signs of systematic errors indicate overestimation and underestimation, respectively.

The potential uncertainties of the inlet were caused by the size cut of the PT-LDMS inlet and the transmission efficiency of the LII. The size cut of the PT-LDMS and transmission efficiency of the LII were described in Section 3. The uncertainty related to the transmission efficiency of the LII can be cancelled out by a comparison between the ambient and calibration conditions. Therefore, by comparison with the filter analysis, the difference between the size cut of the inlet of the PT-LDMS (PM_1) and the size cut of the filter analysis ($PM_{2.5}$) is a major factor determining the uncertainty. As shown in Figure 5.2, the mass size distribution of the aerosol obtained during the measurement period was close to a typical urban size distribution, with a peak diameter of ~400 nm. The systematic error calculated using the measured size distribution and the size cut of the aerodynamic lens of the previous study was −12%.

As discussed in Section 3.4, the potential uncertainties in the vaporization are stem from

incomplete volatilization and refractory materials with a decomposition temperature that is above the trap temperature of the PT-LDMS. Regarding the former, the uncertainty due to the incomplete volatilization of SO_4^{2-} was calculated as the ratio of the zero-air signal to the particle signal for the signal of m/z 48, and the result was −15%. Because nitrate materials have a low decomposition temperature (100 − 200 °C), incomplete volatilization is unlikely. Therefore, the contribution to uncertainty due to the incomplete vaporization of NO_3^- is negligible. Regarding the latter, the influence of materials with a decomposition temperature higher than the trap temperature of the PT-LDMS (~400 °C) was estimated from cations (K^+, Na^+, Mg^{2+}, Ca^{2+}) measured by filter analysis. The possible uncertainties of SO_4^{-2} and NO_3^- caused by refractory materials were −12% and −7%, respectively.

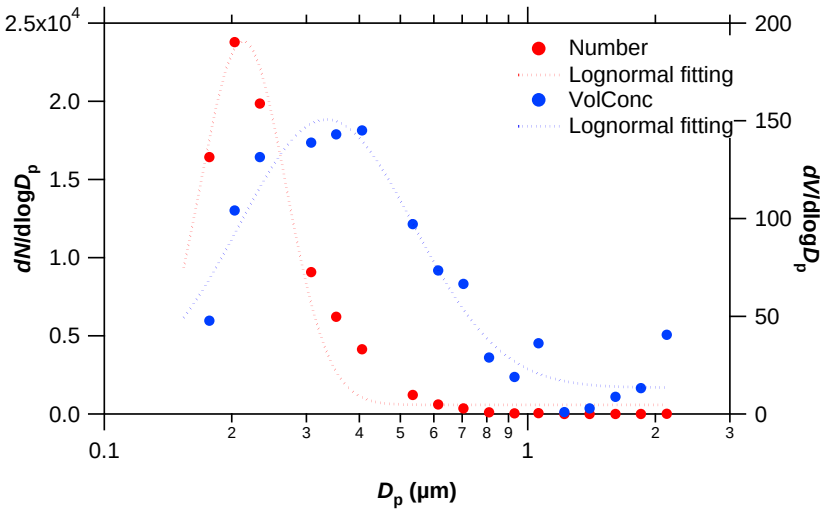

Figure 5.2. Typical number (red) and volume (blue) size distributions by LII using scattering signal.

5.2.5. Comparison with filter analysis

The M_{SO4} and M_{NO3} measured using the LII-MS analyzer were compared with those obtained by filter analysis, as shown in Figure 5.3. The data of the LII-MS analyzer were averaged over 12 h for consistency of the time resolution for the filter analysis. Note that the LII-MS data contains mass concentrations measured by the parallel and tandem modes as described in Section 4.2. The PT-LDMS measurements were conducted before the measurement period analyzed in this study. The PT-LDMS was calibrated using the method described in the work of *Ozawa et al.* [2016], and M_{SO4} and M_{NO3} obtained in the parallel mode were calculated by linear regression with the time series of the sensitivity data. The mass concentrations obtained by filter analysis were calculated as 25 °C and 1 atm conditions. The error bars in Figure 5.3 depict the uncertainties of the LII-MS analyzer. The uncertainties are discussed in the previous section.

The uncertainty of the filter is considered to account for the errors in the extracted volume, sampling flow rate, and calibration curves, as well as errors caused by volatilization during sampling. It is difficult to estimate these errors. In a previous study, the uncertainties of SO_4^{2-} and NO_3^- were ± 25% [*Manuel et al.* 2012]. The systematic random errors were calculated to be 20% and ± 5%, respectively, from the uncertainties of the LII-MS analyzer described in the previous section. The data of SO_4^{2-} and NO_3^- was distributed within ± 25%, including the errors. The inorganic salt measurements obtained with the LII-MS analyzer after averaging over 12 hours of the measurement period were consistent with the filter analysis within ± 25%. The two measurements agreed within their corresponding errors.

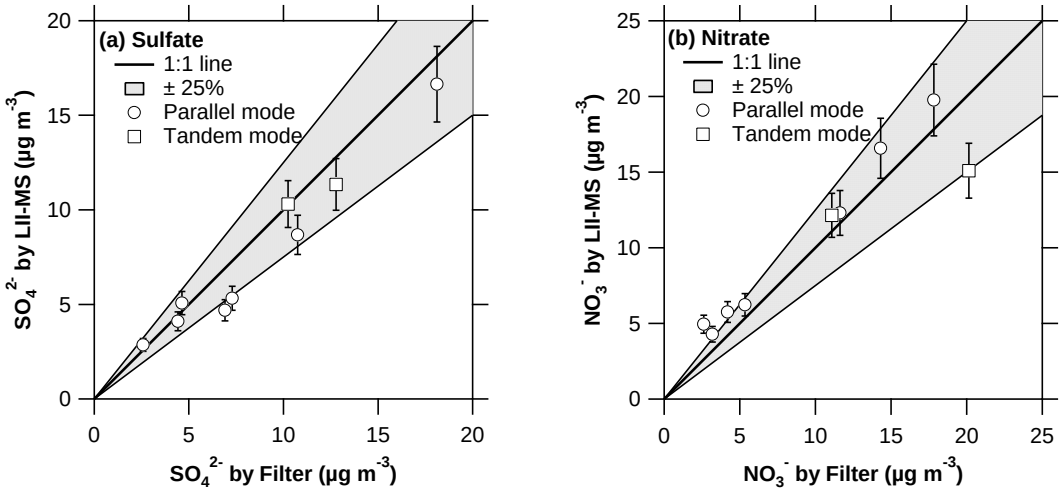

Figure 5.3. Correlation plots of LII-MS versus filter analysis for mass concentrations of (a) $SO_4^{2-}$and (b) NO_3^-. The LII-MS averaged over 6 h were used for comparison with filter analysis data. The circles represent the LII-MS data measured by MS mode and quadrangles represent the LII-MS data measured by LII-MS mode. The solid line indicates a 1:1 correspondence. The shaded region shows the ± 25% range.

5.3. Metrological Conditions

5.3.1. Characterization of Air Mass

Three-day backward trajectories for sampled air were calculated using the hybrid single-particle lagrangian integrated trajectory (HYSPLIT) model [*Draxler and Hess* 1998; *Stein et al.* 2015] (http://ready.arl.noaa.gov/HYSPLIT.php). The subplots in Figure 5.4 show examples of trajectories classified by possible origins of air parcels. China air masses (CH) were defined as those originating from the northern or eastern part of China. Stagnated air masses (ST) were defined as those stagnated around Korea at least two days prior to the measurement. Maritime air masses (MR) were defined as those originating from the East China Sea. Free troposphere air masses (FT) were defined as those originating from the free troposphere.

The temporal variation of the meteorological field around the observation site were characterized by a sequential passage of synoptic scale disturbances, namely, low-pressure and

high-pressure systems, which passed near the Korean peninsula. When CH-type air masses were sampled, a low-pressure system passed over the north side of the Korean Peninsula and air in the cold side of cold front reached the observation site. In contrast, when ST-type air was sampled, a high-pressure system covered the Korean Peninsula and weak wind resulted in the stagnation of air around the observation site. The low-pressure and high-pressure systems periodically moved from west to east during the measurement period. In summary, the backward trajectory analyses suggest that the air sampled during the observation period was generally transported from over the Asian continent to the Korean peninsula except for the ST-type air occasionally sampled.

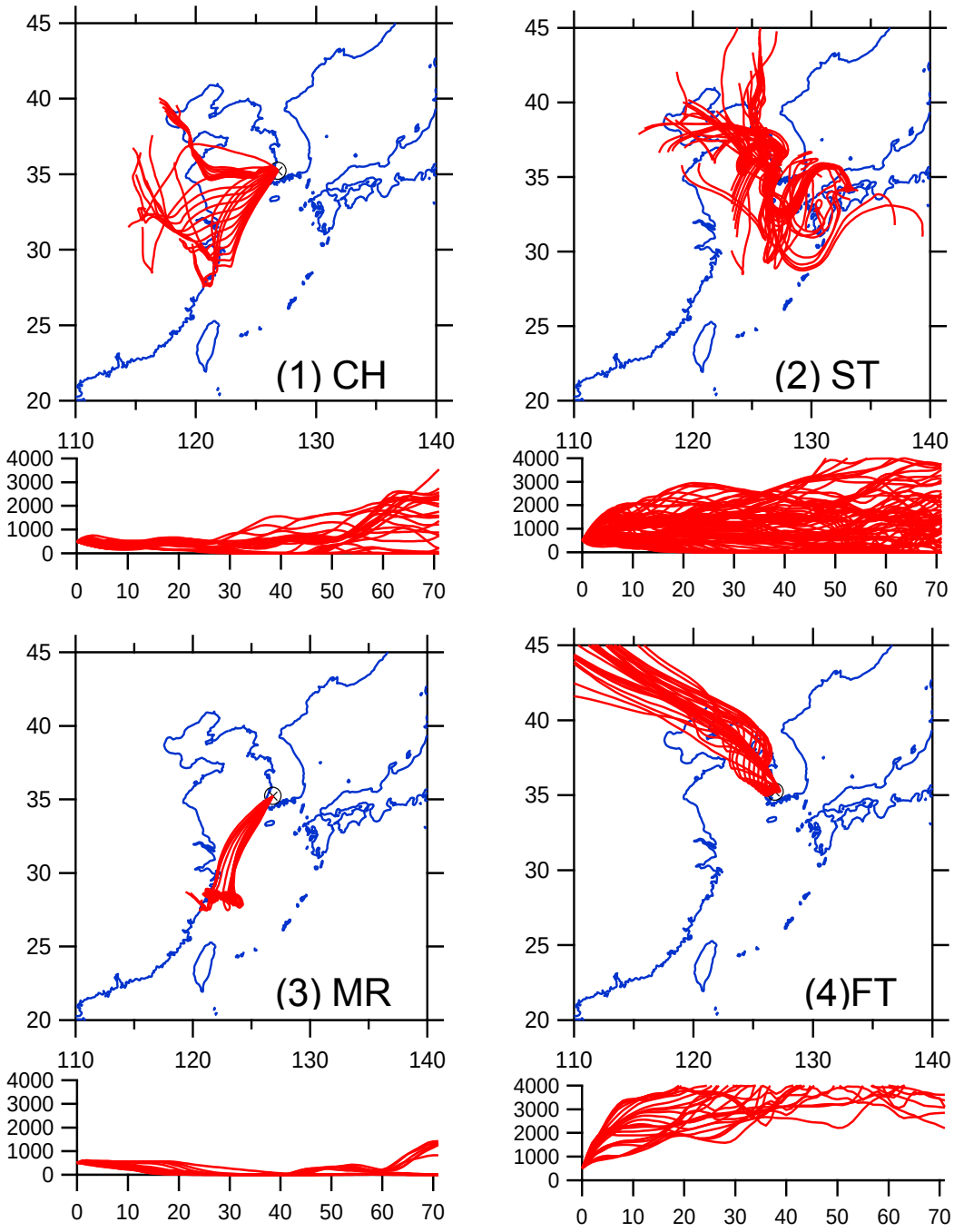

Figure 5.4. Horizontal and vertical plots of backward trajectories of air mass of the following types: China (CH, left top), Stagnant (ST, right top), (c) Maritime (MR, left down), and free troposphere (FT, right down). 3-day backward trajectories calculated using the national oceanic and atmospheric administrations (NOAA) HYSPLIT model. The trajectories were calculated every hour during the measurement period.

5.3.2. Local meteorological data

Figure 5.5 shows the time series of air temperature, relative humidity (RH), precipitation, wind speed, and wind direction measured at the observation site. Classification of the sampled air described in the previous section is also shown in this figure. When local meteorological data were not available, data obtained by the Korea Meteorological Agency (KMA) (http://www.weather.go.kr/) are shown. The temperatures were 5 – 10°C during the first half of the measurement period, but it rose to 10 – 15°C in the latter half. The temperature of the first half was lower than that in the latter half. The wind direction at the observation point was typically north or south, depending on the meteorological conditions, and generally corresponded to the air type (origin of air) described above. Relatively strong wind of speeds greater than 4 m s^{-1} were observed on March 29, but in other periods, weak winds of 0 – 2 m s^{-1} were generally observed. Precipitations rarely occurred during the measurement period, except on April 3.

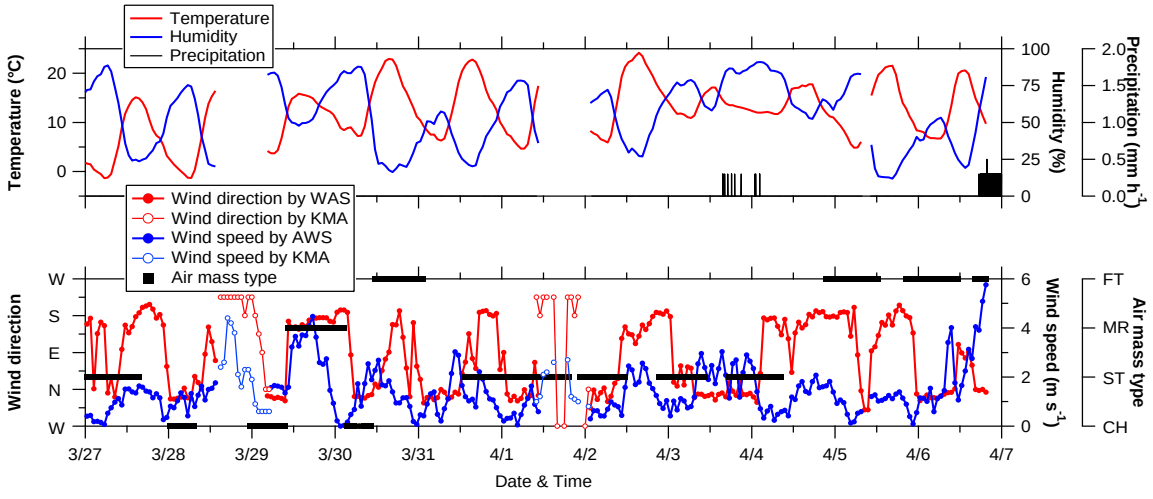

Figure 5.5. Time series during the measurement period. Upper graph: air temperature, relative humidity, precipitation. Lower graph: wind direction at GIST campus, wind direction at Gwangju weather station (red open circle and line), wind speed (blue marker and line), and air mass type (rectangle marker). AWS is the Automatic Weather Station of GIST. KMA is the Korea Meteorological Administration. Air mass types are represented in Section 5.3.1.

5.4. Results

5.4.1. Mass concentrations and temporal variation

Figure 5.6 shows temporal variations of M_{SO4}, M_{NO3}, M_{BC}, and, *m/z* 44 signal (a major fragment ion of organic aerosols) during the measurement period. Mass concentrations of BC-containing and BC-free particles are separately shown for M_{SO4}, M_{NO3}, and *m/z* 44 signal. The M_{SO4} and M_{NO3} were calculated using the sensitivity calibrated using $(NH_4)_2SO_4$ and NH_4NO_3 particles, as described in Section 5.2.2. The mass concentrations measured by the LII-MS analyzer contain an uncertainty that depends on the relative change in the mass concentration within one cycle of the LII laser on/off modulation [*Miyakawa et al.* 2014]. When changes in mass concentrations between the laser on and off modes within each measurement cycle are lower than the limit of detection (LOD), the data are discarded and not used in the following analyses. The averages of the observed values are summarized in Table 5.2.

Table 5.2. Averages of measured parameters

	SO_4^{2-} (μg m^{-3})	NO_3^- (μg m^{-3})	m/z 44 (pC)
M^{all}	8.2 ± 3.6	13.7 ± 6.7	17207.1 ± 7278.6
M^{int}	1.5 ± 0.9	2.1 ± 1.3	3246.0 ± 2066.4
M^{ext}	6.7 ± 3.3	11.6 ± 6.0	13961.0 ± 6474.8
G^{all}	0.26 ± 0.07	0.45 ± 0.07	0.28 ± 0.06
G^{int}	0.27 ± 0.11	0.43 ± 0.10	0.30 ± 0.12
G^{ext}	0.27 ± 0.08	0.46 ± 0.08	0.27 ± 0.06
F	0.19 ± 0.10	0.16 ± 0.08	0.19 ± 0.10

The total M_{SO4} and M_{NO3} varied in ranges of 1 – 15 μg m^{-3} and 5 – 35 μg m^{-3}, respectively. NO_3^- was the most abundant species during the measurement period. Because the temperature was low (~15°C) during the measurement period, M_{NO3} tended to be higher. As described above, concentrations of OM have not been estimated in this study, and the ion current signal for m/z 44 was shown for OM. A signal with a value of 3.0×10^4 pC at m/z 44 corresponds to approximately ~15 μg m^{-3} (Section 5.2.2.). The time series of M_{SO4}, M_{NO3}, and m/z signal did not show clear diurnal variations, while they did exhibit day-to-day variations, which were similar to each other (Figure 5.6e). In fact, as shown in Figure 5.7, one-hour data of M_{NO3} and M_{SO4} show a clear positive correlation ($r^2 = 0.8$).

M_{BC} varied in range of 1 – 5 μg m^{-3}. Spikes of very high values within short time periods (typically ~30 minutes) were frequently observed in the temporal variation of BC (e.g., March 27 daytime, March 29 nighttime, and April 5 nighttime). These high values were quite likely due to local emission sources, namely combustions near the observation site. The temporal variations of BC other than these spikes generally took place with day-to-day time scales and they were similar to those of NO_3^- and SO_4^{2-}. The temporal variations of NO_3^-, SO_4^{2-}, and BC did not exhibit clear diurnal variations. Because BC (primary aerosols introduced to the atmosphere by emission sources) and inorganic aerosols (secondary aerosols formed in the atmosphere) show similar day-to-day variations, these temporal variations were likely caused by synoptic scale meteorological variations, namely regional scale transport of pollutant air masses. This argument is further examined using backward trajectories as below.

The mass concentrations (and ion signal) of the aerosols (M_{SO4}, M_{NO3}, M_{BC}, and *m/z* 44 signal) were highest in the morning of March 29. Backward trajectory analyses showed that CH-type air masses (air transported from China, Section 5.3.1 and Figure 5.4) were sampled in this event. After

this event, a rapid decrease in concentrations was observed in association with changes in the local wind speed/direction. Trajectory analyses show that sampled air was of the MR-type air mass, which likely stagnated over the Yellow and East China Sea. Thus, it was less influenced by anthropogenic emissions. After April 4, mass concentrations of aerosols remained low (~5 − 10 μg m^{-3}) and sampled air was found to be of the FT-type air mass, which descended from the free troposphere (FT) to the planetary boundary layer (PBL) within a few days prior to the observations. FT air is considered to be clean (less affected by recent anthropogenic or natural emissions), and therefore, the observed low aerosol concentrations were considered to be consistent with these trajectory analyses. The average mass concentrations of sulfate and nitrate (M_{SO4} and M_{NO3}) for each air mass category are summarized in Figure 5.8. Averages of M_{SO4} and M_{NO3} were highest in CH-type air masses. Conversely, they were lowest in FT-type air masses. These results indicate that the observed chemical properties (aerosol mass concentrations) and meteorological properties (air mass type) are generally consistent during the measurement period.

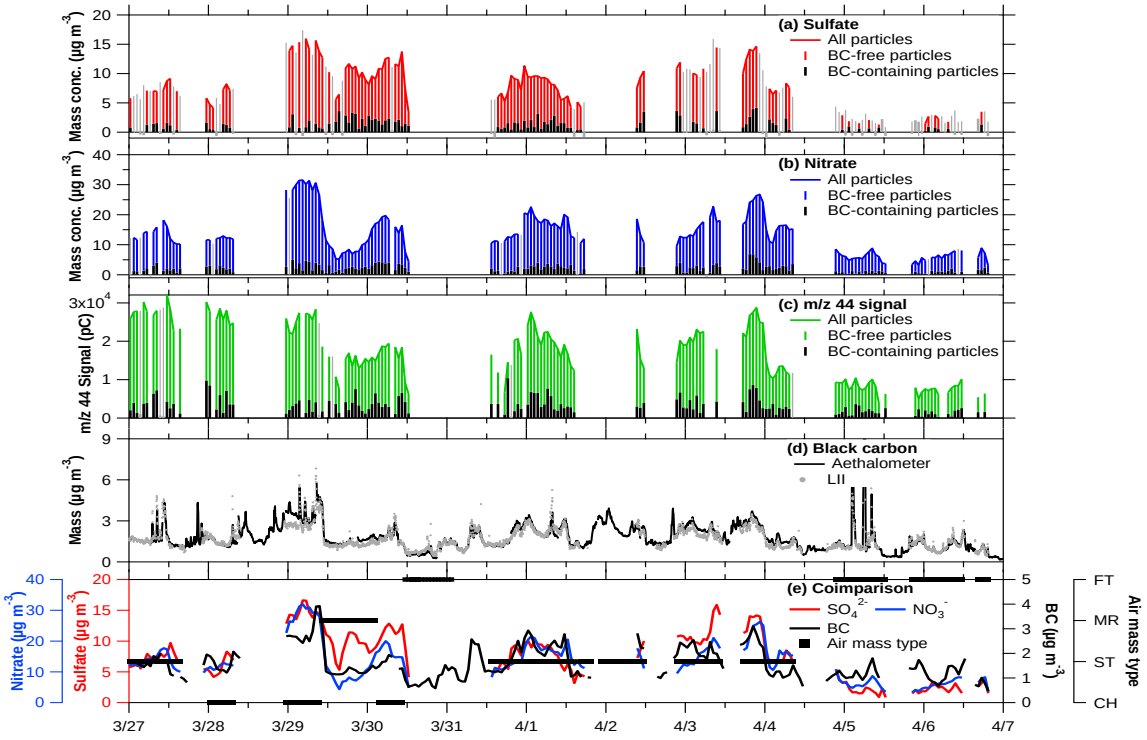

Figure 5.6. Temporal variations of (a) M_{SO4}, (b) M_{NO3}, and (c) M_{m44} signals for BC-containing (black color bars), BC-free (red, blue and green color bars), and all (red, blue and green lines) particles. (d) Temporal variations of M_{BC} particles obtained by the LII (shaded circles) and by the aethalometer (solid line) with air mass types (quadrangle marker). (e) Temporal variations of M_{SO4} (red line), M_{NO3} (blue line) and M_{BC} (black line). Mass concentrations of BC-free particles stack on top of those of BC-containing particles in figure (a), (b) and (c).

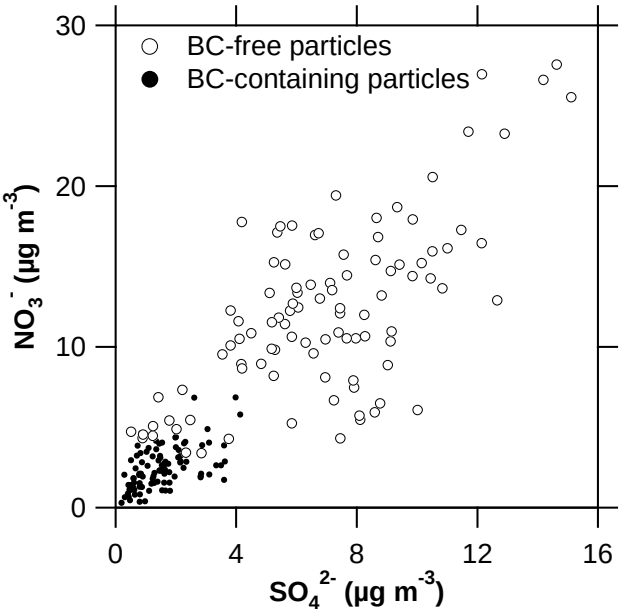

Figure 5.7. Scatter plots of M_{NO3} versus M_{SO4}. Open circles depict the BC-free particles and black circles depict the BC-containing particles.

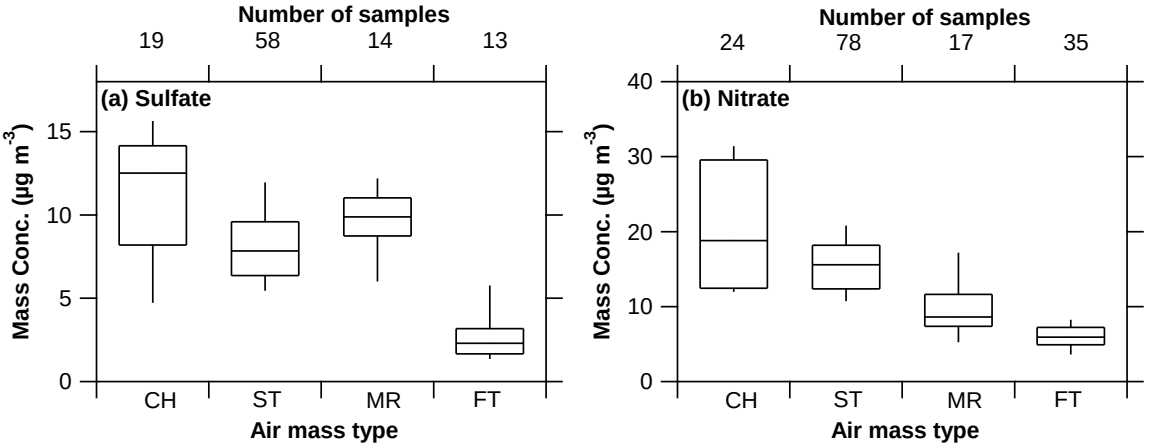

Figure 5.8. Mass concentration of (a) sulfate and (b) nitrate for each air mass category. Numbers above the plots depict the number of samples. Box plots show the median and 25 − 75 % of data. The bars depict the 10 − 90% range.

5.4.2. Mixing state: mass fraction with BC-containing and BC-free particles

The relative fractions of M_{SO4} (or M_{NO3} or M_{m44}) in the total aerosol mass (summation of M_{SO4}, M_{NO3}, and M_{m44}) are separately calculated for BC-containing and BC-free particles as below.

$$G_x^y = \frac{M_x^y}{M_{SO4}^y + M_{NO3}^y + M_{OM}^y} \left(x = SO_4^{2-}, NO_3^-, m44; y = int, ext\right), \qquad (5.1)$$

where "int" and "ext" express the internal and external mixture, respectively. M_{m44} was calculated from m/z 44 signals using the sensitivity estimated from laboratory experiment with oxalic acid (as described in Section 5.3.2).

Figure 5.9 shows the time series of the G_x^y values. The average values of G_x^y are summarized in Table 5.2. As shown in this figure and table, on average, there were no clear differences in G_x^y values between BC-containing and BC-free particles as well as all particles (fractions for the sum of BC-containing and BC-free particles). However, temporal variations of one-hour G_x^y values are not necessarily similar between internally and externally mixed compounds. In fact, a scatter plot between the 1-hour values of G_{SO4}^{int} and G_{SO4}^{ext} shows no clear correlation between these two parameters ($r^2 = 0.2$, Figure 5.10).

These results suggest that on average, the growth of individual inorganic aerosol compounds takes place concurrently between BC-containing and BC-free particles: when BC-free particles grow by secondary production processes, BC-containing particles also grow leading to increases in a coating thickness of BC particles. However, there are some processes, which can change G_x^y values in different ways between BC-containing and BC-free particles, and these processes likely generate different temporal variations between BC-containing and BC-free particles. Possible mechanisms of these processes are discussed in section 5.5.

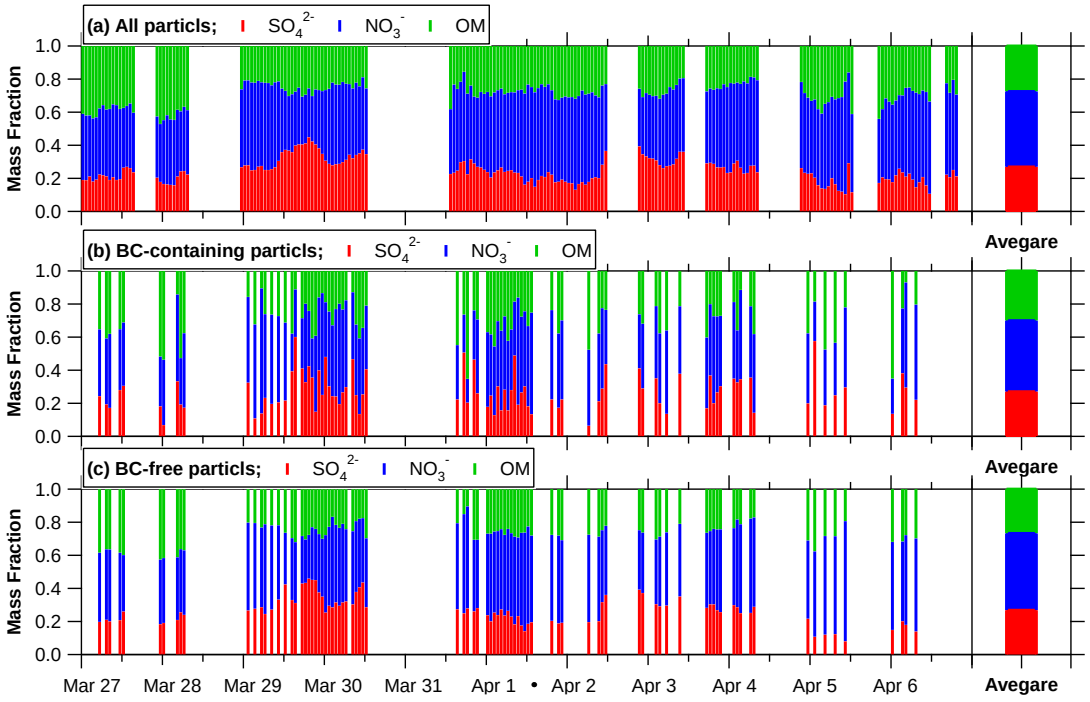

Figure 5.9. Temporal variations of the mass fraction of (a) all particles, (b) BC-containing particles and (c) BC-free particles.

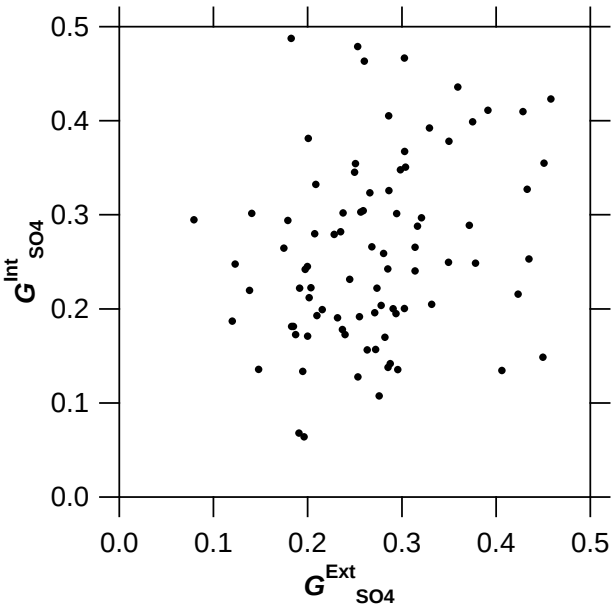

Figure 5.10. Scatter plot of G^{int}_{SO4} and G^{ext}_{SO4}.

5.4.3. Mixing state: mass fraction between BC-containing and BC-free particles

The mass fraction of species x internally mixed with BC within the total mass concentration of this species (sum of internally and externally mixed amounts), F_x (subscript x indicates the chemical component), is defined as follows:

$$F_x = \frac{M_x^{int}}{M_x} \quad \left(x = SO_4^{2-},\ NO_3^-,\ OM\right). \tag{5.2}$$

where M_x^{int} is the mass concentration of species x internally mixed with BC, and M_x, is the total mass concentration of species x. Figure 5.11 shows temporal variations of F_{SO4}, F_{NO3}, and F_{m44}. The average values of F_x are summarized in Table 5.2. Evident diurnal variations were not observed. Figure 5.12 shows the histograms of F_{SO4}, F_{NO3}, and F_{m44}. There were no significant differences in the values of among F_{SO4}, F_{NO3}, and F_{m44} on average. Their values ranged from 0.16 to 0.19.

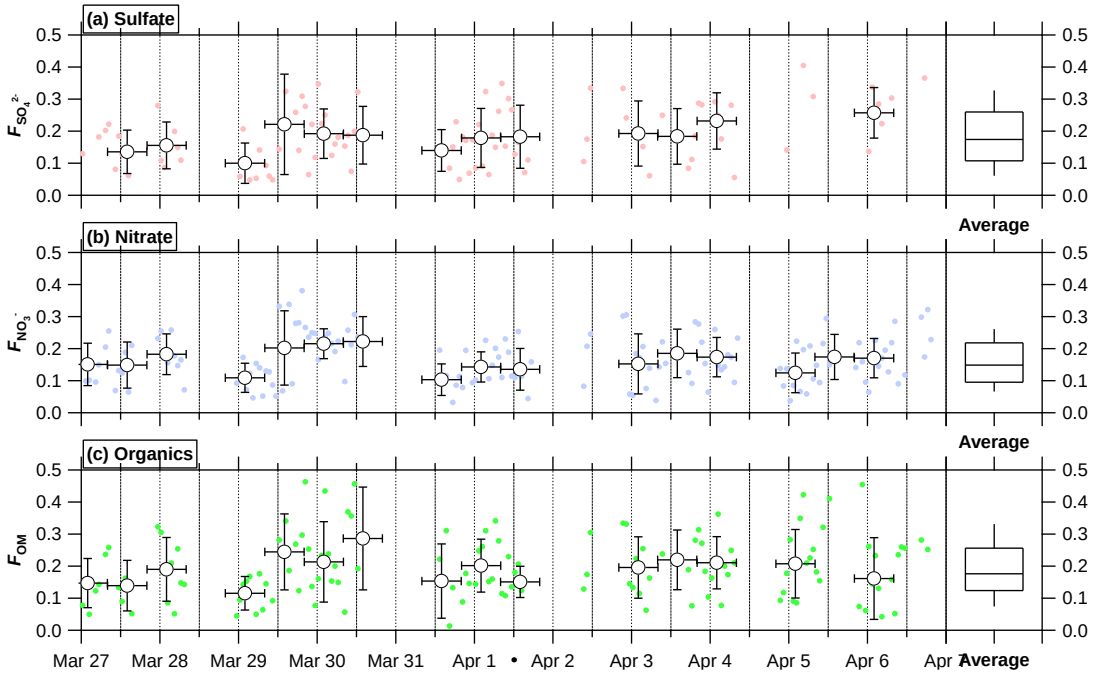

Figure 5.11. Temporal variations of the mass fraction for the internal mixture to all particles for (a) sulfate, (b) nitrate and (c) organics.

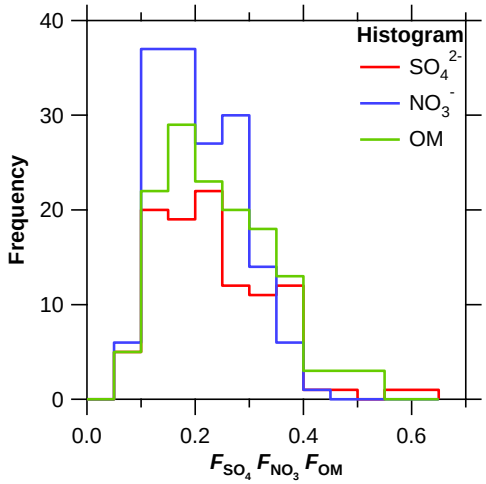

Figure 5.12. Histograms of F_{SO4} (red), F_{NO3} (blue), and F_{OM} (green).

Figure 5.13 shows scatter plots of F_{NO3} and F_{OM} versus F_{SO4}. The open circles in this figure denote averages for F_{SO4}, F_{NO3}, and F_{OM} values within their individual data ranges (bin average). The F values depict weak correlations. The r^2 was 0.4 for the one-hour value and 0.6 for the average value.

The averages of F_{SO4} and F_{NO3} internally mixed fractions of sulfate and nitrate for each air mass category are summarized in Figure 5.14. The average F_{SO4} value was lowest and highest for CH-type and FT-type air, respectively. As previously, shown in Figure 5.8, the absolute mass concentrations of SO_4^{2-} and NO_3^- (M_{SO4} and M_{NO3}) were the highest and lowest in CH-type and FT-type air, respectively. These results indicate that on average, although mass concentrations of SO_4^{2-} were highest in CH-type air (polluted air), relative fractions of aerosol amounts, which internally mixed with BC, were lowest. High mass concentrations of SO_4^{2-} accounted for externally mixed compounds. On the other hand, systematic differences in F_{NO3} values were not observed according to the air mass type.

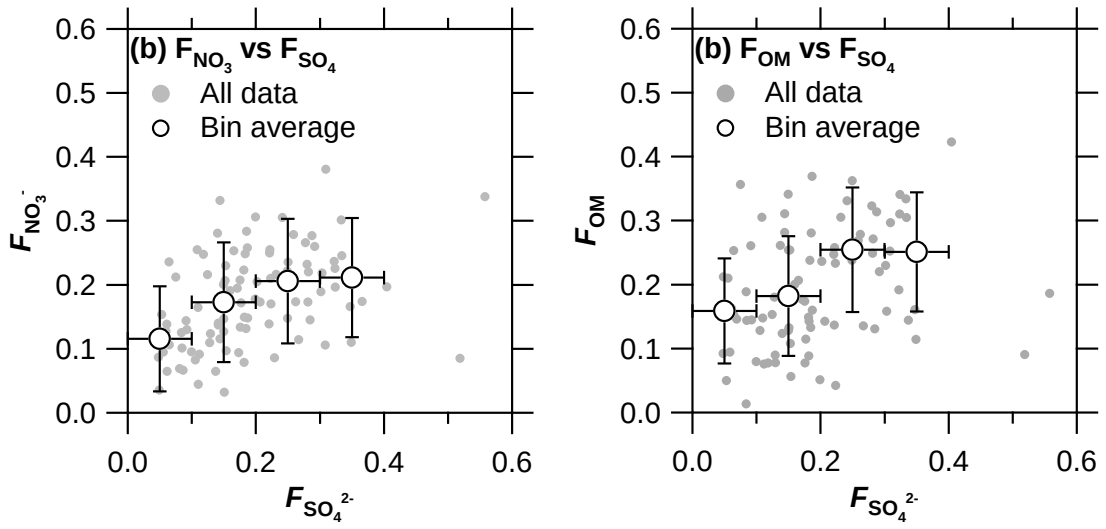

Figure 5.13. Scatter plots of (a) F_{NO3} versus F_{SO4} and (b) F_{OM} versus F_{SO4}.

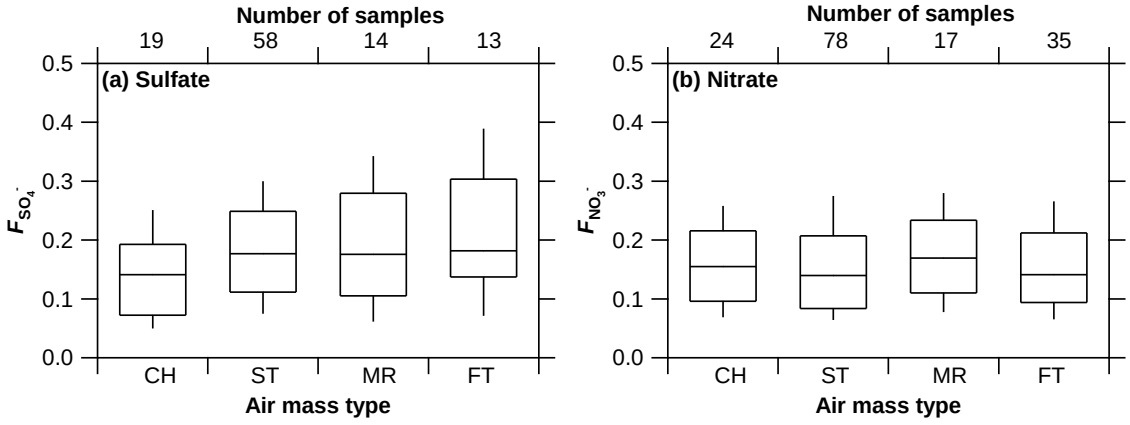

Figure 5.14. Average (a) F_{SO4} and (b) F_{NO3} for each air mass category. The numbers above the plots depict the number of samples. The box plots show the median and 25 – 75% of data. The bars depict the 10 – 90% range.

Figure 5.15a shows a scatter plot of the relation between F_{SO4} and M_{SO4}. Different symbol colors are used for different air mass categories. The F_{SO4} and M_{SO4} related to the specific air mass type. M_{SO4} and F_{SO4} values were higher and lower, respectively, in CH-type air, while the opposite tendency was observed in FT-type air. These results are consistent with the averaged values of M_{SO4} and F_{SO4} as described above (see Figures 5.8 and 5.14). On the other hand, F_{NO3} values did not show clear variability related to the air mass type as shown in Figure 5.15b. In the following sections, the sulfate particles with characteristic variations are discussed.

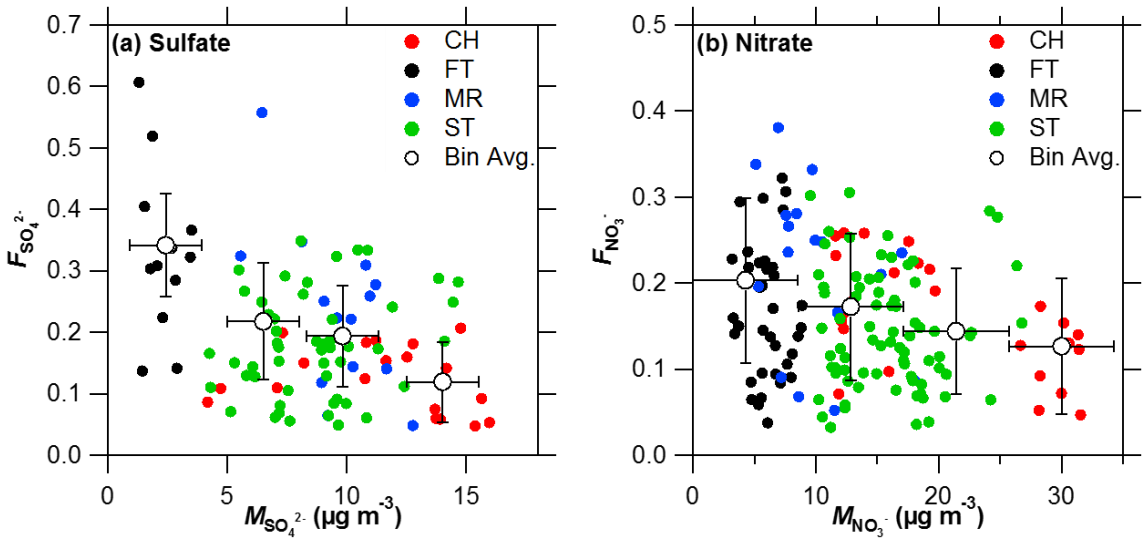

Figure 5.15. Scatter plot of (a) F_{SO4} and the mass concentration of SO_4^{2-} and (b) F_{NO3} and the mass concentration of NO_3^- from different air mass origins. Colors of markers depict the air mass origins; red is CH, black is FT, blue is MR, and green is ST. White circles represent the bin average for 4 μg m^{-3} of the mass concentration. Error bars depict the 2σ of each average value.

5.5. Discussion

5.5.1. Process controlling averaged BC mixing state

As described in the previous sections, by separately measuring aerosol amounts, which internally and externally mixed with BC, following new findings were obtained.

1) G_x^y values, which denote the mass fractions of particular compounds to the total aerosol mass, are generally similar between to the BC-containing and BC-free particles on average. However, one-hour values of G_x^{int} and G_x^{ext} do not show clear correlations.

2) F_x values, which denote the mass fractions of particular compounds internally mixed with BC within a total mass concentration of this species (sum of internally and externally mixed amounts) are similar among SO_4^{2-}, NO_3^-, and OM (m/z 44) on average. Furthermore, one-hour values of F_{SO4}, F_{NO3}, and F_{OM} were weakly correlated.

3) F_{SO4} tends to be inversely correlated with M_{SO4}. M_{SO4} and F_{SO4} values are higher and lower, respectively, in CH-type air, while the opposite tendency is recognized in FT-type air.

Aerosol particles grow by various physicochemical processes, such as a coagulation and condensation in the atmosphere during transport from their source regions. Coagulation and condensation processes depend on particle diameters, number concentrations, and the partial pressure of condensed gases, as described in Section 2. When coating thickness of BC particles is thick enough, condensation and coagulation processes are considered to work in similarly to BC-free particles (externally mixed aerosols). This is because vapor pressures at the particle surface, accommodation coefficients, and coagulation kernels are expected to be similar between BC-containing and BC-free particles in cases when BC particles are fully coated by inorganic and/or organic compounds. Resultantly, mass concentrations of BC-containing and BC-free particles are expected to increase concurrently. Therefore, averaged G_x^y values of internally and externally

mixed amounts become similar. Furthermore, regarding F_x values, the similarities in averaged values and correlations can also be explained by simple condensation and coagulation processes as described below.

For simplicity, ideal cases are considered in which the number concentration ratios of BC to all aerosols (N_{BC}/N_{all}) are same among samples examined here. Even when the absolute number concentrations of BC and aerosols (N_{BC} and N_{all}) are different, F values do not change through the condensation processes if initial N_{BC}/N_{all} values are same. One can easily expect that F values also do not change through the coagulation processes when the shape of initial aerosol size distributions are same. On the other hand, when the initial N_{BC}/N_{all} values are different, the resulting F values become different.

In order to quantitatively examine how condensation process affects BC mixing state, a box model that calculates the condensational growth of aerosol particles and associated changes in the BC mixing state was developed. The details of the box model are described in Appendix 5.4, and a brief summary is given here. In this box model, a size-dependent BC mixing state is represented by a two-dimensional representation of aerosols; the first axis represents dry aerosol diameters and the other axis represents BC mass fraction within all dry aerosol mass. The growth of aerosol is calculated assuming only condensational growth using the mass transfer equation. Consequently, a particle number concentration does not change in this calculation. For initial aerosol size distributions, one size distribution was prepared for pure BC particles and the other one for pure $(NH_4)_2SO_4$ particles, using observations obtained in this study as well as those obtained in source regions in China, namely in conditions immediately after emissions of aerosols and gases [*Cheng et al.* 2017; *Batmunkh et al.* 2016].

The calculation result by the box model is shown in Figure 5.16. Aerosols with large (small)

N_{BC}/N_{all} ratios will result in large (small) F values, as shown in Figure 5.16. This result is reasonable, because when relative the number fraction of BC-containing particles is higher, then the total amount of aerosols that condense on the BC-containing particles is higher, and thus, F values become higher. Because the condensation processes work in the same way for SO_4^{2-} and NO_3^-, one can expect that F_x values become similar for these two compounds and that F_{SO4} and F_{NO3} values correlate with each other.

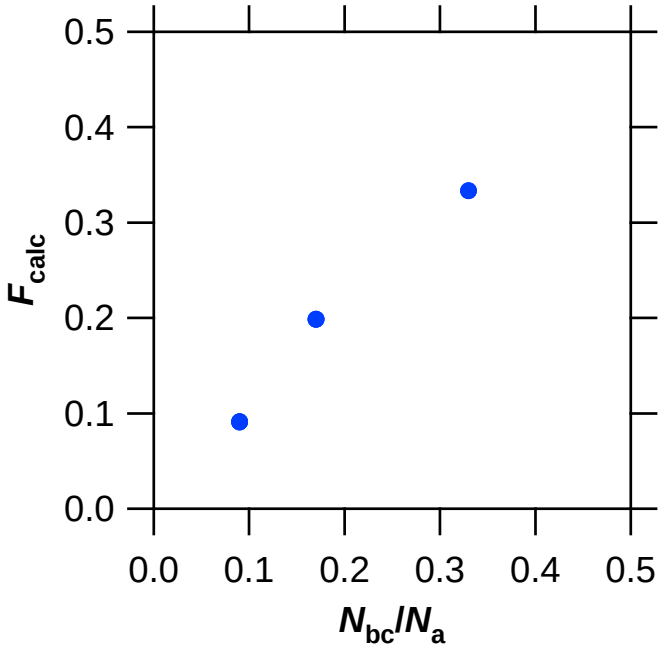

Figure 5.16. Box model calculation result.

However, simple condensation and coagulation processes cannot explain some of the observed features. Figure 5.17 portrays the same data as Figure 5.16, but observed values are presented instead of model calculations, namely, a scatter plot between assumed N_{BC}/N_{all} values and resulting F values. Although a positive correlation is seen for the model calculations, there was no correlation between observed N_{BC}/N_{all} and F values. This result indicates that changes in the N_{BC}/N_{all} values may not be the primary factor causing changes in F values. Furthermore, the condensation/coagulation processes cannot explain the fact that one-hour values of G_x^{int} and G_x^{ext} do not show clear correlations. In addition, the observed inverse correlation between F_{SO4} and M_{SO4} likewise cannot be also explained. These results suggest that the condensation/coagulation processes likely play important roles in controlling the averaged BC mixing states, while other processes also affect temporal variations of BC mixing states that could have worked in different ways between the CH-type and FT-type air.

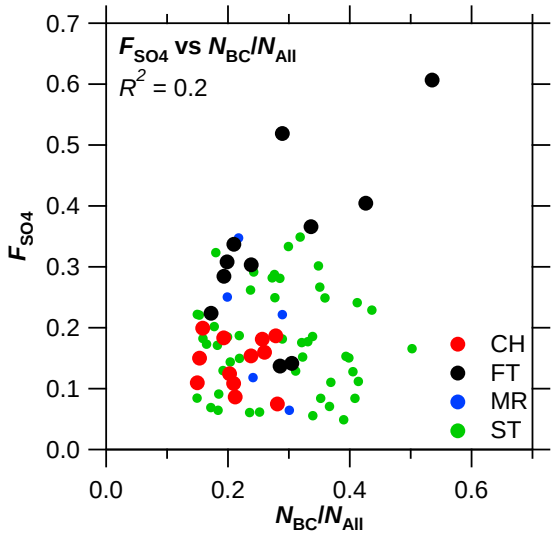

Figure 5.17. Ambient measurements results. Marker colors depict different air mass origins; red is CH, black is FT, blue is MR, green is ST.

5.5.2. BC mixing state in CH-type air

The inverse relationship between F_{SO4} and M_{SO4} values is examined from the viewpoint of differences in atmospheric processes for CH-type and FT-type air masses. For this purpose, chemical signatures of air (aerosol concentrations and size distributions) and properties of air trajectories are examined together. CH-type air is examined in this section, and FT-type air is examined in the next section.

Figure 5.18 shows average aerosol size distributions observed in CH-type air (March 29 and 30 AM). The pronounced feature of these size distributions is that the number concentrations for aerosols with diameters (D) larger than 100 nm were high. In comparison, the average size distribution for FT-type air (April 5 AM) is also shown. This distribution is more like the typical one observed in the atmosphere. The enhancement of aerosols with D = 100 – 500 nm were previously reported [e.g., *Hering and Friedlander*, 1982], and they were attributed to the aqueous-phase sulfate production in the cloud or fog water [*Meng and Seinfeld*, 1994]. These are referred to as the droplet mode aerosols. In general, particles in droplet mode cannot be explained by condensational growth because the gas phase reaction to produce SO_4^{2-} from SO_2 is rather slow. Aqueous phase reactions efficiently supply SO_4^{2-} to the atmosphere [*Kerminen and Wexler*, 1995].

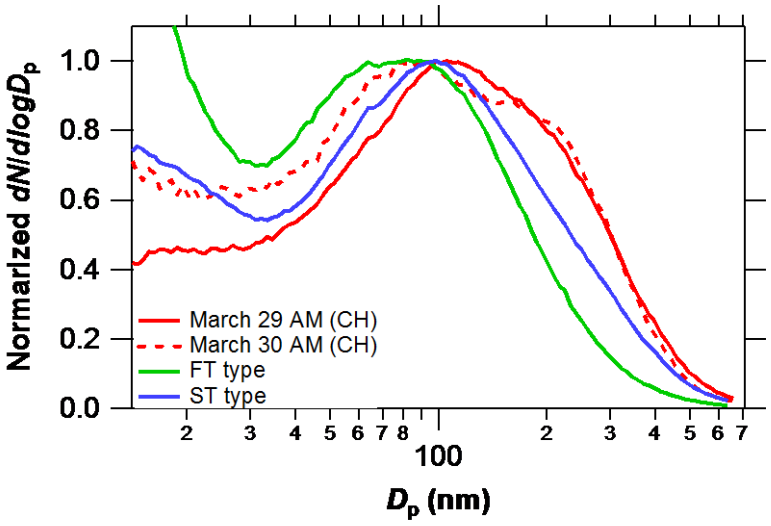

Figure 5.18. Average normalized size distributions measured by SMPS. The size distribution was normalized using the peak value of each size distribution, which was the CH air masses on 29 AM and 30 AM of March, and average of all FT and ST air masses.

Visible and infrared images of clouds over East China and Yellow Seas obtained by Multi-functional transport satellite (MTSAT) from the Japanese Aerospace Exploration Agency (JAXA, http://www.eorc.jaxa.jp) were examined to evaluate possible influences of cloud/fog water to explain observed chemical features of sampled air. Resultantly, when CH-type air had passed over East China and Yellow Seas, clouds were found to be extensively present above these regions (Figure 5.19, Appendix 5.5). Furthermore, as described in Section 5.3.1., backward trajectory analyses show that CH-type air masses had likely been influenced by anthropogenic emissions over China and been transported within the PBL for a few days prior to the measurements (Figure 5.4). The analyses of meteorological parameters along the trajectories show that the CH-type air occasionally experienced high relative humidity values up to ~85% (Appendix 5.3). Although these results do not present direct evidence, one could speculate that CH-type air is affected by aqueous-phase SO_4^{2-} production. If BC-free particles, whose mass concentrations were increased

by the aqueous-phase SO_4^{2-} productions, were mixed into CH-type air, then M_{SO4} would increase with a concurrent decrease of F_{SO4}. Consequently, chemical features that are not consistent with the observations are obtained. However, it is nevertheless highly uncertain when and where the sampled air masses encountered fog or clouds. In this study, one of the possible mechanisms is proposed. In order to quantitatively evaluate the influence of this mechanism on the variability of the BC mixing states, further observations including fog/cloud and precursor gases, as well as detailed numerical modeling are necessary.

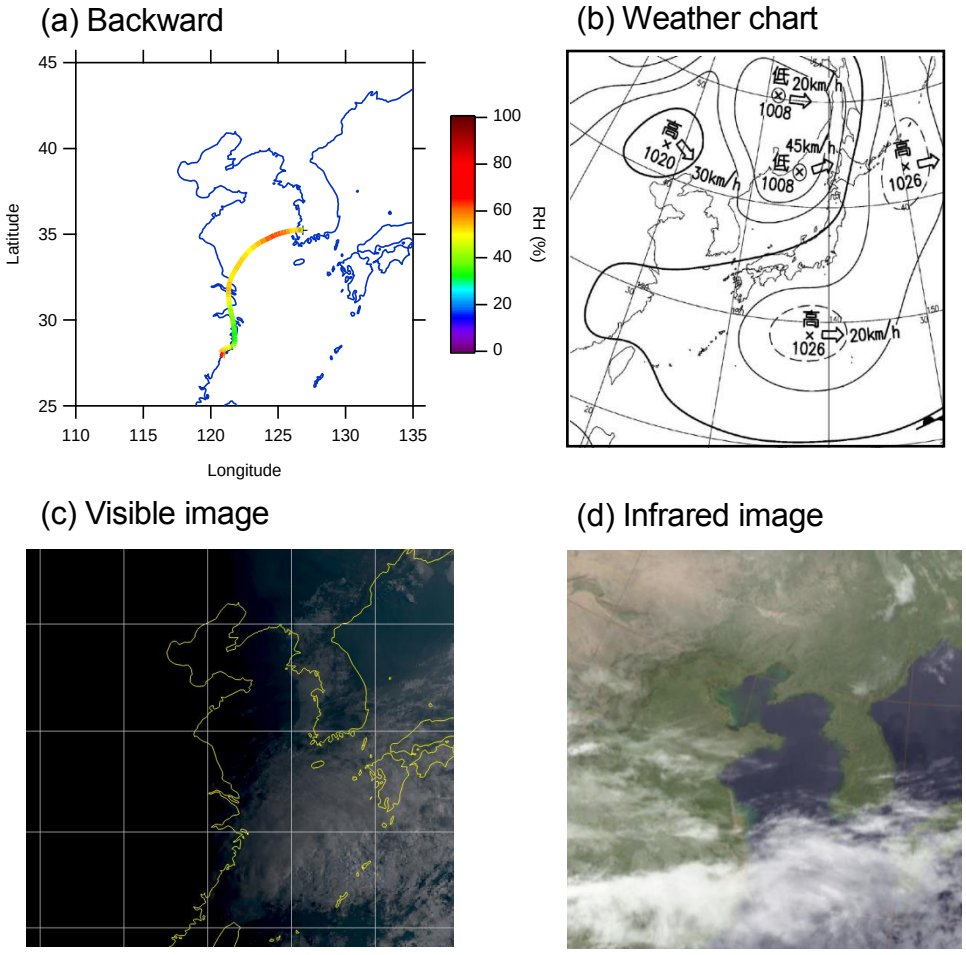

Figure 5.19. (a) Backward trajectory at 6:00 AM on March 30; (b) weather chart at 6:00 AM on March 30; (c) visible image 7:00 AM on March 30 and (d) infrared image 6:00 AM on March 30 observed by MTSAT. Color plots in Figure 5.19c depict the RH value. The visible image at 7:00 AM was used because that at 6:00 AM was not available.

5.5.3. BC mixing state in FT-type air

The chemical signatures of the FT-type air are characterized by low M_{SO4} and high F_{SO4} values. Aerosol concentrations in FT are lower than those in the PBL because of the lack of recent influences from anthropogenic and natural emissions at the planetary surface, and of wet removal processes of aerosols and precursor gasses by precipitation during the vertical transport of air. The wet removal processes of aerosols could explain the observed high F_{SO4} values because the removal rates can be different between BC-containing and BC-free particles during cloud processes, as described below.

Aerosol particles, which can serve as cloud condensation nuclei (CCN), are activated to cloud droplets near the cloud base. One part of these activated aerosols is removed by precipitation through collision- coalescence processes of cloud droplets and drops [*Ohata et al.,* 2016]. Some BC-containing particles are removed from the atmosphere by precipitation, but other BC particles, which are not activated to cloud droplets, tend to be carried to higher altitudes and detained in FT-type air. According to the κ-Köhler theory [*Köhler*, 1936; *Petters and Kreidenweis*, 2007], the critical diameter of aerosol particles activated to cloud droplets can be controlled via the hygroscopic property, κ, determined by the chemical composition of each particle. The κ-value of particles consisting of multiple chemical components is determined by the volume ratio of the components constituting the particle. The κ of BC is significantly lower than that of other aerosol components. Consequently, when the coating thicknesses of BC-containing particles are thin, such as that of freshly emitted BC particles, these particles are generally not easily activated to cloud droplets and are not easily removed. In other words, the critical diameters of BC-containing particles are generally higher than that of BC-free particles, and only relatively large size aerosols are removed by precipitation. For example, assuming a supersaturation of 0.5%, the critical

diameter is calculated to be approximately 190 nm and 40 nm for bare BC particles and ammonium sulfate particles, respectively, as shown in Figure 5.20. Thus, freshly emitted BC particles with thin coatings are more likely to be carried into the free troposphere by cloud processes, while BC-free particles are more efficiently removed. Consequently, internally mixed amounts of SO_4^{2-} become higher, leading to high F_{SO4} values. Figure 5.21 shows data calculated assuming wet removal was performed in 3 hours after the start of calculation using the box model described in Section 5.5.1. The critical diameters calculated using the super saturation ratio of 0.01, 0.2, 0.4, 0.5, and 0.6%. This result can explain the observation result of the FT type air mass as shown in Fig. 5.17, and is qualitatively consistent with the above hypothesis. Nevertheless, there is no evidence to support this hypothesis. To this end, further observation of the mixing states with BC particles using an aircraft are needed.

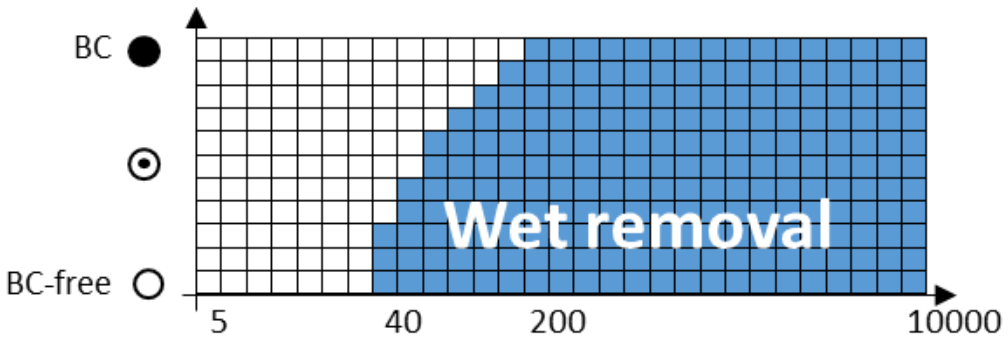

Figure 5.20. Schematic diagram of the dependence of the critical diameter on particle size and mixing state.

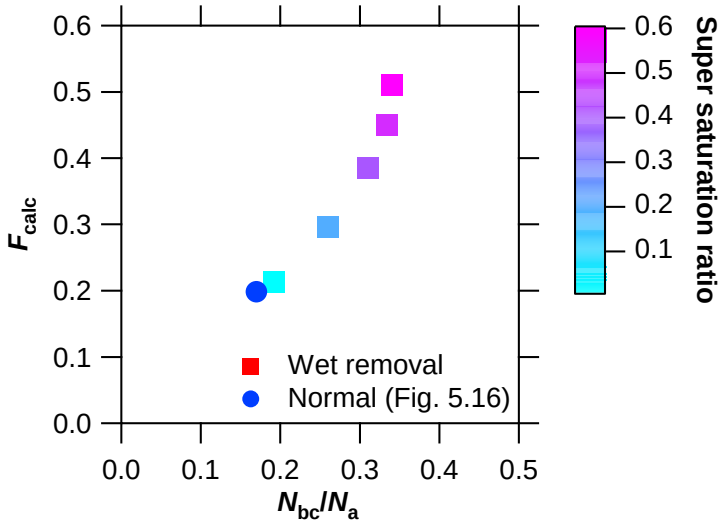

Figure 5.21. Change in *F* value by wet removal using the box model. The blue circle is one of the calculation results shown in Figure 5.16. The square markers are the result of calculation assuming the wet removal as described. After calculating for 3 h from the initial conditions, particles above the critical diameter of wet removal calculated in Figure 5.20 were removed from the calculation. Subsequently, the box model calculation was performed using the particle size distribution of aerosols subjected to wet removal and the gas concentration of 1/100 of the initial value as initial estimates. The color plots depict the super saturation ratio. The super saturation ratios of 0.01, 0.2, 0.4, 0.5, and 0.6% are used.

5.6. Summary

The chemical composition and mixing state with BC in atmospheric aerosols was obtained in Korea during the spring of 2016 using an LII-MS. The observation site is located in the western part of the Korean Peninsula, where the variations at the regional scale occurring in the Yellow Sea can be observed. The air mass origins were classified by backward trajectory analysis.

The mass concentration of the inorganic aerosols measured with LII-MS during the measurement period correlated well with that of BC. No clear diurnal variations were observed in one-hour average values of aerosol mass concentrations. The mass concentrations of SO_4^{2-}, NO_3^-, and BC were higher in air masses originating from the China and extremely low in that from the

free troposphere. The backward trajectory and the temporal variation of mass concentration frequently showed the influence of regional air pollution transported from the Asian continent.

There was no significant difference in the chemical composition between the BC-containing and BC-free particles. The values of the internally mixed fraction for sulfate and nitrate showed a weakly positive correlation. Although measurements were conducted through a limited period, they provide important information for estimating the optical properties and humidity of aerosol particles. These results can be explained by assuming that the coagulation and condensation processes occur without dependence on the chemical compositions or mixing state.

The internally mixed fraction for sulfate tended to be lower in highly polluted air masses originating from China and higher in clean air masses originating from the free troposphere. The inverse correlation between the internally mixed fraction for sulfate and the mass concentration of sulfate cannot be explained by the coagulation and condensation assumption. When observing the air mass originating from China, the characteristic particle size distribution, the droplet mode, was shown, which indicated the influence of the aqueous-phase reaction. On the other hand, the high internally mixed fraction for sulfate in air masses originating from the free troposphere can be explained by the selective removal of BC-containing particles in the cloud process. However, present evidence is inadequate because of the limited data obtained from our measurements. It is necessary to conduct further observations, including the measurement of precursor gas concentrations, and evaluate using 3D models to investigate the processes that determine the variability of mixing states in aerosols.

Appendix 5.

A5.1. Calibration

The data reduction of the LII-MS analyzer was performed as described in the work of *Miyakawa et al.* [2014] and *Ozawa et al.* [2016] (Chapters 3 and 4). Laboratory experiments for determination of the sensitivity used for obtaining the mass concentrations with the LII-MS were conducted using the same setup as that described in Chapter 4. NH_4NO_3 and ammonium sulfate ($(NH_4)_2SO_4$) particles were used for these laboratory experiments to determine the sensitivities for nitrate (NO_3^-) and sulfate (SO_4^{2-}), respectively. These laboratory experiments were conducted on March 28 and April 7 and the average values of the obtained sensitivities were used to calculate ambient mass concentrations.

The inlet flow rate of the PT-LDMS and the LII analyzer was calibrated using a standard flow meter (DryCal DC-Lite Air Flow Calibrator, Brandt Instruments, Inc., USA). Mass concentration is expressed as μg m^{-3} at 25 °C and 1 atm pressure conditions.

A5.2. Measurement setup

As shown in Figure A5.1, the sample air for the LII-MS was aspirated from the rooftop down to the observation room at a height of approximately 10 m above the ground level using a 1-inch stainless steel tube (1-inch tube) with a length of 1.4 m. The 1-inch tube was reduced to a 1/2-inch stainless steel tube and subsequently to a 3/8-inch stainless steel tube. A $PM_{2.5}$-cut cyclone (URG-2000-30EH, URG, Inc., USA) was used to remove coarse particles in the frontal part of the LII-MS analyzer. Because the $PM_{2.5}$ cut cyclone requires a flow rate of 16.7 L min^{-1}, an air flow of ~16 L min^{-1} was drawn by a backup pump added the LII-MS analyzer (which has a flow rate of ~0.1 L min^{-1}).

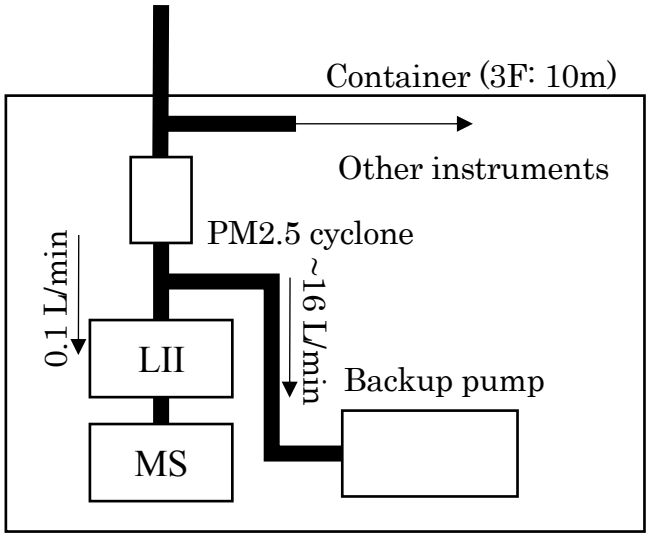

Figure A5.1. Measurement set up.

A5.3. Analysis of RH and the satellite image

A reanalysis of the metrological data set by the Global Data Assimilation System (GDAS) is used in the HYSPLIT model calculation. The spatial and temporal resolutions in GDAS data set are 1°, and 3 h, respectively. Ensemble calculations are started multiple trajectories with each member of the trajectory ensemble calculated by offsetting the meteorological data by a fixed grid factor (0.01 sigma of meteorological grid points). This results in 27 trajectories for all-possible offsets in X, Y, and Z. The meteorological fields followed by individual backward trajectories can diverge significantly.

Figure A5.2 shows the RH trends of the ensemble members. The RH value of CH-type air masses measured on March 30 at 6:00 AM has a large divergence in 20 − 80% within the same period. When the RH was extremely high (80%), the altitude was high (~1.5 km), and the existence of a lower cloud was found in the satellite image. Considering that vertical mixing is abundant in the troposphere, it is considered that the environment in which the aqueous-phase reaction was dominant prevailed. However, the droplet mode and the history of RH are not always consistent. Figures A5.2b and A5.2c show the RH of ensemble members of the backward trajectory at 9 AM

on April 1 and 9 AM on April 2 when observing ST-type air mass. The RH values on April 1 was not high (~ 20%), while there was data that showed high RH (~85%) on April 2. However, in the latter case, data indicating an aqueous-phase reaction could not be obtained. Consequently, it is difficult to estimate the liquid phase reaction from the RH data of the meteorological field.

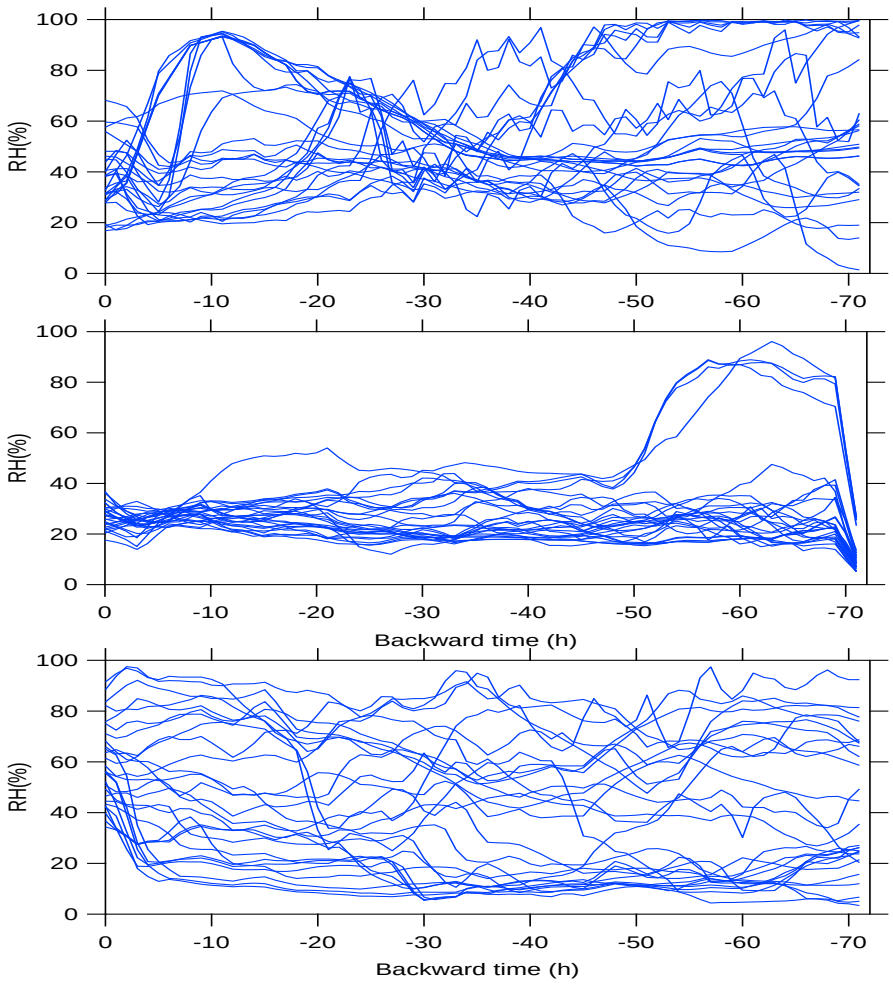

Figure A5.2. Relative humidity trends of ensemble calculations on (a) March 29, (b) April 2, and (c) April 3.

Figure A5.3 shows a typical infrared satellite image in observations of each air mass during the measurement period. A cloud over the Yellow Sea was present when observing CH-type air mass. In the case of ST-type air mass, few clouds were present over the Korean Peninsula; however, there were occasions when a large amount of cloud was present, like on April 2 and April 3.

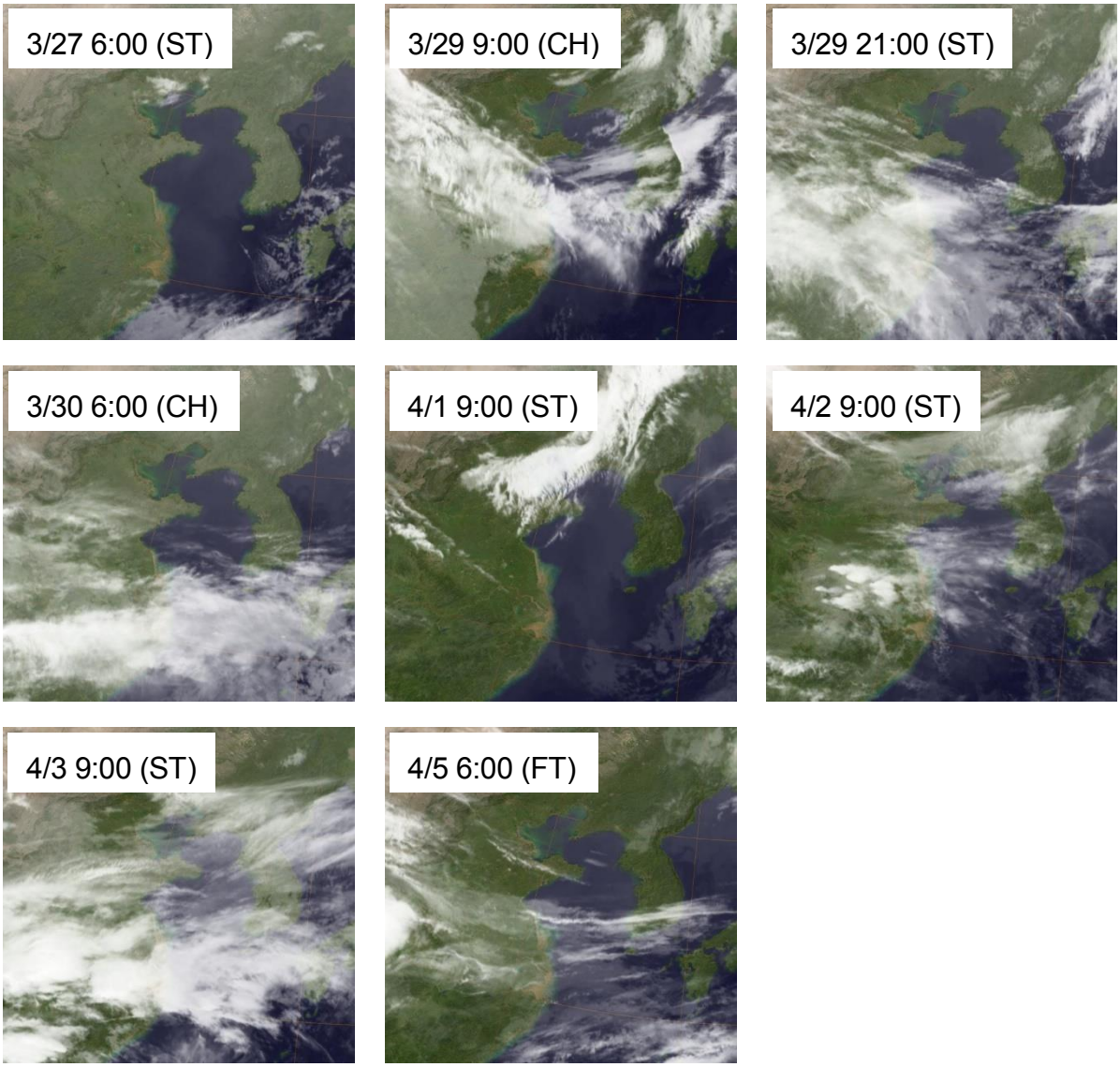

Figure A5.3. Typical satellite images of China and the Yellow Sea obtained from Japan aerospace exploration agency (JAXA).

A5.4. Box model for aerosol growth

Physical and chemical processes that grow aerosol during transportation are mainly condensation and coagulation. Condensation growth is particularly important in regional scale transportation. If the mass transport from the gas phase to the particle phase is considered assuming that particle phase and gas phase are not in equilibrium. By equation 2.3, the change of particle diameter due to the condensation process can be expressed by the following Equation A5.1:

$$\frac{dD_p}{dt} = \frac{4D_i M_i}{RTD_p \rho_p} f(\mathrm{Kn}, \alpha) \left(p_i - p_{eq,i} \right), \qquad \text{(A5.1)}$$

where ρ_p is the density of the particle. Since the change in D_p is inversely proportional to D_p, the change becomes smaller as D_p increases. This calculation was based on the mass transfer equation provided in *Seinfeld and Pandis* [2006]. The calculation result of a simple aerosol bin is likewise reproduced from *Seinfeld and Pandis* [2006].

In the box model, both the particle size distribution and BC mixing state were expressed using a two-dimensional aerosol bin as shown in Figure A5.3. One dimension is the dry particle size of the aerosol and the other dimension is the BC mass fraction of the total aerosol mass concentration in the dry condition. This two-dimensional representation is similar to *Oshima et al.* [2009]. The aerosol size range between 5 nm to 10 μm was divided into 30 bins at equal intervals on the log scale. The BC mass fraction is divided into 10 bins from 0 to 1.0. The initial particle size distribution of the aerosol was assumed to be a lognormal distribution with a mode particle size of 20 nm and $\sigma = 1.5$. The value of N_{BC}/N_{all} (0.1 − 0.4), with the total concentration of the aerosol as 1000 cm^{-3}, was used in the same manner as in the previous studies [*Cheng et al.* 2017; *Batmunkh et al.* 2016]. Other parameters use same in *Seinfeld and Pandis* [2006] ($D_i = 0.1$ cm^2 s^{-1}, $M_i = 100$ g mol^{-1}, $T = 298$ K, and $\rho = 1$ g cm^{-3}).

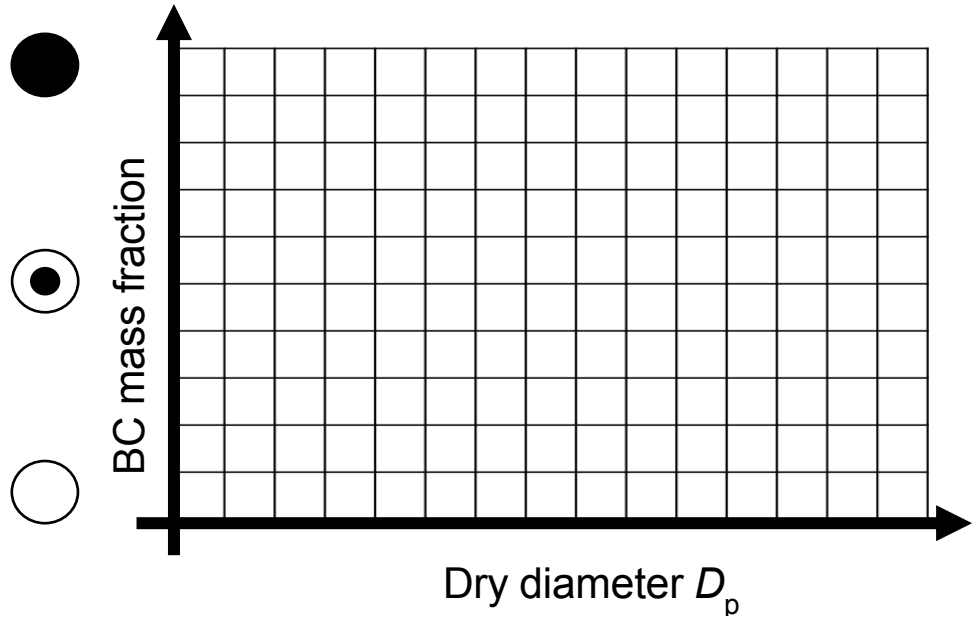

Figure A5.4. 2-D aerosol bin representation

A5.5. Analysis of CH-type air mass

Figure A5.4 shows the backward trajectory line of the CH-type air sample, the satellite infrared image, and the particle size distribution of the aerosol. The twelve samples explain thin clouds above the Yellow Sea. The particle size distributions show the typical droplet mode, although the aqueous-phase reaction may have occurred.

March 29 01:00

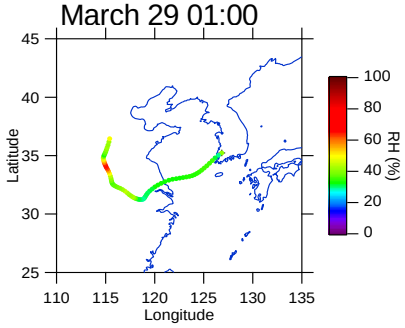

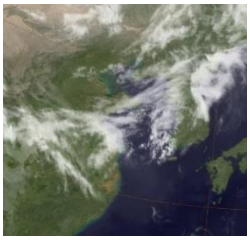

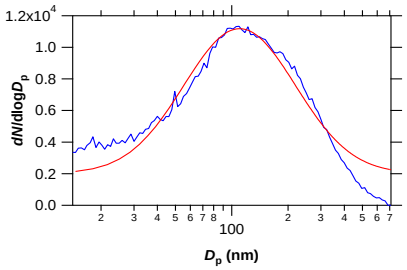

March 29 02:00

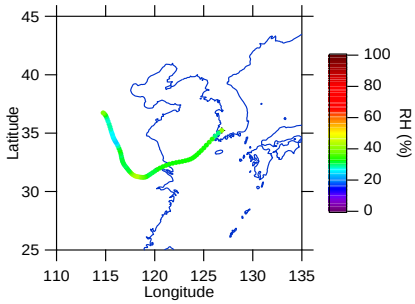

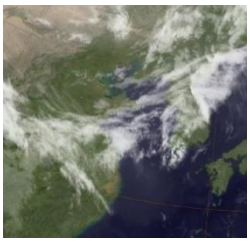

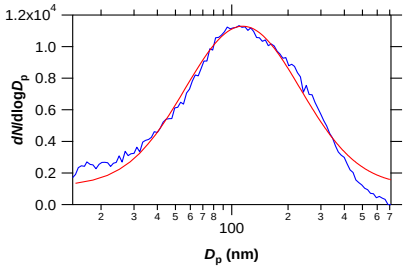

March 29 03:00

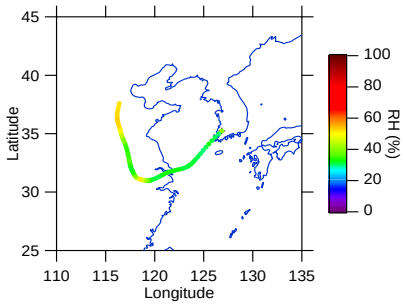

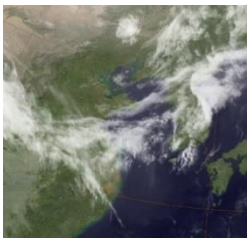

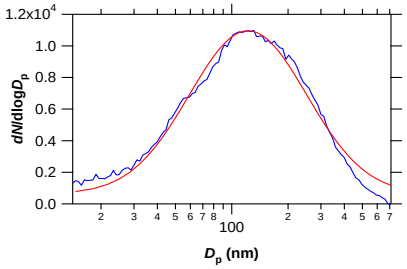

March 29 04:00

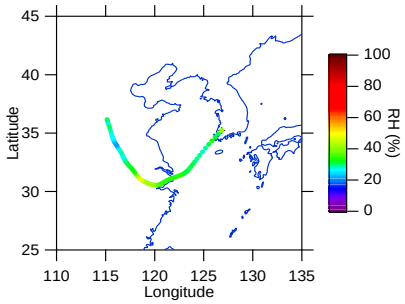

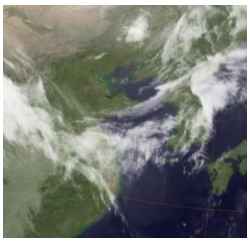

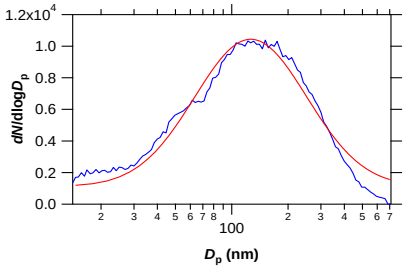

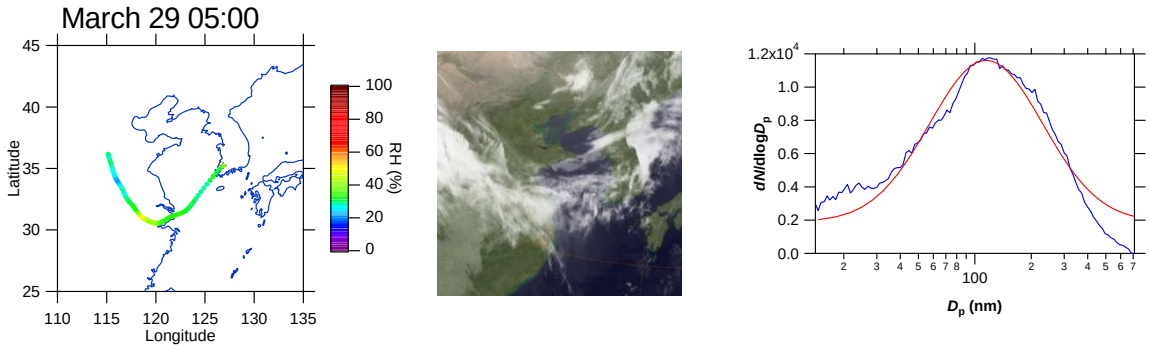
March 29 05:00
Latitude
Longitude
RH (%)
dN/dlogDp
Dp (nm)

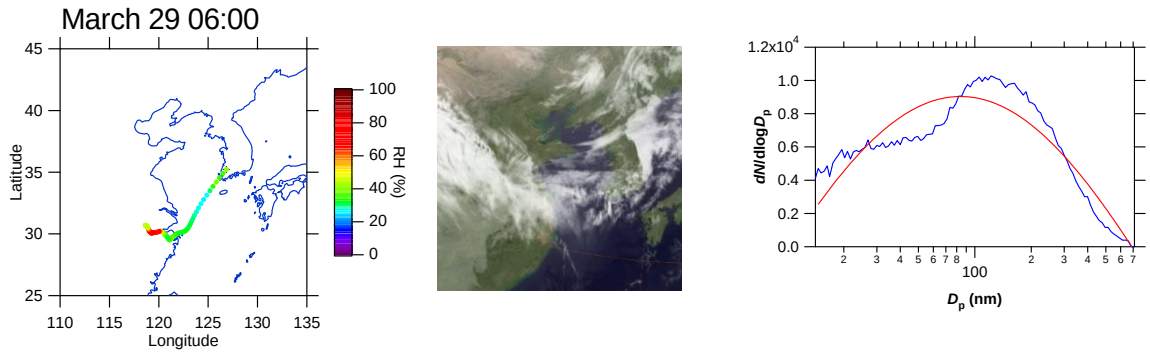
March 29 06:00
Latitude
Longitude
RH (%)
dN/dlogDp
Dp (nm)

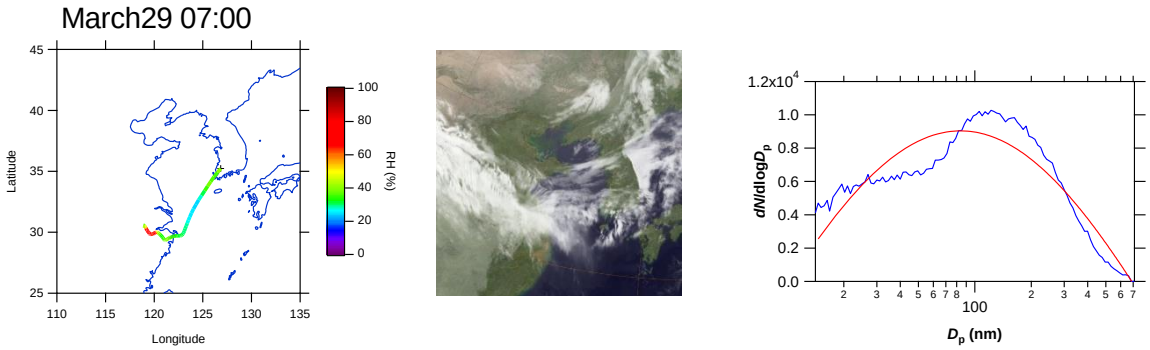
March29 07:00
Latitude
Longitude
RH (%)
dN/dlogDp
Dp (nm)

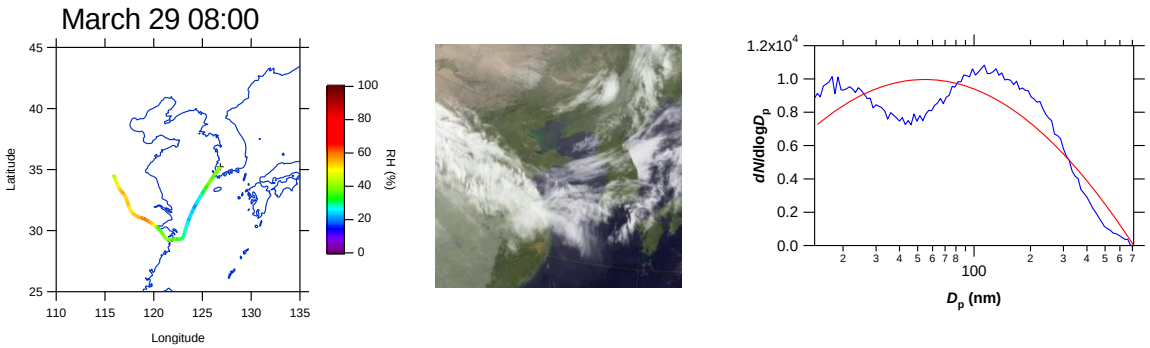
March 29 08:00
Latitude
Longitude
RH (%)
dN/dlogDp
Dp (nm)

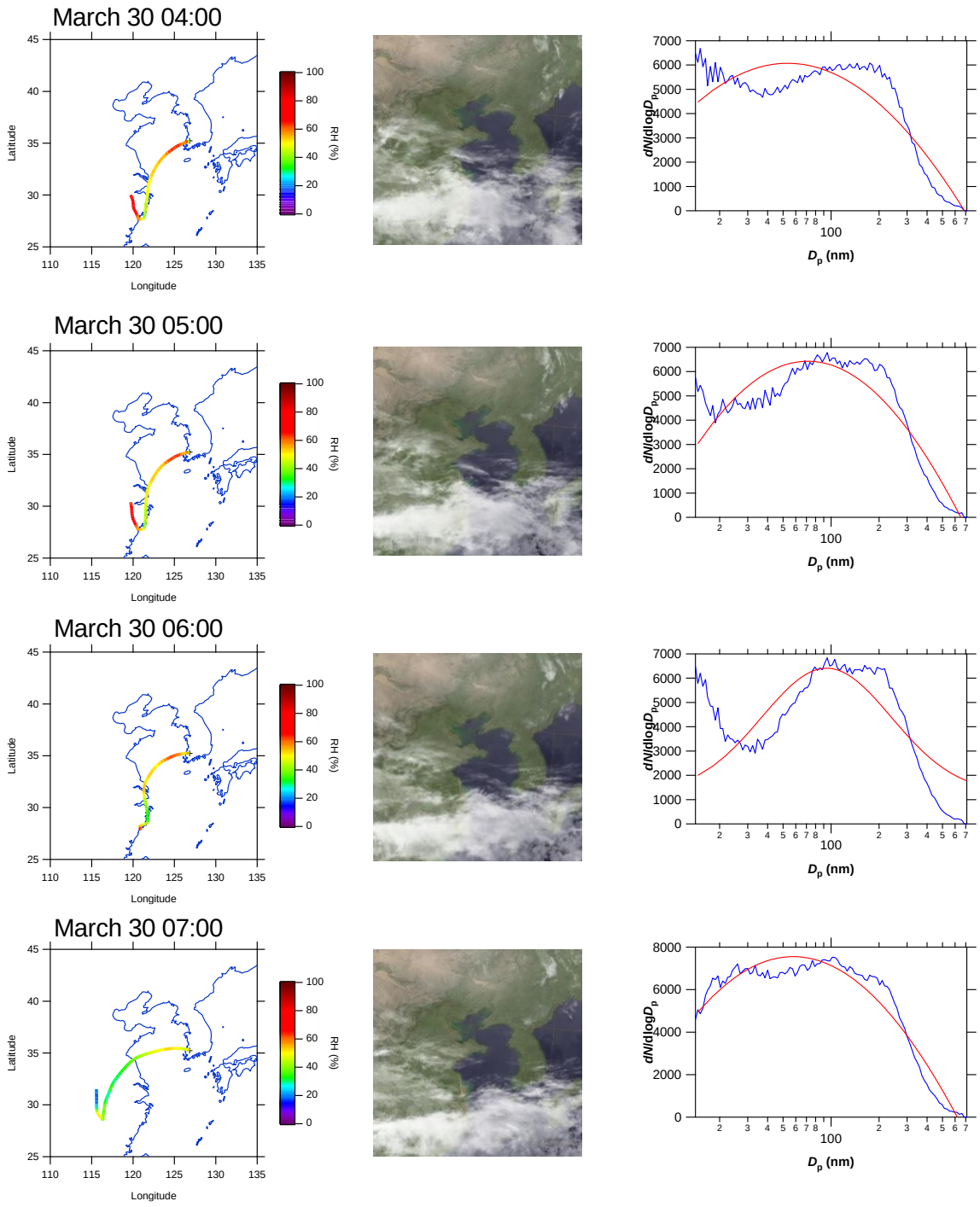

Figure A5.5. The backward trajectories, infrared satellite images, and number size distributions of aerosols in CH-type air samples. The color bars in backward trajectories depict the RH. The red lines in size distributions depict the lognormal fitting lines.

Reference

Batmunkh, T., K. Lee, Y. J. Kim, M. Bae, S. Maskey, and K. Park, (2016), Optical and thermal characteristics of carbonaceous aerosols measured at an urban site in Gwangju, Korea, in the winter of 2011, *J. Air Water Manage. Assoc.*, 66, NO. 2, 151-163.

Chen Y. K., H. Su, D. Rose, S. S. Gunthe, M. Berghof, B.Wehner, P. Achtert, A. Nowak, N. Takegawa, Y. Kondo, M. Shiraiwa, Y. G. Gong, M. Shao, M. Hu, T. Zhu, Y. H. Zhang, G. R. Carmichael, A.Wiedensohler, M. O. Andreae, and U. Pöschl, (2012), size-resolved measurement of the mixing state of soot in the megacity Beijing, China: diurnal cycle, aging, and parameterization, *Atmos. Chem. Phys.*,12, 4477-4491, doi: 10.5194/acp-12-4477-2012.

Cheng, B., Zhe, B., Cui, X., Chen, J., Anderson, A., and Gustafsson, O., (2017), Light absorption enhancement of black carbon from urban haze in Northern China winter, *Environ. Poluut.*, 221, 418-426.

Cui, X., Wang, X., Yang, L., Chen, B., Chen, J., Andersson, A., and Gustafsson, Ö. (2016) Radiative absorption enhancement from coatings on black carbon aerosols. *Sci Total Environ* 551-552:51–56.

Draxler, R. R., and G. D. Hess, (1998), An overview of the HYSPLIT_4 modeling system for trajectories, dispersion and deposition, *Aust. Met. Mag.*, 47, 295-308.

Guo, S., Hu, M., Guo, Q., Zhang, X., Schauer, J. J., and Zhang, R. (2013) Quantitative Evaluation of Emission Controls on Primary and Secondary Organic Aerosol Sources during Beijing 2008 Olympics Atmos. *Chem. Phys.*, 13, 8303-8314.

Guo, S., Hu, M., Zamora, M. L., Peng, J., Shang, D., Zheng, J., Du, Z., Wu, Z., Shao, M., Zeng, L., Molina, M. J., and Zhang, R. (2014). Elucidating Severe Urban Haze Formation in China, *Proc. Natl. Acad. Sci.*, 111, 17373– 17378.

Hansen, A. D. A., H. Rosen, and T. Novakov, (1984), The aethalometer – an instrument for the real-time measurement of optical absorption by aerosol particles, *Sci. Total Environ.*, 36, 191-196.

Hering, S. V., and S. K. Friedlander (1982), Origins of aerosol sulfur size distributions in the Los Angeles Basin, *Atmos. Environ.*, 16, 2647? 2656, doi:10.1016/0004-6981(82)90346-8.

Jiang, H., Liao, H., Pye, H., Wu, S., Mickley, L., Seinfeld, J., and Zhang, X. (2013), Projected effect of 2000–2050 changes in climate and emissions on aerosol levels in China and associated transboundary transport, *Atmos. Chem. Phys.*, 13 (2013), 7937-7960.

Kerminen, V. M., and A. S. Wexler (1995), Growth laws for atmospheric aerosol particles: An examination of the bimodality of the accumulation mode, *Atmos. Environ.*, 29, 3263-3275, doi:10.1016/1352-2310(95)00249-X.

Köhler, H (1936). The nucleus in and the growth of hygroscopic droplets, *Trans. Faraday Soc.* 32:1152-1161.

Manuel, A. L. G., M. C. Araya, A. M. Alvarado, and R. J. Seguel, (2012), Uncertainty estimation of anions and cations measured by ion chromatography in fine urban ambient particles ($PM_{2.5}$), *Accred. Qual. Assur.*, 17:53-63, doi: 10.1007/s00769-011-0844-4.

Meng, Z., and J. H. Seinfeld (1994), On the source of the submicrometer droplet mode of urban and regional aerosols, *Aerosol Sci. Technol.*, 20, 253?265, doi:10.1080/02786829408959681.

Miyakawa, T., N. Takeda, K. Koizumi, M. Tabaru, Y. Ozawa, and N. Takegawa, (2014), A New Laser Incandescence-Mass Spectrometric Analyzer (LII-MS) for Online Measurement of Aerosol Composition Classified by Black Carbon Mixing State. *Aerosol Sci. Technol.* 48:853-863

Moteki, N. and Kondo, Y. (2010). Dependence of Laser-Induced Incandescence on Physical

Properties of Black Carbon Aerosols: Measurements and Theoretical Interpretation. Aerosol Sci. Technol., 44:663-675

Moteki, N., Kondo, Y., and Adachi, K. (2014). Identification by single-particle soot photometer of black carbon particles attached to other particles: Laboratory experiments and ground observations in Tokyo, J. Geophys. Res. 119:1031–1043, doi:10.1002/2013JD020655.

Ohata, S., J. P. Schwarz, N. Moteki, M. Koike, A. Takami, and Y. Kondo, (2016). Hygroscopicity of materials internally mixed with black carbon measured in Tokyo. *J. Geophys. Res.* Doi: 10.1002/2015JD024153

Oshima, N., Koike, M., Zhang, Y., Kondo, Y., Moteki, N., Takegawa, N., and Miyazaki, Y. (2009) Aging of black carbon in outflow from anthropogenic sources using a mixing state resolved model: Model development and evaluation. *J. Geophys. Res.*, 114, D06210, doi: 10.1029/2008JD010680, 2009.

Ozawa, Y., N. Takeda, T. Miyakawa, M. Takei, N. Hirayama, and N. Takegawa, (2016). Evaluation of a particle trap laser desorption mass spectrometer (PT-LDMS) for the quantification of sulfate aerosols. *Aerosol Sci. Technol.* 2: 173-186.

Park, K., J. Park, S. Lee, H. Cho, and M. Kang, (2012). Real-time measurements of the chemical composition of submicrometer aerosol at urban Gwangju in Korea by aerosol mass spectrometer. *Atmos. Environ.* 62:281-290.

Petters, M. D., and Kreidenweis, S. M. (2007). A Single Parameter Representation of Hygroscopic Growth and Cloud Condensation Nucleus Activity, *Atmos. Chem. Phys.* 7:1961-1971.

Seinfeld, J.H., and Pandis, S. N. (2006). Atmospheric Chemistry and Physics. *Jhon Wiley & Sons*, New York.

Shiraiwa, M., Y. Konso, N. Moteki, N. Takegawa, L. K. Sahu, A. Takami, S. Hatakeyama, S.

Yonemura, and D. R. Blake, (2008), Radiative impact of mixing state of black carbon aerosol in Asian outflow, *J. Geophys. Res.*, 113 (D24210), doi: 10.1029/2008JD010546.

Stein, A. F., R. R. Draxler, G. D. Rolph, B. H. B. Stunder, M. D. Cohen, and F. Ngan, (2015), NOAA's HYSPLIT atmospheric transport and dispersion modeling system, *American Met. Soc.*, doi: 10.1175/BAMS-D-14-0010.1.

Streets, D. G., Bond, T. C., Carmichael, G. R., Fernandes, S.D., Fu, Q., He, D., Klimont, Z., Nelson, S. M., Tsai, N. Y., Wang, M., Woo, J. H., and Yarber, K. F., (2003), An inventory of gaseous and primary aerosol emissions in Asia in the year 2000, *J. Geophys. Res.*, 108 (D21), doi: 10.1029/2002JD003093.

Takegawa, N., T. Miyakawa, M. Kuwata, Y. Kondo, Y. Zhao, S. Han, K. Kita, Y. Miyazaki, Z. Deng, R. Xiao, M. Hu, D. van Pinxteren, H. Herrmann, A. Hofzumahaus, F. Holland, A. Wahner, D. R. Blake, N. Sugimoto, and T. Zhu, (2009), Variability of submicron aerosol observed at a rural site in Beijing in the summer of 2006, *J. Geophys. Res.*, 114 (D00G05), dio: 10.1029/2008JD010857.

Wang, G. H., Kawamura, K., Lee, S., Ho, K. F., and Cao, J. J., (2006), Molecular, seasonal, and spatial distributions of organic aerosols from fourteen Chinese cities, *Environ. Sci. Technol.*, 40 (15) 4619-4625.

6. General Conclusion

Laboratory and field studies focusing on the chemical composition of aerosols mixed with BC particles were conducted. This study included the improvement and evaluation of a mass spectrometer, PT-LDMS for practical application of a device LII-MS analyzer capable of quantifying the chemical composition of aerosols classified by the mixing state of BC, and ambient measurements in a downstream area of a large-scale anthropogenic emission source.

Laboratory experiments were performed to investigate the optimal conditions for ambient measurements and the temperature dependence of sulfate sensitivity. The major decomposition product of $(NH_4)_2SO_4$ was similar to that of ambient sulfate in the PT-LDMS. The results also showed that the sensitivity for $(NH_4)_2SO_4$ particles tends to increase with T_{cell}, which may be explained by decreased adsorption of the decomposition product of $(NH_4)_2SO_4$ on the cell surface at high temperatures.

Ambient measurements for the overall testing of the instrument, as well as the intercomparison of PT-LDMS with other measurements methods, were performed in Tokyo. $\Delta Q_{64}^{X}/\Delta Q_{48}^{X}$ for ambient aerosol particles show good agreement with the laboratory data to within 15%, indicating that the thermal desorption products from ambient sulfate aerosol particles are very similar to those from $(NH_4)_2SO_4$ particles generated in the laboratory. The PT-LDMS exhibited tight correlation with the SPA (r^2 = 0.96), but tended to underestimate the mass concentration of sulfate (slope = 0.70).

Major uncertainties in PT-LDMS during the measurement period originated from the size cut of the aerodynamic lens (~12%) and differences in the vaporization efficiency of $(NH_4)_2SO_4$ particles between calibrations and ambient conditions (~10%). In addition, uncertainty in the

contribution of refractory sulfur compounds between the PT-LDMS and SPA was estimated to be ~6% in this case. These uncertainties were estimated by considering numerous sources of systematic error and used for the interpretation of the intercomparison results. The overall uncertainty due to the above factors was estimated to be ~20%, which potentially explains the underestimation of PT-LDMS to a large extent. Further studies using polydisperse aerosol particles and other materials for calibrations are needed in order to improve the accuracy of quantification.

Ground-based measurements of aerosol chemical compositions have been conducted in Asian outflow at an urban site in Gwangju, Korea, from March 26 to April 7, 2016. The air masses measured at GIST were classified as those originating from the continental area, local (urban) area and free troposphere by backward trajectories. There was no significant difference in the chemical composition between the BC-containing and BC-free particles. The values of the internally mixed fraction for sulfate and nitrate showed a weakly positive correlation. Although measurements were conducted through a limited period, they provide important information for estimating the optical properties and humidity of aerosol particles. These results can be explained by assuming that the coagulation and condensation processes occur without dependence on the chemical compositions or mixing state.

The internally mixed fraction for sulfate tended to be lower in highly polluted air masses originating from China and higher in clean air masses originating from the free troposphere. The inverse correlation between the internally mixed fraction for sulfate and the mass concentration of sulfate cannot be explained by the coagulation and condensation assumption. When observing the air mass originating from China, the characteristic particle size distribution, the droplet mode, was shown, which indicated the influence of the aqueous-phase reaction. On the other hand, the high internally mixed fraction for sulfate in air masses originating from the free troposphere can be

explained by the selective removal of BC-containing particles in the cloud process. However, present evidence is inadequate because of the limited data obtained from our measurements. It is necessary to conduct further observations, including the measurement of precursor gas concentrations, and evaluate using 3D models to investigate the processes that determine the variability of mixing states in aerosol particles.

In this study, it was made possible to quantitatively measure inorganic aerosols by thermal decomposition method which had great uncertainty in previous studies. The results obtained in this study are important for considering temperature conditions and uncertain factors in measuring sulfate and nitrate aerosols by the thermal decomposition method. On the other hand, this study enabled highly accurate and stable measurement of inorganic aerosols, it became possible to quantify the chemical compositions related to BC mixing state in the atmospheric conditions. The observation of this study was made near China, which is one of the largest BC emission sources in the world. Air masses from China were transported to the observation site with a time scale of about 24 hours, which is a typical time constant for BC mixing state changes. Consequently, the results presented in this paper were obtained in one of the most important locations of BC studies. The results of this study confirm the importance of understandings of various chemical and physical processes that control the BC mixing state, which is one of the key parameters in evaluating BC radiative forcing through the influences on absorption coefficients and wet removal efficiencies of BC-containing particles. The results of this study also indicate that in order to estimate BC radiative forcing more accurately, numerical model calculations need to more explicitly represent the mixing states of BC (e.g. *Oshima et al.* 2009 and *Matsui et al.* 2013) and more accurately express various aerosol processes, which affect not only BC but also other aerosols, such as the aqueous phase reactions and wet removal. It is generally assumed that

condensation and coagulation take place with same rate coefficients between BC-containing and BC-free particles in current numerical model calculations. The similarity in averaged mass fractions of individual aerosol compounds within all compounds between BC-containing and BC-free particles observed in this study supports the validity of this assumption. However, observations in this study also indicate that even when averaged features (such as mass fractions and internally mixed fractions) are similar between BC-containing and BC-free particles or among aerosol compounds there are considerable variabilities in individual one-hour data. Consequently, in order to evaluate numerical model calculations, it is not enough to only examine averaged quantities but one has to examine variabilities in BC mixing states, which can change averaged quantities. Considering a future pathway for a better understanding of BC radiative forcing and its climate impact, it is important to make more measurements of BC mixing state as well as other aerosol parameters in a various atmospheric environment, such as in China or regions near intense biomass burning. In the near future, a detailed comparison between these new measurements and numerical model calculations must be made.

Reference

Matsui, H., Koike, M., Kondo, Y., Moteki, N., Fast, J. D., and Zaveri, R. A. (2013) Development and validation of a black carbon mixing state resolved three-dimensional model: Aging processes and radiative impact. *J. Geophys. Res.*, 118, 2304-2326, doi:10.1029/2012JD018446.

Oshima, N., Koike, M., Zhang, Y., Kondo, Y., Moteki, N., Takegawa, N., and Miyazaki, Y. (2009) Aging of black carbon in outflow from anthropogenic sources using a mixing state resolved model: Model development and evaluation. *J. Geophys. Res.*, 114, D06210, doi:

10.1029/2008JD010680, 2009.

Acknowledgments

I would like to express my appreciation to the following individuals for their cooperation in this study. I am deeply grateful to Prof. N. Takegawa at the Tokyo Metropolitan University for his continued support and encouragement during the course of my study. I am also grateful to Prof. M. Koike at The University of Tokyo, for his invaluable advice and encouragement throughout my study. I would like to express sincere thanks to Dr. T. Miyakawa at Japan Agency for Marine-Earth Science and Technology for his invaluable comments and suggestions regarding my study. I would like to thank Prof. K. Misawa at Tokyo Metropolitan University, Prof. N. Moteki, and Dr. S. Ohata at The University of Tokyo for their valuable comments and suggestions on this study. I would also like to thank Mr. N. Takeda at Fuji Electric Corporation, Ltd. for his kind support and suggestions regarding my study. I would like to thank Prof. K. Suzuki and Prof. Y. Takahashi at The University of Tokyo, for their valuable comments and suggestions on this study. I wish to acknowledge all of the laboratory members at The University of Tokyo and Tokyo Metropolitan University, and ex-members of the Atmospheric and Oceanic Science Group for their kind support. I would like to thank T. Oizumi and many researchers at the GIST for their cooperation and support. I am thankful to A. Suzuki for her warm encouragement and support during the course of my study. Finally, I would also like to express my gratitude to my family for all the things that they have done for me.

I was supported by the SENTAN program of the Japan Science and Technology Agency (JST) and the Grant-in-Aid for Scientific Research of the Japan Society for the Promotionof Science (25281004).

Publication list

Ozawa, Y., Takeda, N., Miyakawa, T., Takei, M., Hirayama, N., and Takegawa, N. (2016), Evaluation of a particle trap laser desorption mass spectrometer (PT-LDMS) for the quantification of sulfate aerosols, *Aerosol Sci. Technol.*, 50(2): 173-186.

Miyakawa, T., Takeda, N., Koizumi, K., Tabaru, M., **Ozawa, Y.**, Hirayama, N., and Takegawa, N. (2014), A New Laser Incandescence-Mass Spectrometric Analyzer (LII-MS) for Online Measurement of Aerosol Composition Classified by Black Carbon Mixing State., *Aerosol Sci. Technol.*, 48(8): 853-863.

Miyakwa, T., Kanaya, Y., Taketani, F., Tabaru, M., Sugimoto, N., **Ozawa, Y.**, and Takegawa, N. (2015), Ground-Based measurements of fluorescenct aerosol particles in Tokyo in the spring of 2013: Potential impacts of non biological materials on autofluorescence measurements of airborne particles., *J. Geophys. Res.*, doi: 10.1002/2014JD022189